TECHNIQUES AND APPLICATIONS FOR PRECLINICAL SPECT

Bryan C. Yoder

A dissertation submitted to the faculty of the University of North Carolina at Chapel Hill in partial fulfillment of the requirements for the degree of Doctor of Philosophy in the Department of Biomedical Engineering.

Chapel Hill
2008

Approved by:

David S. Lalush

Weili Lin

Marija Ivanovic

Robin Gardner

Arif Sheikh

ABSTRACT

Bryan C. Yoder
Techniques and Applications for Preclinical SPECT
(Under the direction of David S. Lalush)

Two developments of the past decade have spurred the development of SPECT as a useful tool for preclinical research. Development of the pinhole collimator, and the growing library of imaging probes for use with SPECT beyond the traditional markers for perfusion or tumor metabolism have both increased the potential uses of SPECT for small animal research.

The oblique geometry of pinhole rays originating toward the edges of the FOV results in incomplete sampling and poor image quality away from the pinhole orbit plane. Correction requires an orbit that includes an axial component of motion. A simple solution was developed by placing circular orbits at multiple axial locations along the length of the object. When reconstructed with an OSEM algorithm, the multiple projection sets improved data completeness and reconstructed image quality for simulated and experimental data.

Pinhole collimators provide the greatest resolution and highest sensitivity when the object distance is minimized. In actuality, objects are placed some distance from the aperture to ensure that the camera field-of-view is large enough to avoid truncation. A method for improvement was tested by decreasing object distance and obtaining multiple

offset projection sets. The two truncated projection sets were then be reconstructed with OSEM to create an image at with improved resolution.

In addition to advancements in acquisition strategies, the work in this dissertation details two preclinical projects using the microSPECT camera. The microSPECT camera was used to examine the biodistribution of labeled monoclonal and polyclonal antibodies against the neutrophil protein myeloperoxidase. Mice injected with Staph-A were imaged at 24hr post infection with increased uptake of the tracer probe witnessed in the infected region.

A second application required the measurement of hematocrit values using SPECT and labeled erythrocytes and plasma with ^{99m}Tc in ischemic rats. SPECT imaging of the labeled plasma and RBCs showed increases in hematocrit values within the ischemic lesion as defined from an HMPAO perfusion image. Moreover, the hematocrit value varied inversely with the perfusion deficit. For regions of poor blood flow, hematocrit was higher. During reperfusion, when flow was restored, or increased above normal levels, hematocrit levels dropped.

CONTENTS

LIST OF TABLES

LIST OF FIGURES

LIST OF ABBREVIATIONS

1D	one dimensional
2D	two dimensional
3D	three dimensional
ANOVA	analysis of variance
AOR	axis of rotation
CBF	cerebral blood flow
CBV	cerebral blood volume
$CMRO_2$	cerebral metabolic rate of oxygen
CPV	cerebral plasma volume
CRCV	cerebral red cell volume
CT	computerized tomography (x-ray)
CTA	computerized tomography angiography
DWI	diffusion weighted imaging
FBP	filtered backprojection
FWHM	full-width-at-half-maximum
Hct	hematocrit
HMPAO	hexamethylpropylene-amineoxime
HSA	human serum albumin
IgG	Immunoglobulin
MDP	methylene diphosphonate
MPO	myeloperoxidase
MRA	magnetic resonance angiography

MR-COMI	magnetic resonance – cerebral oxygen metabolism index
MRI	magnetic resonance imaging
MTT	mean transit time
NCCT	noncontrast computerized tomography
OEF	oxygen extraction fraction
OER	oxygen extraction rate
OSEM	ordered-subset-expectation-maximization
PCT	perfusion computerized tomography
PET	positron emission tomography
PMT	photomultiplier tube
PSPMT	position-sensitive photomultiplier tube
PWI	perfusion weighted imaging
RBC	red blood cell
ROI	region of interest
ROR	radius of rotation
SPECT	single photon emission computed tomography
UCT	unenhanced computerized tomography

LIST OF SYMBOLS

mm	millimeter
mCi	milliCurie
Pc	Plasma image counts
Pw	Plasma well counter counts
Pwl	Decayed plasma well counter counts
Rc	Red blood cell counts
Rw	Red blood cell well counter counts
F	focal length
L	object length
M	Magnification
β^-	beta particle (electron)
β^+	positron
γ	gamma photon
μ	attenuation coefficient
keV	kilo-electron volt
MeV	Mega-electron volt
Z	Atomic Number

Chapter 1

Introduction

1.1 Background

As biomedical research progresses from bench-top *in vitro* studies toward more clinically relevant *in vivo* work, new tools are needed to answer the questions posed by geneticists, biologists, physicians, and physicists. The development of dedicated imaging modalities for animal research allows these scientists to perform more sophisticated studies and study more complex phenomena. Every imaging modality available for human clinical exams is now also available for small animal studies involving mice and rats, along with the associated complexities in instrumentation and procedures (Klaunberg and Lizak 2004).

Single photon emission computed tomography (SPECT) is a functional imaging modality that examines the *in vivo* distribution of a radio-labeled biomarker. What information the images provide depends entirely upon the kinetics of the biomarker and what it is designed to probe. Traditional tracers such as ^{99m}Tc-methylene diphosphonate (^{99m}Tc-MDP), a bone agent, or ^{99m}Tc-tetrofosmin, a cardiac perfusion agent, are used to determine the functionality of organs or tissue in the body and operate on a cellular level. Advances in radio-chemistry have led to the development of far more specific tracers designed to operate on a molecular level (Lyons 2005).

The development of more specific tracers has in turn spurred development into faster, more capable imaging systems to take advantage of the modern biochemistry. As tracers become more specific, detector sensitivity and resolution must improve as well. Small animal SPECT became feasible after development of pinhole SPECT (Jaszczak, Li et al. 1994; Strand, Ivanovic et al. 1994; Weber, Ivanovic et al. 1994; Weber and Ivanovic 1995). Modern, state-of-the art preclinical SPECT systems rely on multiple detectors each with multiple pinhole collimators to boost sensitivity without compromising resolution (Ishizu, Mukai et al. 1995; Metzler, Jaszczak et al. 2005; Forrer, Valkema et al. 2006; Funk, Kirch et al. 2006; Rentmeester, van der Have et al. 2007). Of course, the trade-off comes at price with modern systems costing hundreds of thousands of dollars to over $1M.

The gamma camera used for the work in this dissertation lacks the modern technological tricks of multipinhole collimation and multi-detectors, but the simple design still allows for reconstructed resolution of 1.2mm using a pinhole collimator and OSEM reconstruction, which is sufficient for many small animal applications. The most limiting aspect of this SPECT system is the imaging time. Research demands ever faster machines capable of finer temporal resolution for more dynamic assessments of tracer distribution. Nevertheless, even the most basic imager can help to answer well-posed questions and hypotheses.

A mix of core imaging physics and application-related work will be presented in this dissertation. A portion of the work in this dissertation focused upon ways to maximize the performance of the SPECT system, hereby known as the microSPECT, by taking full advantage of the pinhole geometry and performance of the reconstruction

software. The remaining work will focus upon two widely different small animal applications using the microSPECT.

1.2 Objectives

The work in this dissertation set out to meet four objectives pertaining to both basic imaging research and imaging applications. The first objective was development of an orbit scheme to improve the axial sampling issues inherent to pinhole, and cone-beam tomography. The pinhole collimator only allows direct views of pixels that lie within the orbital plane. We can easily imagine that rays originating in voxels within the orbit plane must travel perpendicular to the axis of rotation to reach the pinhole and be detected. For voxels that lie above or below this plane, rays traveling to the pinhole must point at an angle less than 90^0 with respect to the axis of rotation in order to be detected. The further above or below the orbit plane the pixels lies, the smaller the angle between the ray and the axis of rotation.

The design of the pinhole results in pixels lying outside the orbit plane being detected at an oblique angle. Because of this, the information contained in the rays detected by the camera do not provide the complete data necessary to properly reconstruct the pixels (Tuy 1983). Rays that travel perpendicular to the axis of rotation provide better data than those that travel at an angle to the AOR. The oblique nature of the rays sampling the outer pixels results in image artifact with the reconstructed image quality worsening at increasing axial distance. By positioning the pinhole orbits at various axial locations along the object, the angle between pixel and pinhole can be increased toward normal and reconstruction artifacts improved. Evaluation of the

proposed dual-circular orbit approach is the first objective of this dissertation. Both simulated and experimental data were collected to validate the approach and determine the optimum geometry given a specific object size and camera field of view.

Another disadvantage of pinhole collimation is the inherent tradeoff between resolution and field-of-view. The highest resolutions require the object to be placed as close as possible to the aperture, but because the field-of-view diminishes, only very small objects can be imaged using the maximum performance. Usually the object is placed at a distance from the aperture so that the camera FOV approximately matches the object size and reduced resolution is accepted.

Considering the resolution/FOV tradeoff, acquiring projections without truncation are generally a higher priority than maximizing magnification as truncated data results in severe reconstruction artifacts. Using atypical orbit schemes and iterative reconstruction methods, however, a set of truncated projections may provide enough information or reconstruction so long as the set contains the proper views to satisfy Tuy's criteria. One such projection set uses two circular orbits with offset axes of rotation. Each individual projection set could fail to meet Tuy's criteria due to truncation and missing views for some pixels, but the missing views from one set would be present in the second. Using both projection sets for the projection/backprojection operations in the reconstruction algorithm allows the entire data set to be updated and truncation artifacts to be avoided. The second objective of this dissertation is to evaluate a dual-axis-of-rotation orbit along with iterative reconstruction, both OSEM and MLEM. Both simulated and experimental data will be used to evaluate the validity of the method and the optimum geometry for a given object size.

With the first two objectives focused upon improvements in pinhole methods, the second two objectives will concern small-animal applications. The microSPECT camera system was designed to image small animals from 20g mice to 400g rats. Although the system was designed primarily for qualitative studies of tracer biodistribution, with proper methods, quantitative data can be obtained from the images as well. The two studies detailed in this dissertation will utilize both different animal models and quantitative analyses.

The first objective requires evaluating the specificity and sensitivity of a novel tracer for visualizing sites of neutrophil activation and inflammation. An autoimmune disease in which antineutrophil cytoplasmic antibodies initiate neutrophil response occurs in a significant portion of the population. The complete disease etiology has not been confirmed, but the target for the antibodies is thought to be myeloperoxidase, a neutrophil membrane protein (Jennette and Falk 1998; Xiao, Heeringa et al. 2002; Huugen, Tervaert et al. 2004; Xiao, Heeringa et al. 2005). The binding of the antibody to the myeloperoxidase initiates the activation of the neutrophil and the resultant burst releasing potent superoxides into the endothelium and stimulating inflammatory responses.

By linking an anti-myeloperoxidase antibody to a radioisotope, imaging myeloperoxidase distribution *in vivo* is possible using SPECT or PET (Querol Sans, Chen et al. 2005). The objective of this project was to evaluate a tracer created from linking the anti-myeloperoxidase antibody, Ih4, with a ^{99m}Tc atom for SPECT imaging. A mouse infection model, based upon an intramuscular Staph-A infection was used as the test vehicle for the tracer. Because the Staph-A infection was expected to result in up regulation of neutrophil cells, the tracer was expected to localize within the infected

region. Both parallel-hole and pinhole SPECT scans were used to provide biodistribution patterns both within the entire mouse body and within the inflammation lesion. A series of experiments varying tracer mass and uptake period were designed to provide insight as to the specificity and sensitivity of the tracer and identify areas of tracer affinity. The experiments performed for this dissertation were geared toward validation of the tracer as suitable for further evaluation in more advanced models.

The fourth and final objective required design of an experimental procedure for measuring hematocrit values within the rat cerebral cortex. A literature search of previous hematocrit studies shows inconsistent results for hematocrit values. A study measuring hematocrit in patients with chronic internal carotid artery occlusion showed decreasing hematocrit values (Yamauchi, Fukuyama et al. 1998), while a second study with acute stroke patients showed increases in hematocrit in the affected hemisphere (Loutfi, Frackowiak et al. 1987). The studies have not been repeated within a controlled animal model so variables in ischemic intensity and duration can be controlled.

Using a rat model for cerebral ischemia, changes in hematocrit values within the ischemic lesion and control region were determined using tracers for red blood cells and plasma along with SPECT. Sequential injection of the blood component tracers with SPECT scans for each; provided images of cerebral cortex where image intensity was proportional to the volume of each tracer. Calibration of image intensities required blood sample analysis for an activity/unit volume value. Using the blood sample counts and image intensity values the hematocrit of the cortex was calculated. The SPECT hematocrit procedure was applied in a series of experiments designed to correlate hematocrit values with ischemic durations.

Ultimately, the work detailed in this dissertation was motivated from two central questions. How can we best take advantage of the available technology, and what potential services can we provide to the local scientific community? Using those two questions as the core motivation, the basic ideas evolved and matured into the projects presented in this work.

1.3 Organization

This dissertation is structured into five chapters, with subsections for each of the four projects. Within each chapter, the project order will remain constant: the dual-circular orbit for improved axial sampling will be presented first, followed by the offset-AOR orbit for truncation correction. The inflammation tracer validation study will follow third with the cerebral hematocrit study presented last. Chapter Two provides a discussion of the basics of SPECT imaging as well as a description of issues regarding small animal imaging. Background and motivations for the hematocrit imaging project and the antibody tracer validation project are also presented. Chapter Three will detail the methods and experimental design for each project with the rationale presented for specific design issues. Chapter Four will present the simulation and experimental results, with Chapter Five providing discussion and conclusions.

Chapter 2

Background

2.1 Basic SPECT Theory and Principles

Single Photon Emission Computed Tomography (SPECT) provides 3D images of the distribution of a radioactive tracer within the patient. A gamma camera views the object from multiple angles, to acquire a set of projections. The set of projections provides the information needed to perform a reconstruction and estimate the point of origin for each photon detected. The imaging process conveniently divides into three stages, projection acquisition, reconstruction, and post-processing.

2.1.1 SPECT Physics and Basic Principles

The image acquisition process starts with the radioactive decay of the tracer nucleus. Radioactive decay can occur through several different processes such as β^- (beta) decay, β^+ (positron) decay, α (alpha) decay or γ (gamma) decay. Directly imaging the β^-, β^+, and α particles is impractical because those particles interact readily with matter and are absorbed before they are emitted from the body, thus they cannot be detected. The positron will interact with matter in such a way that it will annihilate itself along with a local electron and create two 511keV γ-rays traveling in opposing directions. That interaction is the basis behind PET. For SPECT, however, only isotopes that decay via γ emission are used. The ideal SPECT tracer possesses a relatively short half-life to

minimize dose to the patient, emits a γ-ray with sufficient energy to penetrate the body without undesirable scatter or attenuation, binds easily to probe molecules, and is nontoxic. No single isotope can perfectly satisfy all the ideal conditions, but the most commonly used, ^{99m}Tc, comes closest. The ^{99m}Tc γ is 140.5 keV which is sufficient to penetrate the body with only minor attenuation losses. The isotope half-life is 6.02 hours so the majority will decay or be filtered from the body within a few days. The chemistry has been well sorted and hundreds of compounds are available for imaging nearly every organ in the body. Because of these attributes, ^{99m}Tc will be exclusively used in this work. Other common tracer isotopes are ^{111}In (171 keV; 2.83 day half-life), ^{123}I (159keV; 13.2hr), ^{201}Tl (167keV; 3.04 day) and ^{67}Ga (184keV; 78.3hr). Each isotope is suited for specific studies based on the desired half-life and the binding chemistry to provide appropriate pharmacokinetics.

2.1.1.1 Interactions of Radiation with Matter

While the ideal photon will pass through the body without attenuation, the reality is that attenuation and scatter will significantly reduce the number of emitted photons. As the photon passes through the tissue of the body, it has the opportunity to collide with the electrons and nuclei that make up that tissue. Photons can interact with matter through the photoelectric effect, Compton scattering, Rayleigh (coherent) scattering or pair production. The energy of the photon, and the atomic mass, Z, and density of the material through which the photon passes determines which interaction takes precedence. For low-energy photons (<200keV) passing through high Z materials, the photoelectric effect dominates as an atom of the material absorbs the entirety of the photon energy. The absorbed energy is then released via emission of an orbital electron. The electron

then can go on to interact with neighboring atoms and inflict ionization damage to molecules. In this manner, the gamma radiation is said to be indirectly ionizing as the energy is first transferred to the atom, and then from the atom to an orbital electron. Alpha and Beta emission are directly ionizing as their energy is directly imparted to the orbital electron which is ejected from the shell. The difference is somewhat unimportant as the final effect is an atom with a missing electron.

For materials with lower Z, Compton scattering dominates the interactions. When an energetic photon collides with an orbital electron, the energy difference forces the electron out of the shell and the photon continues on an altered path. Compton scattering is often described using a pool metaphor, where the photon acts as the cue ball, and the electron as the target ball. The collision sends both balls away from the point of interaction in different directions. The energy of the continuing photon can be calculated based on the conservation of momentum and energy laws using:

$$E_{sc} = E_0/[1+(E_0/0.511)(1-\cos\theta)] \quad (1)$$

The scattered photon energy, E_{sc}, is dependent upon the initial energy, E_0, and the scattering angle, θ. The rest mass of the electron is equivalent to 511keV, which accounts for the constant in equation 1. Lower photon energies tend to result in larger scattering angles with the maximum angle being 180^0. As the photon energy increases, θ tends to decrease and the photon travels on a path more similar to its initial direction. For most medical imaging situations, the photoelectric effect and Compton scattering dominate the interactions of the photons within the body.

Pair production occurs for very high energy photons (>1022keV) where the deposited energy is transferred during interaction with the nucleus into the creation of a

β^+/β^- pair. Because the rest mass of both the β particles is equal to 511keV, only photons with energies larger than 1.022MeV are capable of providing enough energy for the interaction. Photons with such large energies cause problems for efficient detection and are not used for imaging; they are used in therapy protocols, however.

The fourth interaction is Rayleigh, or coherent scattering. This phenomena is only relevant for very low energies (<50keV). The photon interacts with a nucleus in such a way that no energy is transferred to the nucleus. This is equivalent to an inelastic collision in our pool ball example, such as when the pool ball strikes the wall or some other immovable object. Because photons with such low energies are not as useful for emission imaging due to attenuation and scattering, the most important effects are Compton scattering and the photoelectric effect. Rayleigh scattering is important for X-ray transmission tomography where photon energies are lower.

The interactions of radiation and matter result in an attenuation of the initial photon flux. The probability of interaction increases with increasing tissue thickness so sources that are buried deeper within the body are attenuated more than sources that lie closer to the surface. We can characterize a particular tissue via the attenuation coefficient, μ. The attenuation coefficient describes the likelihood of interaction and is dependent upon the atomic number, Z, the density, ρ, and the photon energy. For a uniform material of thickness, t:

$$I_{out} = I_0 e^{-\mu t} \tag{2}$$

Because absorbed photons are not detected, and scattered photons cannot be traced back to the origin of emission, photons that travel through the body unimpeded are preferred for imaging. Because the probability of attenuation depends on the distance the

photon must travel through the material, a disproportionate number of photons are detected that originate at the surface, and fewer are detected from deeper in the tissue. This results in an attenuation artifact where the measured object distribution does not accurately depict the true distribution. This effect can be compensated by including a model of the attenuation within the reconstruction algorithm to restore the proper distribution.

2.1.1.2 SPECT image acquisition

Since the majority of photons emitted from the source are affected from the photoelectric effect and scattering, utilizing the available photons becomes more important. Acquiring quality projections requires a gamma camera designed with sufficient resolution and sensitivity to obtain adequate images quickly enough to be useful. Due to the difficulty of directly imaging the high energy gamma photons from radioisotope, gamma cameras have used a scintillation crystal to absorb the gamma energy and convert it to visible light which can be viewed with photomultiplier tubes. This phenomenon is called scintillation and the energy of the incident gamma is transferred to the crystal to bump orbital electrons into the valence band of the crystalline structure. Impurities in the crystal create 'holes' for the valance electrons to fall into releasing energy in the form of visible light. The photomultiplier tubes use the photoelectric effect to convert these scintillation photons into electrical charge which is then amplified several billion times. Processing electronics then measure that charge and determine the center of mass of that charge on the face of the detector which is assumed to be the same as the location of scintillation in the crystal. The position of each charge

distribution is plotted and from the sum of all photons measured, an image can be created. A schematic of the process of photon detection can be seen in Figure 2.1.

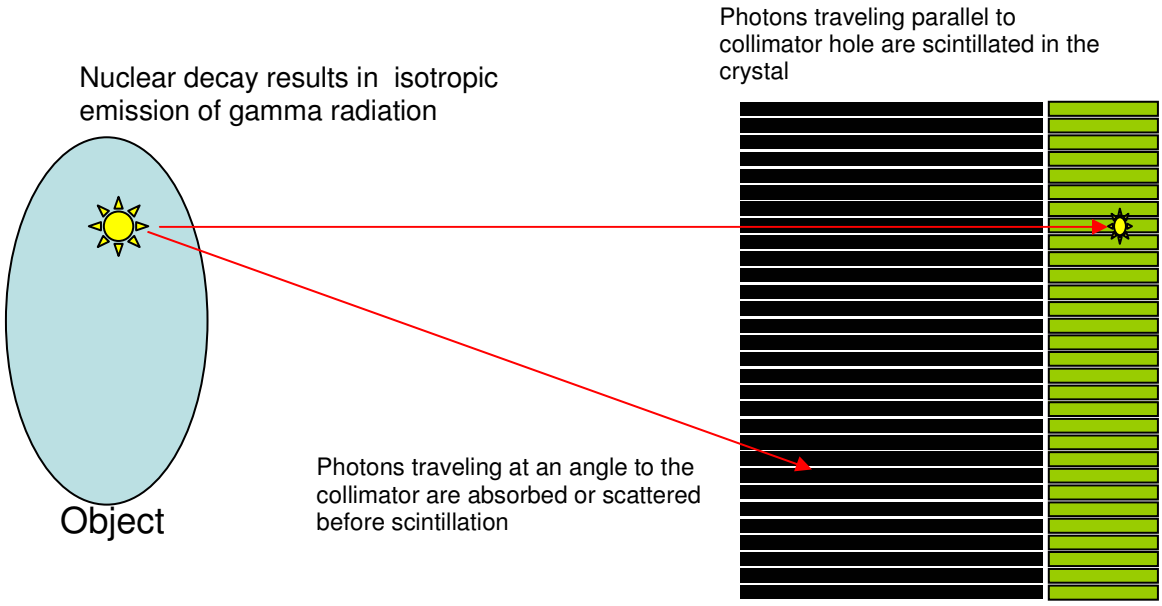

Figure 2.1: Nuclear decay of the radio-tracer results in emission of gamma photons from the object. If the photon is traveling along a path parallel to the collimator it will pass through and be absorbed in the scintillator. As the gamma releases energy to the crystal, the energy is used to create scintillation photons which are detected by the PSPMT.

Measuring the location of scintillation of gammas is only useful if we have some way to know where the gamma was before scintillation. Collimators are used to restrict the flow of gammas to only those that follow a predetermined path to the detector. The most common collimator design uses a honeycomb structure of lead to form parallel columns for the photons to travel to the detector. Any photon traveling at an angle to the direction of the columns is absorbed by the lead septa and not allowed to interact with the detector. This allows each photon that interacts with the detector to be traced back along a direct path toward the object, a critical requirement for reconstruction which will be discussed in section 2.1.3.

Detectors are limited with finite resolution capabilities, so the measured data represents a sample of the true object properties. As such, sampling theory plays an important role in ensuring the accuracy of the representation of the projections and in turn the reconstructed images. An overview of the basic theory behind SPECT sampling principles will be presented in the next section.

2.1.2 Image Sampling Theory

For proper reconstruction and accuracy, the volume of the image space must be sampled properly meeting the Nyquist criteria. The sampling element in the case of volumetric imaging is the voxel – a volumetric pixel. Image sampling can be thought in terms of two independent variables, the path of camera vantage points (orbit), and the number of vantage points along that orbit. It makes sense to start the discussion with analysis of camera orbit as once properly established, it becomes trivial to place the correct number of vantage points along that line. Orlov described the proper orbit for parallel-hole collimation, stating that for parallel-hole collimators the set of vantage points formed a curve on a unit sphere of directions centered on the object "must have points in common with any arc of a great circle" (Orlov 1975).

Consider the image space composed of N voxels with each voxel as the center of a unit sphere. For every voxel to be properly viewed, the set of views of the voxel from the detector must follow a path coincident with any great circle of the unit sphere. For parallel-hole geometry any circular orbit is sufficient to meet this criterion as long as the object is not truncated in any projections. This is due to the fact that every ray from the parallel-hole collimator strikes the voxels at the same angle, if one voxel is properly

viewed, then the symmetry of the collimator means that all the voxels are properly viewed.

The simple circular orbit meets the sufficiency criterion while being the easiest orbit to implement. Clinical systems mount the camera on a slip-ring gantry and rotate the camera about the patient, but the geometrical equivalent of rotating the patient in front of a fixed camera results in identical projections.

For parallel-hole collimation, theoretically, only 180^0 rotation is needed to obtain sufficient data for reconstruction. In the real world attenuation considerations usually require a full 360 orbit. From a reconstruction standpoint, however, each pixel should be viewed from diametrically opposed viewpoints to provide complete data, and a full orbit provides redundant projections. For fan-beam or cone-beam collimation, 180^0 rotation will not provide sufficient viewpoints for every pixel in the image. In these cases, the fan or cone angle must be accounted for due to the fact that all pixels are not viewed from identical viewpoints as in the parallel case. In order to acquire complete data the detector (or patient) must rotate $180^o + 2\ \theta$, where θ is the fan angle. The 180^o +fan angle orbit results in partial redundancy for pixels in the center of the FOV since the fan angle at the center of the collimator is zero. Typically, for in the real world, a full 360^0 rotation is used to provide complete data and reduce truncation effects at a small time penalty.

The other half of the sampling equation involves the proper number of vantage points, or projection angles. Linear sampling theory provides a straightforward guideline for how many samples are required along the projection space with the Nyquist theorem. The Nyquist theorem states that the minimum sampling rate to prevent aliasing is two times the maximum frequency of the signal. Obviously, 2D imaging presents a few

differences from 1D signal sampling, but the principle holds. For an object to be adequately displayed in the image it must be represented by at least 2 pixels in any direction. In order to be resolved, objects must have spatial frequency components smaller than the sampling frequency of the pixel. The angular sampling rate should be chosen so that the sampling interval between angles is approximately the same as the linear sampling interval of the detector. We must remember, however, that the angular sampling interval near the center of the image space is not equal to the angular sampling interval near the edge of the image space. One can think of this by picturing the spokes on a bicycle, the spokes are spaced further apart at the rim than they are at the hub. If each 'spoke' is thought of as a sampling line, we can imagine the sampling density at the center is higher than at the edge. Oversampling the center of the image causes no problems so it is appropriate to focus on the sampling rate near the edge. We can relate the number of views, N, to the linear sampling interval Δr, with

$$N = \pi D/2\ \Delta r$$

where D is the diameter of the image space. Typically, the pixels near the edge of the FOV do not carry as much information as the pixels near the center of the FOV so undersampling the edge does not usually result in major artifacts. A simple rule-of-thumb suggests that the number of projections should be set to 1.5 times the number of pixels across the image for parallel-hole tomography.

2.1.3 Image Reconstruction Techniques

Reconstruction is the process of using the information from the projections to create a 3D representation of the object. Algorithms used for this process can be divided

into two categories, analytical and statistical. The simplest algorithm for reconstruction is simple backprojection. For this method the value in the projection pixels are simply projected back across a line normal to the pixel. The counts in the projection pixel are divided evenly amongst the image pixels along the normal path. The final image results from the summed result of projecting all the pixels in all of the projections. Befitting such a simple method; the results using simple backprojection are usually poor for all but the simplest objects.

The deficiencies from simple reconstruction led to the development of filtered backprojection (FBP). FBP is still the most commonly used reconstruction technique in SPECT and CT clinics because of its ease of implementation and fast speed. We will consider a 1D detector and a 2D reconstruction for simplicity. The 1D projection data must be converted to frequency space (k space) via the Fourier transform. The k space projection data is then filtered by multiplying the data with a ramp filter $|k|$. The ramp filter is arbitrarily cutoff at some frequency, k_{max}, so that noise in the reconstructed image is not amplified, and the filtered k space data are converted back into filtered projections. These filtered projections are then projected just as in the simple backprojection case and a 2D image is formed. For 3D data, this procedure is simply repeated for a stack of 1D projections (S. Cherry 2003).

Analytical algorithms must assume that each pixel in a projection represents the line integral from that pixel back across the object. The validity of this assumption depends a great deal upon the actual physical properties of the object. In the real world the projection process is affected by scatter, attenuation, and detector response.

Compensating for these practical issues has led to the development of more accurate methods based upon statistical models.

Statistical algorithms also assume that each pixel in the projections represents the weighted line integral through the object to be imaged. Where they differ is in the manner they use that information. These methods get their name from the use of statistical measures to determine the final result of the reconstruction. They also use statistical models to more accurately describe the physical process of photon transport (Tsui, Frey et al. 1994). Statistical reconstruction algorithms are most easily implemented as iterative algorithms where an estimate of the object distribution is updated and refined as the algorithm progresses through a series of iterations.

Iterative algorithms have the major advantage of being able to model the physical processes more accurately than analytical methods. For instance, the line integral along the path to the projection bin may not be ideal due to attenuation or scatter, or even the detector response. Those three properties can cause deviation from the ideal line integral and result in an incorrect measured photon position. Iterative algorithms can incorporate these factors into the projector or back projector operations to come up with better estimates of the actual image space. There are many varieties of iterative algorithms, but among the most common are maximum likelihood expectation maximization (MLEM), (Shepp 1982) and ordered-subset expectation maximization (OSEM) (Hudson 1994). They both use a similar update function, but the OSEM algorithm groups the projections into subsets and then updates the subsets. Performing the backprojection and projection operations upon all of the subsets equals a single iteration. Arranging the workload in this manner leads to dramatic efficiency gains and far quicker reconstructions compared

to MLEM (Hudson 1994). The level of acceleration depends upon the number of subsets, and for a single subset containing all of the projections, the algorithm simplifies into the standard MLEM form (Hudson 1994). The work in this dissertation primarily uses the OSEM algorithm due to its relatively fast speed for an iterative algorithm.

2.2 Small Animal SPECT Techniques

The size of the subjects in small animal imaging requires higher spatial resolution than most clinical systems can provide. This has led to the development of compact gamma cameras for what is termed microSPECT. The basic physics behind these cameras is similar to their larger clinical counterparts, but there are a few differences designed to enhance resolution and sensitivity.

2.2.1 Small Animal SPECT Detector Design

Instead of an array of photomultipliers (PMTs), most microSPECT cameras are based on position-sensitive PMTs (PSPMT) (Weisenberger, Bradley et al. 1997; Schramm, Wirrwar et al. 2000; MacDonald, Patt et al. 2001). Most models use either a single PSPMT with a 120mm circular FOV, or a small array of square-flat panel PSPMTs to achieve a similar total FOV with better intrinsic resolution. (Weisenberger, Wojcik et al. 2003) The state-of-the-art in detector design is moving toward avalanche photodiode designs due to their improved resolution, and size characteristics. (Funk, Despres et al. 2006) The advantages of using PSPMTs over arrays of PMTs include better spatial resolution of the scintillated light in a smaller package. The resolution of the PSPMT depends on the design of the anode and how many outputs are available for readout. Older models use 28x28 anode readouts over 10cm while newer models use 64x64 or higher over 4cm. This leads to an increase in available resolution so smaller crystal

elements can be used, although the additional readouts require more sophisticated electronics to convert the various output values into a useful position value. The PSPMT anode readouts are combined and reduced into 4 channels (+X, +Y, -X, -Y) that allow for software determination of the position of the incident photon using Anger logic. (Popov, Majewski et al. 2001) This simplifies the electronics and allows a standard desktop PC to control the camera.

A second difference between microSPECT and clinical SPECT cameras lies in the design of their scintillator crystals. Papers have shown that the light spread in a scintillator for clinical cameras can be several cm.(Scrimger, 1967). Obviously, since the entire FOV of a microSPECT is only 10cm, this would result in poor spatial resolution. The solution has been to construct large crystal arrays from smaller elements. In effect this creates a 'pixilated' crystal. Reflective material between the pixel elements prevents scintillated light traveling between the individual elements. This design limits the spread and allows the PSPMT to identify a single element. This arrangement also helps with resolution, as the intrinsic resolution of the detector is approximately the size of the crystal elements used. Smaller elements allow for higher intrinsic resolution, defined as the uncollimated resolution of the detector. The intrinsic resolution for the microSPECT at UNC is ~1.6mm, while newer models can do better than 1mm.

2.2.2 Pinhole Collimator Geometry

The collimator influences image quality far more than the detector or scintillator design. Clinical cameras tend to use parallel-hole collimators primarily, with occasional use of fan-beam or perhaps cone-beam collimators for brain imaging. These collimators allow for a sufficient FOV for scanning broad ranges of human sizes. Small animal

imaging requires only a small FOV so pinhole collimators can be used. A pinhole trades off FOV for increased resolution and sensitivity. Development of the pinhole collimator has been critical to the success of small animal imaging as the resolution can approach 1mm with a simple system, with some of the newer systems citing sub-millimeter resolution.(Funk, 2006) For comparison, a clinical system with low-energy-high-resolution (LEHR) collimators, the reconstructed in plane FWHM is only about 1cm.

The geometry of a pinhole allows the object to be magnified in the projection image. The degree of magnification is related to the focal length of the pinhole, defined as the distance from the detector to the pinhole aperture, and the distance from the aperture to the object. The basic geometry of a pinhole collimator is shown in Figure 1.2.

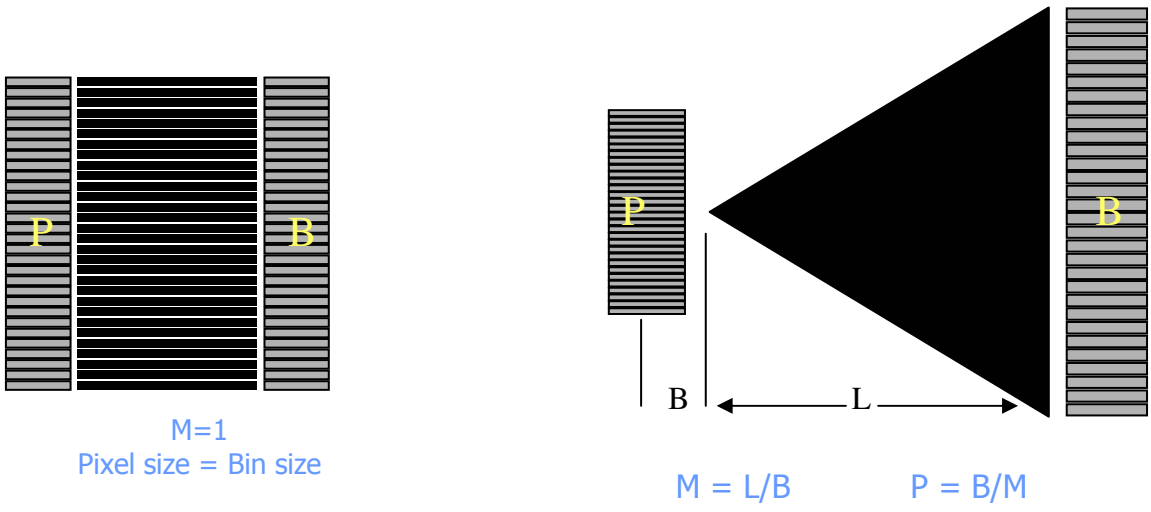

Figure 2.2: Parallel-hole collimation (l) results in a 1:1 relationship between the image space and the detector FOV. Pinhole collimation (r) uses magnification to divide the available detector bins over a smaller image space. With more pixels over a smaller area resolution is increased.

If a clinical system can be fitted with a pinhole collimator, the size of the FOV allows large magnification levels to be used. The increased magnification makes up for the poorer intrinsic resolution of the detector and can make clinical systems appropriate for small animal imaging. In fact, current research is working to exploit the large FOV of clinical systems with multipinhole collimators.(Funk, Despres et al. 2006; Vastenhouw and Beekman 2007) These collimators place an array of pinholes between the object and the detector with each pinhole mapping to a different location on the detector face. This allows for increased axial sampling of the object so entire animals can be imaged instead of small regions. This also increases sensitivity as each pinhole can be treated as a separate entity creating several virtual detectors with a single camera. Care must be taken with the design of the collimator to not allow much overlap between the projections, but if this can be taken care of, the multipinhole collimator is the best way to image animals. Ironically, this approach is less effective on many dedicated microSPECT cameras. The small FOV of these cameras does not allow for the pinhole projections to be spaced appropriately resulting in excessive overlap. This overlap has the effect of decreasing the signal to noise ratio because now more information must be used to determine which aperture a given photon passed through, instead of using that information for reconstruction. This has the effect of reducing image contrast with multipinhole systems. (Yoder, Lalush 2006)

2.3 SPECT Tracers for Inflammation Imaging

Functional imaging methods such as SPECT or PET offer a unique perspective for imaging infection and inflammation. Often the tracers used in these modalities can detect functional changes before obvious anatomical defects present. More mature

tracers for inflammation imaging include ^{67}Ga, and ^{111}In and ^{99}Tc labeled white blood cells (WBC).

Use of ^{67}Ga exploits the fact that the element acts as an iron analog. This allows it to leak through endothelial junctions into infection sites where it can bind to iron-binding proteins in inflammatory cells or bacterial siderophores.(Love and Palestro 2004) Because this method does not directly require labeling of WBCs, it is most often used in cases of low WBC recruitment such as TB infections or in patients with reduced white cell function.

The other two mature methods of infection imaging require labeling of leukocytes and then tracking the accumulation of those cells into areas of infection and inflammation. These methods are more labor intensive as blood must be drawn from the patient and then labeled in vitro otherwise the tracers will nonspecifically bind to other cites in the body. The use of ^{111}In allows for better physiologic specificity, as the ^{111}In-WBC complex does not show gastrointestinal uptake, as does the ^{99}Tc-WBC tracer. Use of ^{99}Tc-WBC can result in better image quality, however, as larger injected activity can be used due to the lower dose administered to the patient. This is primarily due to the shorter half-life compared to ^{111}In.(Love and Palestro 2004)

The ability to label antibody proteins provides a platform for more focused targeting of inflammatory processes. The high specificity of antibodies for target proteins allows differentiation of inflammation pathways depending on what organ is examined.

The lessons learned from previous antibody applications can be applied to the imaging of antineutrophil cytoplasmic antibodies (ANCA) and the vascular inflammation

and kidney glomerulonephritis they cause. The ANCA have been identified in several conditions including inflammatory bowel diseases, autoimmune diseases and infections, but there are two main subgroups of ANCA. The first can be denoted as P-ANCA, so named because of its staining pattern when using fluoroscopic stains. The P-ANCA protein shows staining in the perinuclear/nuclear space, while C-ANCA shows staining in the cytoplasmic space. These two subtypes both result in vasculitis, although the proteins targeted and the details of the disease progression differ.

The C-ANCA subtype primarily reacts with the proteinase 3 (Pr3-ANCA) with one example disease being Wegeners granulomatosis, while the P-ANCA interacts with myeloperoxidase (MPO-ANCA) and causes microscopic polyangiitis and allergic granulomatous angiitis. The prognosis for either of the two types is poor when left untreated, but administration of corticosteroids and cyclophosphmide usually leads to remission within a few months.(Mansi, Opran et al. 2002)

Both clinical investigation and *in vitro* experimentation lead investigators to suspect that the ANCAs played a pathologic role in the vasculitis, but could not prove causation without direct *in vivo* experimentation. The interactions of the ANCA with the target neutrophils were characterized with the help of *in vitro* work. The current theory behind the neutrophil activation suggests that the ANCA bind to targets both on the surface and within the cytoplasm of the neutrophil cells. The two main targets are the MPO and the PR3 antibodies, which are drawn to the surface of the cell in the presence of some 'primer.' (Falk and Jennette 1997; Jennette and Falk 1997) The primer could be a stimulating agent such as lipopolysaccharide or cytokine tissue necrosis factor. Once the neutrophil is primed and the target proteins are directed toward the surface, the

ANCA bind and initiate activation of the neutrophil. This leads to a respiration burst and degranulation, ultimately resulting in superoxide release into the immediate area surrounding the neutrophil. Additionally, the presence of the ANCA has been shown to increase the affinity of neutrophils for endothelial cells.(Heeringa, Huugen et al. 2005) Thus the neutrophils stick to the endothelium and so when activated release their contents directly onto the endothelial layer. The contents released upon neutrophil activation include cytokines, chemokines, proteolytic enzymes and reactive oxygen. The endothelial cells then react with the superoxide and other neutrophil agents resulting in inflammation and necrosis.(Savage, Harper et al. 2002; Jennette, Xiao et al. 2006)

Animal models mimicking the vasculitis effects of the antineutrophil antibody have been developed using both rats and mice. These models allow investigation of the cause-effect relationship between the ANCA and the pathology witnessed in humans. There are now multiple models designed to mimic the effects of the anti-myeloperoxidase ANCA protein. (Yumura, Itabashi et al. 2006)

Mice have been engineered via gene knockout to lack expression of the meyloperoxidase MPO antigen. Subsequently, these mice develop autoantibodies against MPO as it is deemed a foreign substance by their immune systems. Harvesting blood samples containing these autoantibodies and injecting them into healthy, normal mice results in the anti-MPO antibodies reacting against the native MPO in the healthy mice. (Xiao, Heeringa et al. 2002) The result approximates an autoimmune response with similar pathogenesis to ANCA induced vasculitis seen in humans. The glomular epithelial cells suffer the most intense immune response and incur the largest injury. By imaging the distribution of the 99mTc-MPO agent, we expect to see increased uptake in

regions where the immune response is greatest. In vitro studies such as ELISA and in vivo studies on the animal model have shown inflammation in the glomular endothelial cells. We hypothesize that SPECT pinhole imaging will result in increased uptake in the kidneys relative to a control mouse. The resolution of the pinhole is ~1.2mm FWHM, which should allow visualization of the kidney, although it is not sufficient for detailed differentiation of kidney components.

2.4 Imaging Methods for Ischemic Stroke

The first few hours after stroke or incidence of an ischemic event provide the greatest opportunity to intervene and minimize the trauma to brain tissue. Accurate diagnosis at the earliest opportunity since stroke becomes critical as stroke can manifest in several different ways, thrombolic, embolic, or hemodynamic with each variant requiring a different mode of therapy.(Hashimoto, Hirano et al. 2005) Quickly determining the type of stroke and plotting the appropriate course of action are of utmost importance. The vast majorities of strokes are of the thrombolic variety and are treated with thrombolytic drug therapy.(Hashimoto, Hirano et al. 2005) Because the drugs used could cause hemorrhage in patients misdiagnosed for thrombolic stroke, properly evaluating the patient quickly becomes the highest priority. From an imaging standpoint, proper diagnosis requires confirmation of an ischemic core and possibly a penumbra of potentially salvageable tissue. Most stroke imaging techniques are focused on recognizing and identifying the signals from the penumbra.(Bryan, Levy et al. 1991) As this region exhibits reduced cellular function due to insufficient blood supply, several potential suitable imaging markers exist, with each identifiable by a different modality.

A brief history of the modalities used, and what they are sensitive to, will set the stage for current stroke research.

2.4.1 CT Based Approaches for Stroke Diagnosis

Of the several imaging modalities used to look for signs of ischemic attack, each provides differing information and exploits differing physical processes. Often CT is the primary modality to be used in clinical settings, particularly small community hospitals due to its low cost and mature technology. There are three varieties of CT used for stroke diagnosis: unenhanced CT (UCT), perfusion CT (PCT), and CT angiography (CTA). Unenhanced CT can be used to rule out any hemorrhage or to find any massive changes in attenuation due to ischemia. The poor sensitivity of non-contrast UCT lacks the ability to distinguish between healthy and ischemic tissue in the early stages of trauma, which limits the modality's usefulness to acute ischemic stroke.(Tan, Dillon et al. 2007) Because of the high prevalence of CT machines in clinics and cheaper costs involved relative to other modalities, CT is still the primary imaging modality used for diagnosis of stroke.(von Kummer, Allen et al. 1997)

Improved acquisition methods and contrast agents have been examined to improve the information generated from a CT scan. Both PCT and CTA have been used to determine both the ischemic core and the potentially salvageable tissue surrounding it. In one paper, both PCT and CTA were compared with standard non-contrast CT. (Tan 2007) Because each imaging protocol provides differing information and emphasis on differing anatomical or functional features, they found that the best imaging protocol involved using both PCT and CTA scans to identify cerebral blood flow and locate the ischemic core and any potentially salvageable tissue.

A typical CTA scan provides coverage from the aortic arch to the circle of Willis and focuses on the carotids and other arteries in the neck. Contrast agent is administered slowly for 30sec which provides the best contrast to show the blood vessels. Blockages of arteries show as cold spots or unexpected empty areas where the contrast agent does not penetrate the thrombus.(Srinivasan, Goyal et al. 2006)

In addition to the CTA scan, often PCT scans are performed to measure mean transit time (MTT), cerebral blood volume, and cerebral blood flow. The procedure is similar to CTA, but quantitatively more intense due to the analysis of specific regions of interest to be defined by the radiologist. Typically, they look at a set of pixels representing an artery, a set of pixels representing a vein and a set of pixels representing parenchyma. When the contrast bolus is injected, the time/attenuation curves are plotted for both ROIs. Deconvolution analysis can then be used to calculate the mean transit time, defined as the time it takes for the bolus to go from the artery to the vein. Calculation of the integral of the time-attenuation curve for the parenchymal and the arterial ROIs allows the cerebral blood volume to be calculated. Finally, cerebral blood flow can be calculated using the central volume principle where CBF = CBV/MTT.(Srinivasan, Goyal et al. 2006)

From the three CT scans, it is possible to obtain an idea of both the ischemic core and the extent of the penumbra. All evaluations are based on the hypothesis that the ischemic core shows large decreases in both blood flow and blood volume, while the penumbra shows a large decrease in blood flow, but little decrease in blood volume. While the information provided by the CT scans allows for an informed decision about treatment, the basic principles that guide the determination of penumbra are rather crude

and do not directly measure the functionality of the affected cells. For that information, other modalities are needed.

2.4.2 MR Based Stroke Imaging Methods

Although recent advances in CT contrast agents and imaging protocols allow for clinically relevant information to be gained from CT scans, the ability of MR to distinguish ischemic regions has been well proven and is still considered the gold standard for stroke imaging.(Bryan, Levy et al. 1991) MR also can be tailored to emphasize different traits much like CT. Conventional MR, MR angiography (MRA), perfusion-weighted MR (PWI), provide similar information to their respective CT scans, although the design of the scanner allows the entire brain to be imaged with MR instead of only a few axial slices as with CT.

One of the more common MR techniques, diffusion-weighted imaging (DWI), allows emphasis to be placed on the diffusion of protons, which can be treated as markers for water. This particular scan has no analogy with CT and is an advantage for using MR. In areas of ischemia, the breakdown of ion pumps on the cellular membrane results in osmotic pressure driving water into the cells which makes it less mobile.(Li, Chen et al. 1998) In DWI, this results in areas of increased intensity relative to normal tissue. Because proton diffusion results in phase shifts that lead to signal loss, reduced diffusion results in reduced phase shifts and therefore less signal loss.(Davis, Robertson et al. 2006)

The actual DWI sequence differs little from a standard spin-echo sequence, and was first introduced by Stejskal and Tanner.(Stejskal, Tanner et al. 1965) The pulse sequence consists of adding two identical gradient pulses to the spin-echo sequence. The

purpose of the gradients is to give each proton in the imaging space a different spin based on the position of the proton with respect to the magnetic gradient. Now protons have a different phase depending on their physical location. This can be thought of as labeling the proton. A 180^0 pulse is applied inverting the phase of the protons, and the final gradient pulse is applied. The second gradient again induces a phase in the protons dependent upon their physical location. If the proton hasn't moved, then the net result of the two gradient pulses and the inverting pulse is no change in the apparent phase of the proton and no change in signal. If the proton has moved, however, the phase shifts induced by the gradient will not cancel out and will be detected.(Schaefer, Copen et al. 2006)

The premise behind DWI stroke imaging relies on the fact that cells must experience severely compromised blood flow to lack the energy needed to operate the membrane ion pumps. Because of this, the DWI lesions are considered to correspond closely to the ischemic core with permanent tissue injury. In a comprehensive review of DWI imaging Davis looked at papers which compared the sensitivity of DWI to UCT for the diagnosis of ischemic stroke and the majority found DWI to be superior especially when imaging is performed soon after the ischemic event.(Davis, Robertson et al. 2006)

Because DWI is only sensitive to areas of severe blood flow reduction, it is not able to accurately define regions of reduced blood flow corresponding to the penumbra. Alternative MR techniques are required to establish the boundaries of potentially salvageable tissue.

Often patients that present with stroke symptoms are scanned with a perfusion-weighted MR sequence in addition to the DWI sequence. The purpose of the perfusion-

weighted images is to attempt to gain an understanding of the penumbra by looking at areas where blood flow is reduced, but not restricted enough to result in breakdown of the cellular ion pumps. When both DWI and PWI are performed, the DWI lesion is considered the ischemic core, while the PWI lesion describes the penumbra.(Rivers, Wardlaw et al. 2006; Ryu, Lee et al. 2006; Schaefer, Copen et al. 2006; Parsons, Pepper et al. 2007) Perfusion-weighted imaging allows for computation of three important parameters, cerebral blood volume (CBV), cerebral blood flow (CBF), and mean transit time (MTT). CBV lesions correspond closely to the DWI lesion, with both methods describing the final infarction core well. Vary rarely do the two methods produce wildly different results. A more common mismatch is between the DWI lesion, and areas of reduced CBF or MTT. Unfortunately, some studies have shown that the size of the mismatch correlates well to the final lesion size (Karonen, Ostergaard et al. 2001), while others have not (Rivers, Wardlaw et al. 2006). Although somewhat controversial, the mismatch volume is still considered an important indicator for patient prognosis. In terms of defining the section of penumbra that will likely proceed to infarction and the sections that may be saved, the CBF values tend to be the most useful parameters to study, but are not perfect predictors.(Schaefer, Copen et al. 2006)

While MR DWI and PWI imaging together provide a good estimate of the infarction core and penumbral regions, natural variation in the CBF amongst different patients and variability in the CBF ratios between normal and hypoperfused tissue makes a prediction about future tissue viability difficult. In order to gain a better understanding about tissue viability, functional imaging methods have been researched for their abilities to categorize the penumbra and infarcted tissue using more direct techniques.

2.4.3 PET based Stroke Imaging Methods

Another parameter for analyzing ischemic tissue is the cerebral oxygen metabolism rate ($CMRO_2$). Currently, the only clinically approved way to measure this property is by using ^{15}O PET. The general PET stroke protocol requires three different scans, an initial scan using a constant infusion of $H_2{}^{15}O$, a second scan using inhalation of $^{15}O_2$, and a final scan with $C^{15}O$.(Guadagno, Warburton et al. 2004; Coles, Fryer et al. 2006) The three scans allow for computation of CBV, CBF, and $CMRO_2$ from which the ischemic core and penumbral regions can be inferred. Infusion of a constant flow of $H_2{}^{15}O$ allows determination of CBF due to the principles of freely diffusible tracers.(Baron, Frackowiak et al. 1989) During the continuous injection of $H_2{}^{15}O$, the arterial blood is sampled to obtain an approximation of the input function into the brain tissue. The tracer is assumed to reach equilibrium between the blood and the brain tissue immediately, so the tracer injected is matched by its removal into the venous circulation and decay. During this steady state process, the tissue activity is related to the input activity by the cerebral blood flow.(Baron, Frackowiak et al. 1989)

Cerebral blood volume can be calculated from a scan using ^{15}O-labeled carbon monoxide. The $C^{15}O$ binds to deoxyhemoglobin and provides a stable tracer for RBC distribution. Because the $C^{15}O$ does not release the deoxyhemoglobin, the fidelity of the tracer does not change during transition from arterial to venous blood, so direct arterial sampling is not necessary and venous sampling can be used. Introduction of the tracer into the body usually requires inhalation of a large bolus of gas. After complete

equilibration of the tracer into the blood, the measurement of CBV can proceed. (Baron, Frackowiak et al. 1989)

As other imaging methods possess the ability to obtain measurements of CBV and CBF, PET does not hold a major advantage for these examining these parameters. Where PET does offer improvement over other modalities is in measurement of oxygen metabolism due to its direct measurement of the transport of ^{15}O throughout the brain. The steady state model for oxygen utilization was derived and described by Lammertsma back in 1981 (Lammertsma, Jones et al. 1981), but the basic theory has remained the same. The regional $CMRO_2$ is a function of the flow rate, the extraction fraction, and the arterial concentration of molecular oxygen. Obtaining enough information for the calculation of $CMRO_2$ requires two scans and arterial sampling during each scan. The first scan requires measurement of the cerebral $H_2{}^{15}O$ concentration. This can be accomplished two ways; the older method uses inhalation of $C^{15}O_2$ which is converted into $H_2{}^{15}O$ in the pulmonary alveolar capillaries. The newer method uses an infusion of $H_2{}^{15}O$ directly into the venous system. With either method, a dynamic equilibrium is reached after a few half-lives of the ^{15}O tracer, where the incoming tracer is balanced by the decay and washout of outgoing tracer. During this steady-state the intensity in the PET images is proportional to the concentration of $H_2{}^{15}O$ in the brain.

The second scan requires continuous inhalation of $^{15}O_2$. The labeled oxygen becomes bound to deoxyhemoglobin upon inhalation and is transported via RBC to the brain. Thus the total activity in the brain becomes the sum of the activity due to $H_2{}^{15}O$ that is produced from metabolism of the molecular $^{15}O_2$, the $H_2{}^{15}O$ that is washed-out from the molecular $H_2{}^{15}O$ that was introduced via infusion or $C^{15}O_2$ inhalation, and the

hemoglobin-bound $^{15}O_2$. The information from these two scans allows the calculation of the oxygen extraction ratio (OER). The final value of oxygen metabolism ($CMRO_2$) is simply the product of CBF, OER, and the total blood oxygen content.(Frackowiak, Lenzi et al. 1980)

Because the oxygen metabolism is a direct measure of the functionality of neurons, it is important to determine how metabolism changes during ischemia, and how these changes relate to known markers such as DWI. In a paper from Guadagno, the authors explore exactly this to find the $CMRO_2$ within DWI lesions defined using MR.(Guadagno, Warburton et al. 2004) They found that generally, the region within the DWI lesion showed a decrease in oxygen metabolism, but there was significant variability suggesting that the DWI lesion may include areas of reversible and reperfused tissue. The authors conclude that measurement of perfusion is necessary to properly interpret the DWI lesion; the paper serves as a reminder of the limitations of solely using DWI for stroke imaging.

The summary of stroke imaging presented here has illustrated the progression of imaging techniques always striving to improve diagnostic accuracy and correctly characterize the complex tissue reactions during ischemia. We've seen that the best indicator of cellular function is measurement of oxygen metabolism, but this requires the use of very expensive PET machines, and the isotope ^{15}O; an extremely challenging isotope to use due to its short half-life. Potentially, if the oxygen metabolism could be assessed through MR, it would be far easier to obtain the proper information from a single MR imaging session. Such is the goal of work proposed by Lin in the form of an MR cerebral oxygen metabolism index (MR-COMI). All three techniques, DWI, PWI

and O-metabolism could be assessed within a few minutes in a single scanner. Unfortunately, because MR does not directly measure O concentrations, some apriori information is required including hematocrit values. Some research has examined hematocrit changes during ischemic conditions both in man and in animal models, but it remains incomplete and inconsistent.

2.4.4 Noninvasive Hematocrit Measurement for MR-COMI Imaging

The MR-COMI method requires local hematocrit values within the cerebral cortex. As directly sampling blood from within the brain is prohibitively dangerous and extremely difficult a noninvasive method for measurement is required. Currently, methods have been developed for both PET and SPECT for hematocrit measurement. Both are based upon the same biomarkers, red blood cells and plasma, but obviously require different tracers.

The earliest paper detailing a method for hematocrit measurement using PET was written by Lammertsma et al. in 1984.(Lammertsma, Brooks et al. 1984) Their objective was to define the cerebral-to-large vessel hematocrit ratio, which was poorly defined and varied from 0.5 to 0.92. Using ^{11}CO bound to deoxyhemoglobin as an RBC tracer and ^{11}C-albumin as the plasma tracer, they derived a method for Hct calculation. They found that mean cerebral hematocrit levels were 0.28 with mean arterial Hct levels of 0.4. Overall, the cerebral-to-large vessel ratio was approximately 0.7 in humans.

In a study examining cerebral hematocrit levels in patients diagnosed with chronic internal carotid artery occlusion, Yamauchi turned to C^{15}O and ^{62}Cu-HSA as PET labels for red blood cells and plasma respectively. They found no significant difference in the values of Hct between the cortex ipsilateral and contralateral to the ICA occlusion. They

found that cortical hematocrit for both hemispheres was 0.34+/- 0.02. Using PET, they were able to perform images for CBF, $CMRO_2$, OEF, CRCV, and CPV. They found marked reductions in CBF within the ipsilateral hemisphere from 34.3+/- 4.6 mL/min to 27.1+/5.4 mL/min. They also saw a decrease in $CMRO_2$ and an increase in OEF.

Performing a stepwise regression analysis using CBF, OEF, $CMRO_2$ and large vessel Hct, they found a correlation of 0.864 for cerebral Hct. The regression showed that the majority of the variance (42%) in cerebral Hct levels came from large vessel Hct, but CBF and $CMRO_2$ accounted for 32% of the variance as well. Cerebral Hct levels were positively correlated with CBF and negatively correlated with OEF. They inferred that in patients with decreased CBF and increased OEF hematocrit would be decreased.

Yamauchi was unable to explain the mechanism for changes in Hct directly, but saw that the blood volume in the lesion hemisphere increased with plasma making up the majority of the increase in volume. Their analysis suggested that decreases in blood flow increased the thickness of the cell-free plasma layer of the vessels. The lower perfusion pressure results in dilatation of the cerebral vessels and decreased blood velocity (Gibbs, Leenders et al. 1984; Powers, Grubb et al. 1984).

In two papers examining changes in hematocrit levels during the acute stages of stroke, increases in Hct were seen in the ipsilateral hemisphere (Loutfi, Frackowiak et al. 1987; Sakai, Igarashi et al. 1989). The methods used by Sakai and Loufti were similar in that they both used the same two tracers, ^{99m}Tc-RBC and ^{99m}Tc-HSA, but Sakai chose to wait 48hr for the first tracer to decay before injecting the second. Due to the delay in injection, his methods will not allow examination of Hct during the acute phase of stroke, which occurs during the first 3 to 6 hours.

The work performed by Loutfi provided the techniques used in this work for hematocrit measurement using SPECT. By using ^{99m}Tc to label both plasma and red blood cells, the image intensity using SPECT was proportional to the volume of the blood component and the concentration of the labeled tracer.

For the case when the plasma tracer ^{99m}Tc-HSA was administered first, the number of counts within an ROI drawn in the SPECT image is proportional to the plasma volume contained within that ROI, the concentration of ^{99m}Tc-HSA within the plasma and the attenuation, scatter, and detector response factors. The plasma volume can be expressed in terms of hematocrit as

$$Vp = (1-h)Vwhole \tag{1}$$

Where V_{whole} is the whole blood volume and h is hematocrit. By using blood samples counted in a well counter to ascertain the ^{99m}Tc-HSA concentration, the image counts for the plasma tracer are

$$Pc = (1-h)Vwhole * Pw * K \tag{2}$$

Where Pc is the plasma image counts, Pw are the well counts for 1mL of plasma and K is a correction to account for the efficiency of the well counter. Analogously, the equation for the ^{99m}Tc-RBC image is:

$$Rc = hVwhole * Rw * K \tag{3}$$

In the case where ^{99m}Tc-HSA is injected first, the image intensity for the first scan is defined in (3). For the second scan, however, the image intensity will be proportional to the decayed signal left over from (3), as well as new counts from the addition of the ^{99m}Tc-RBC tracer. The equation for the second scan can be written as:

$$Pcl + Rc = (1-h)Vwhole * Pwl * K + hVwhole * Rw * K \tag{4}$$

The decayed signal from the plasma tracer is shown as P_{cl}, and the decayed plasma counts as measured in the well counter are P_{wl}. The two equations from the two SPECT scans leave us with two unknowns, K and h. By dividing the two equations, the K term and whole blood volume will cancel and we will be left with an expression for h.

Equation (5) provides a calculation for hematocrit values dependent upon image counts in

$$\frac{Pc}{Pcl + Rc} = \frac{(1-h)Pw}{(1-h)Pwl + hRw} \qquad (5)$$

each image, the blood sample counts, and hematocrit levels. Solving for hematocrit we see that:

$$h = \frac{1}{x+1} \qquad x = \frac{PcRw}{Pw(Pcl + Rc) - PcPwl} \qquad (6)$$

Equation 6 provides hematocrit values given the image counts and blood sample counts obtained from the experiment. Using this method, Loufti examined three control patients, six patients with transient ischemic attack (TIA), and nine patients with acute hemispheric stroke. They found that the cerebral hematocrit was lower than large vein hematocrit with cHct to lvHct ratios ranging from 0.65 to 0.90.

Consecutive transaxial slices were chosen for ROI analysis in each patient. An ROI was drawn in each hemisphere and paired t-tests were used to determine any difference in mean hematocrit level. For the control patients and the patients with TIA, no significant difference was seen between the affected and the contralateral hemisphere. For patients with stroke, 4 of nine patients showed increased hematocrit levels, with 5 of 9 showing no change. In one patient, they performed two scans, with the first immediately after the onset of stroke showing increased Hct in the affected hemisphere.

The second scan, however, showed no difference in Hct levels between hemispheres indicating that any physiological changes during the acute phase are temporary and other compensatory methods, such as opening of collateral channels will eventually act.

For the work in this dissertation, the methods of Loutfi were used as a template for rat experiments. Section 3.4 will detail the methods used for the calculation of hematocrit in ischemic rats. The work performed in humans, however, showed that successful measurement of Hct within rat cerebral cortex is possible given appropriate camera resolution. The literature seems to suggest an initial increase in Hct levels during ischemic conditions as decreases in CBF reduce the oxygen supply and Hct levels rise to compensate. Over time, however, hematocrit levels return to normal or perhaps even decrease as changes in physiology attempt to regulate CBF. The experiments detailed in Section 3.4 will help to clarify the acute changes in blood viscosity in a more controlled animal model.

Chapter 3

Methods

3.1 A Dual-Plane Orbit Approach for Improved Pinhole Tomography

The pinhole collimator improves upon limitations inherent to the detection of high energy photons with respect to resolution and sensitivity. Naturally, with these improvements, tradeoffs must be made with respect to other imaging parameters. The most important tradeoff affecting pinhole imaging is the sacrifice of data completeness for improved resolution and sensitivity.

As stated earlier in Chapter 2, the pinhole only allows for complete data along the central plane of the aperture. All other regions that lie above or below this plane suffer from decreased data integrity with the problem worsening with increasing distance from the pinhole plane. The decreased integrity of the projection data for these axial planes result in reconstruction artifacts due to misestimating the true distribution of the object. The only way to recover this missing data is to use a camera orbit that includes some axial motion component. This work will introduce and validate a method using multiple, parallel, circular orbits at various positions with respect to the center of the object to improve upon the inherent limitations of the pinhole collimator.

3.1.1 Dual Plane Simulations

The dual-plane imaging protocol for pinhole imaging is designed to increase the axial FOV and reduce the axial distortions inherent to pinhole collimation. We assessed the hypothesis that the dual-circular orbit will result in greater axial coverage and fewer aliasing artifacts than a standard single orbit. Figure 3.1.1 shows a schematic of the dual-circular orbit arrangement.

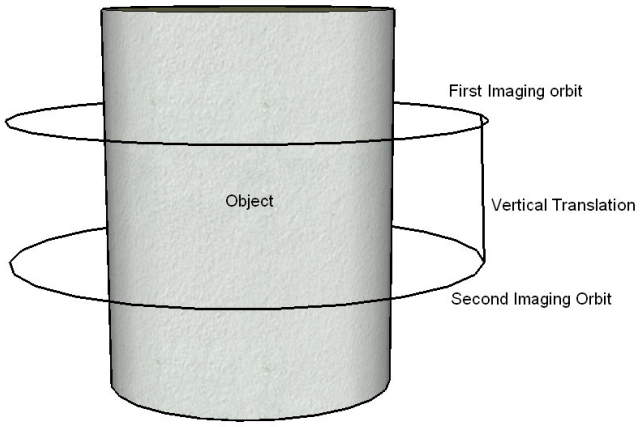

Figure 3.1: Schematic of the orbit arrangement for Dual-circular plane pinhole imaging. A standard circular orbit is performed with the object offset slightly in the axial direction. A vertical translation is used to reposition the object for a second scan to complete the acquisition.

The orbit paths shown in Figure 3.1 allows for the object to be divided into 2 portions with each portion being sampled separately. Each set of projections only covers approximately half of the object, with the amount of overlap between projection sets dependent upon the vertical translation distance, the radius of rotation and the cone angle of the pinhole. Because the OSEM algorithm tends to minimize the error between the real projections and the updated projections based on the algorithm's expected distribution, using both sets of projection data simultaneously will not result in adverse effects during the reconstruction. The algorithm will simply take both projection sets into

account and update the total distribution estimate accordingly. This is true as long as the geometrical parameters used are correctly determined. Mismatches in the true parameters compared to the measured or assumed parameters, especially regarding the translation distance will result in large image artifacts and poor reconstructions. For the computer simulations, a phantom based on the Defrise design of alternate hot and cold planes was used. The phantom was 5cm long and simulated on a 100^3 matrix. The detector was simulated as a square 100^2 array. The dimensions of the phantom were set so that the size of the phantom and of the individual hot planes were similar to that of a physical microDefrise phantom used for SPECT imaging.

The initial simulations were performed using a standard circular orbit centered about the object. The focal length of the pinhole collimator was 10cm, and the object distance was also simulated at 10cm for a magnification factor of one. Ninety projections over 360^o were simulated and reconstructed using the OSEM algorithm. To increase the axial distortion, the object distance was shortened from 10cm to 5cm, increasing the magnification factor to 2. This has the effect of utilizing more of the detector area to sample the object and allows the uppermost and lowermost detector elements to play a role in the projection sampling. We expected this to increase the axial distortions and increase the reconstruction artifact.

Simulation of the dual-plane orbit was simulated using the same detector and camera parameters as before, with 10cm focal length, 5cm object length, and a 100^3 matrix. Detector size was also 100x100 with a 0.1cm element which provides for a 10cm detector FOV. When the object length was simulated at 5cm, the camera FOV was also 5cm, perfectly matching the dimension of the phantom. While the pinhole aperture and

camera orbit were centered about the object in the single orbit scan, for the dual-orbit scan, the camera was shifted a distance of +/- 1.25cm in the axial direction for the two acquisitions. This distance was chosen somewhat arbitrarily, but geometrically divides the object into two equal halves with each orbit in the center of an object 'half.'

The first set of simulations provided for a reasonable comparison between a standard orbit, and a crudely designed dual-orbit scan, but was expected to demonstrate proof-of-concept for further evaluations. The second set of simulations was designed to answer the question of choosing the optimal shift-distance or pitch, given a set of detector and object parameters.

For consistency, the same disc phantom was used along with the same detector and object parameters. The variable for these simulations was the pitch, which was varied from 0.625cm to 5cm. The hypothesis was that shorter pitches would perform better for the center of the object while longer pitches would trade-off accuracy in the object center for accuracy at the object edges. Reconstruction accuracy was evaluated using profiles drawn along the axial direction and comparing reconstruction image values to the true phantom values. The phantom was divided into 5 equal regions corresponding to the dark regions of the phantom for the analysis. The dark regions were chosen for analysis to avoid cone-beam artifacts. The cone-beam artifact is another aberration due to the oblique angle of the sampling rays. It represents as an abnormally bright region in the image near sharp transitions or areas of high contrast. Because there are no negative cone-beam artifacts, by analyzing dark image regions, any errors are attributable to the dual-plane reconstruction process and not general pinhole artifacts. From the set of

simulated pitches, the reconstruction with the lowest overall error throughout the image was chosen as the optimal.

3.1.2 Dual Plane Experimentation

Having simulated the dual plane orbit approach and determining the appropriate pitch given an object size and detector parameters, a physical phantom was scanned using the microSPECT system fitted with a 1mm pinhole. The phantom consisted of 5 hot discs separated by 4 dark discs very similar in design to the simulated phantom. Phantom height was 5cm and width was 4.5cm. A baseline acquisition was taken with the pinhole and detector centered about the object with a single circular orbit. Ninety projections were taken over 360 degrees. The detector consists of 66 elements 1.6mm wide for a total FOV of 105mm. The collimator focal length was 10cm, and the object was placed a distance of 5.5cm from the aperture to avoid transaxial truncation in the projection. The projections were reconstructed using OSEM with 5 iterations and 6 subsets.

Dual-plane acquisitions were performed using the same object length, but object pitches were +/- 1.25cm and +/- 2.5cm. These pitches were chosen to approximate the optimal geometry. Due to uncertainty with object positioning and the detector geometry, the approximations were used to validate the approach concept, and not to generate optimized reconstructions.

A major difference between the simulated data and the experimental data was the shape of the detector. For the simulations, the detector was simulated as a 100x100 square, while the microSPECT uses a circular detector. The shape of the detector plays an interesting role in the regional sampling rates of the object, due to varying width of the detector FOV along the circle. The center of the detector possesses the widest FOV, with

the FOV narrowing toward the edges. The circular geometry adds an additional complexity to the sampling completeness as the sampling rate changes with the area of overlap between the two projection FOVs. In effect, the area visible in both projection sets is counted twice resulting in lower noise levels than the outside regions. This is illustrated in Figure 3.2.

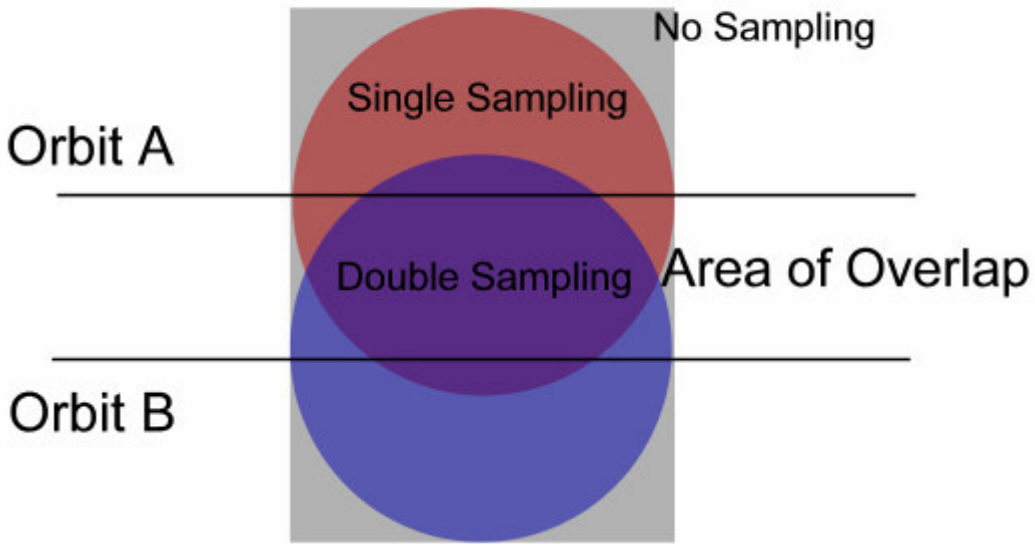

Figure 3.2: Sampling pattern of dual-orbit pinhole tomography using a circular detector. Object is seen in grey, orbit A FOV in red and orbit B FOV in blue.

Because of this variability in sampling completeness across the field-of-view, more simulations were performed using a circular FOV to try to find the optimal pitch for a circular detector.

3.1.3 Circular Detector Simulations

The procedure described in section 3.1.1 was performed again, but a circular mask was applied to the projection sets prior to reconstruction. Poisson noise was also added to the projections to simulate the varying noise characteristics due to variable

sampling rates. Noise levels were added assuming an average of 40K counts per projection, which is a typical value acquired with the microSPECT system. The pitch length was varied from 6.25mm to 50mm. Reconstruction accuracy was measured using the same profile technique described in section 3.1.3. The optimal pitch was defined as that resulting in the reconstruction with the lowest overall error over the entire image.

The simulations and experiments performed were designed to show the improvement of a dual-circular orbit approach when compared to a standard circular orbit. The optimal pitch geometry for both square and circular detectors was evaluated and the accuracy of the dual-plane method compared to a single orbit determined. The next section will detail another atypical orbit approach designed to increase the transaxial FOV and allow for shorter object distances.

3.2 Dual Axes of Rotation orbit for truncation correction

Because pinhole collimators rely on magnification to improve resolution and sensitivity, the field-of-view suffers and the object size is limited. Moving the object closer to take greater advantage of the pinhole geometry introduces truncation into the projection images which will result in reconstruction artifacts. By adding a second scan and using axes of rotation that are offset from the center of the object, complete data can be acquired even though the object is larger than the available FOV. The tested hypothesis was stated as follows: Image resolution and sensitivity will be increased using the dual-AOR approach relative to a standard pinhole orbit. The hypothesis was tested using both simulation and experimental approaches.

3.2.1 Dual AOR Simulation Procedure

A Jaszcazk phantom 5cm in diameter and 5cm tall was simulated to test the reconstruction accuracy of the dual-AOR procedure. The camera geometry was simulated to mimic that of the microSPECT system at UNC. Camera FOV was 10cm and pinhole focal length was also 10cm. A baseline scan using a standard circular orbit was simulated using an object length of 5cm with the axis of rotation centered with respect to the pinhole aperture. Using this geometry, the camera FOV matched the object size exactly, maximizing the detector area used without introducing truncation into the projections. The projection set consisted of 128 images over 360^{o}. After simulation of the projection set, Poisson noise was added to simulate a projection set of 40K counts/projection. The OSEM algorithm with 5 iterations and 8 subsets was used to reconstruct the noisy projection set.

The simulation procedure utilized an ideal pinhole collimator and does not account for aperture size or septal penetration. As such, the resolution of the reconstructed images depends primarily upon the number of pixels devoted to sampling the object in the projection space. As the number of pixels available to sample the object is dependent upon the magnification factor of the acquisition geometry, the resolution of the reconstructed image is only dependent upon the object length of the system for this simulation. Because the dual-AOR methodology only improves resolution by shortening object length, this simulation procedure is adequate for testing the method.

A second simulation was performed using a single orbit scan with the object and axis of rotation again centered about the pinhole. For the second simulation, however,

the object length was halved to limit the camera FOV thereby introducing truncation into the projection set. Again, 128 projections were simulated and Poisson noise equivalent to 40K counts projection added. The projections were reconstructed using OSEM, 5 iterations and 8 subsets. The truncated single orbit image was necessary to establish the artifacts resulting from truncated projections.

The third simulation used the dual-AOR procedure to compensate for the truncated projection data. Two orbits were simulated with both using a 2.5cm object length. Each of the two orbits used a shift in the position of the axis of rotation with respect to the pinhole center. The object center was kept aligned with the axis of rotation which had the effect of the camera viewing only one side of the object. As the object rotated about the axis of rotation, the portion of the object viewed by the camera changed. As such over an entire rotation, the camera sampled every point in the object, but did not have every object point sampled with every projection. The second scan used a symmetrical shift about the pinhole so that the camera saw the other half of the object. Between both scans, the entire combined projection set contained the complete data necessary to reconstruct the object. For voxels that were missing in some views in one of the two scans, the data would be recovered with the second. The hypothesis for this simulation stated that the combined projections would allow for imaging at the shorter object distance without the corresponding truncation artifacts.

Reconstruction of the two projections was again accomplished using the OSEM algorithm. The structure of the algorithm allowed for separate geometry matrices for each scan. As the algorithm progressed through the iteration, the projection and backprojection steps would utilize the data from both projection sets. In this manner the

algorithm would reconstruct the object using data from both projections sets. The OSEM reconstruction algorithm plays a critical role with the dual-AOR approach as incorporating data from multiple projections sets is impossible using analytical approaches.

3.2.2 Optimizing the shift distance for the dual-AOR geometry

Using multiple orbits introduces a new variable into the geometry with the distance the axes of rotation are shifted. We can clearly see that at the extremes of a zero shift, and a very large shift we will not obtain quality reconstructions. For the orbit to work, it is imperative that both orbits include the projections required to meet Tuy's or Orlov's sufficiency criterion. Proper characterization of the dual-AOR orbit requires an examination of the optimal shift given a specific object size and camera FOV.

The shift distance was defined as the total distance between the two axes of rotation. Both shifts were kept symmetric about the pinhole aperture. The optimum shift distance was expected to divide the object equally between the two scans. For example, using a 5cm diameter object, a 10cm focal length pinhole and a 10cm FOV detector, placing the object as close as possible to the aperture would result in a 2.5cm object length as the object would then be touching the aperture. The camera FOV at the origin containing the axis of rotation and the center of the object would also be 2.5cm. In this example, only the center half of the object is visible and the outer 1/4ths are beyond the FOV. By shifting the AOR by +/- 1.25cm each acquisition would see complementary halves of the object and the entire object would be covered. If the shift were either smaller or larger, gaps would be left within the coverage and artifacts would arise. Figure 3.2.1 illustrates the effects of shift distance on the sampled volume.

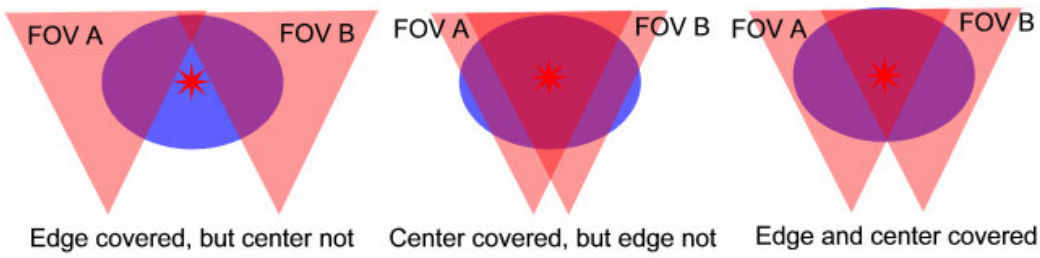

Figure 3.3: The dual-AOR orbit is equivalent to shifting the camera with respect to the object. The axis of rotation is denoted with a red star. For complete data to be acquired, both one side of the object and the AOR must remain in the FOV, otherwise gaps in coverage appear.

To find the optimum geometry for the dual-AOR orbit, various shift distances were tested. Each shift distance was expected to provide a specific tradeoff between providing complete data at the center of the object or providing complete data toward the edge. The optimum shift was defined as the geometry that provided the reconstruction that most faithfully reproduced the original phantom. Only the central transaxial reconstruction slice located at the central plane of the pinhole was measured to avoid pinhole axial sampling effects. The metric used for image quality evaluation was a simple difference between the original phantom and the reconstructed image. All simulations for this experiment were simulated noise free to establish any problems arising from the reconstruction algorithm and orbit path. Table 3.1 shows the entire simulation schedule for the dual-AOR experiment.

The initial simulation plan was designed to identify any major flaws with the dual-AOR procedure and establish the potential to create artifact-free reconstructions from truncated data sets. The next section will examine the method using real data obtained from the microSPECT system.

Table 3.1: Simulated dual-AOR images. Pixel size and detector matrix were chosen to match the microSPECT camera for maximum translatability between simulation and experiment. Pixel size was 1.5mm, and detector matrix was 66x66

Pitch (pixel)	Pitch (mm)	Focal Length(cm)	Object Length (cm)	Detector FOV (cm)
10	15	10	5	10
15	22.5	10	5	10
20	30	10	5	10
25	37.5	10	5	10
30	45	10	5	10
40	60	10	5	10

3.2.3 Dual-AOR orbit reconstruction experimental procedure

True projections do not provide ideal data and are affected from statistical noise related to the number of counts in the projection bins. Another complicating factor is the lack of accuracy and precision regarding the geometry of the camera and object in real life. Mismatches between the true geometry and the assumed, or calculated geometry will result in reconstruction artifacts. Doubling the number of orbits also increases the number of potential mismatches, and the severity of the ultimate reconstruction artifacts unless careful calibrations are performed. Nonetheless, a procedure that provides good results within the strict environment of a simulation, but cannot translate to the real world is not worth development. In order to find the real-world potential of the dual-AOR method, experiments must be performed.

The basic procedure for the experiment closely followed the procedure used for the simulations. The microSPECT camera uses a pinhole collimator with interchangeable apertures. For this experiment the smallest aperture 0.75mm was used to provide the best possible resolution. A micro-deluxe phantom (Data Spectrum, Hillsborough NC) was filled with 5mCi ^{99m}Tc and placed 7cm from the aperture for truncation-free projections.

Sixty projections over 360^{o} were acquired and reconstructed using OSEM with 5 iterations and 6 subsets. The average projection contained approximately 30000 counts.

The object was then moved 2cm closer to the aperture to induce truncation in the projections. The center of the object was kept approximately in line with the AOR and the AOR was centered about the aperture. Again sixty projections were acquired and reconstructed using the same parameters. This particular scan was to establish the extent of truncation artifacts and provide a basis for comparison with the dual-AOR scan.

The third scan used the same geometry from the truncated single-orbit scan, but the AOR and object center were shifted 1cm with respect to the pinhole. SPECT was performed again acquiring 60 projections. The fourth and final scan was performed after shifting the AOR and object center 1cm in the opposite direction with respect to the pinhole. The 1cm shift distance was chosen somewhat arbitrarily because the exact FOV and object length are known only approximately. The FOV of the camera for the experimental magnification level was large enough to cover both the edge of the object as well as the center, so the entire should be covered between both scans. The purpose of the experiment was not to maximize the effect of the dual-AOR orbit, but merely to attempt to properly fuse the two projections sets and demonstrate the basic feasibility. For this reason, a conservative geometry was selected with minimal truncation.

The dual-AOR pinhole orbit was conceived as a method to improve the resolution and efficiency of a single pinhole gamma camera. By shortening the object length and increasing magnification, the camera performance should improve over a standard single orbit scan. Both simulation and experimental methods were applied to determine both

the theoretical and practical limitations of the method and to better evaluate the utility of the method.

3.3 SPECT Imaging for ANCA-induced Kidney Nephritis

The next two sections will detail the methods used for two small animal applications. Instead of a theoretical evaluation of a method, the next sections attempt to answer physiological or biological hypothesizes.

The chemistry for radiolabeling proteins with radiotracers, either iodine based or technetium based has been well documented. This mature chemistry makes SPECT an attractive modality for molecular imaging. Chapter 2.3 detailed the background behind ANCA-induced nephritis and mouse models designed for experimentation of this disease. Most research using these animal models requires sacrificing the animal and performing histology tests to evaluate and diagnose the disease progression. An imaging method which could allow noninvasive monitoring of the disease progress would dramatically decrease the number of animals needed, and improve the statistical significance of the mice used due to lower interanimal variation.

Ideally, development of a tracer for ANCA-induced nephritis would allow SPECT to provide the non-invasive measurements. Previous work on the ANCA model mice has identified a probable protein suitable for radiolabeling. Myeloperoxidase is a signaling protein for neutrophil activation and exists in large concentrations in regions of upregulated neutrophil activity. An antibody against myeloperoxidase would provide the desired tracer for the proposed target. Potentially, an anti-myeloperoxidase tracer along with an imaging system capable of resolving the mouse kidney would provide the desired

non-invasive measurement. Validation of a tracer requires a series of robust experiments to confirm the specificity and sensitivity of the tracer to the biomarker. Before progressing to the full ANCA-model, the proposed tracer was evaluated for a more general infection model to ensure the *in vivo* behavior of the tracer.

3.3.1 Staph-A infection model for MPO

Several variables affect the biodistribution of a tracer within an animal including the injected mass, the affinity of the tracer for the desired target, the affinity of the tracer for secondary targets and the ability of the tracer to overcome any obstacles to the target. To examine these factors, a mouse infection model was developed to encourage a controlled region of increased neutrophil activity. Initial experiments utilized a subcutaneous injection of $5x10^6$ Staph-A cells into the left thigh. Inert phosphate-buffered-saline (PBS) was injected into the right thigh subcutaneously. The infection was allowed to incubate for 24 hours prior to injection of the imaging tracer. These early experiments showed that the tracer did not penetrate through the tissue between the blood stream and the subcutaneous injection site. This was an excellent example of a physiological obstacle for the tracer.

Because of the inability of the tracer to penetrate to a subcutaneous infection, the model was altered by substituting an intramuscular injection into the right thigh instead of subcutaneous injection. The infection was again allowed to incubate for 24 hours, but the bacteria mass was decreased because of the increased potency of an intramuscular infection. A negative control was provided from an intramuscular injection of PBS into the left thigh.

Two tracers were tested using the intramuscular staph infection model. The tested tracer was based on an antibody against myeloperoxidase, while the second was based upon polyclonal immunoglobulin (IgG). Both tracers were labeled with ^{99m}Tc using the Isolink chelating agent (Isolink®, Mallinckrodt B.V. Petten, The Netherlands). The immunoglobulin tracer was expected to act as a positive control to verify the ability of a similar sized molecule to reach the infection site and accumulate.

The anti-myeloperoxidase tracer was expected to show increased specificity over the immunoglobulin tracer because the staph-A infection initiates a neutrophil dominated immune response and was expected to show increased concentrations of myeloperoxidase due to neutrophil burst. No attempt was made to quantify the uptake within the infection region for the earlier mice, so evaluations were based upon visual inspection of the reconstructed images. The lesion uptake in the last few mice was semi-quantitated using the lesion/liver uptake ratio as the liver uptake was deemed to be consistent for all animals. The lesion/liver uptake ratio also controls for injected dose and animal size making it a suitable metric.

The tracer was allowed to circulate for 24 hours before imaging to allow the background levels to subside and ensure sufficient time for the antibodies to infiltrate the infected region and bind to the target molecules. The animal was sacrificed prior to imaging via cervical dislocation and mounted vertically in front of a high-resolution parallel-hole collimator. The parallel-hole collimator was used to increase the sensitivity of the tracer, which had undergone 4 half-lives prior to imaging. The low residual activity levels necessitated a long imaging time of 90 minutes per animal which necessitated the sacrifice of the animal. The resolution of the collimator at a distance of

3cm was 2.2mm FWHM. Sixty projections were acquired over 360^{o} and reconstructed using OSEM with 5 iterations and 6 subsets. Eight mice were used for this experiment with half receiving the anti-MPO tracer and the other half receiving the IgG tracer.

3.3.2 MPO-/- mouse experiment

An additional experiment was conceived to provide an extra level of control for the specificity of the tracer. Mice bred to not exhibit the myeloperoxidase protein were used for the same staph-A experiment. The hypothesis was that mice without myeloperoxidase would not offer a suitable target for the anti-MPO tracer. Any uptake of the anti-MPO tracer within the staph-A lesion would therefore be attributable to secondary targets. Because the ultimate goal of imaging within an ANCA mouse necessitates a tracer with high specificity, failure of this experiment would provide strong evidence to eliminate the tracer for consideration.

Three MPO-/- mice were obtained for this experiment with one receiving the IgG tracer and two receiving anti-MPO tracers. All other experimental procedures were identical as for the wild-type mice. Staph infection was induced via intramuscular injection and tracer injection was performed 24 hr later. Approximately 1mCi of the tracer was injected in 0.2mL via retroorbital injection. As this experiment requires a quantitative assessment of the difference between the two tracer types, the lesion/liver uptake ratio was used as the metric.

The experiments detailed in this section were designed to evaluate and validate a novel new tracer for imaging sites of inflammation and neutrophil activation. Both wild-type and knockout mice were used to assess the specificity of the anti-myeloperoxidase

tracer. The results of these experiments will provide the justification for future work developing the method for the complete ANCA-induced nephritis model

3.4 Hematocrit measurement in ischemic rat brain using SPECT

Hematocrit measurements typically require a blood sample to be drawn from the animal and centrifuged to separate the two blood components. The Hematocrit measured then applies to the vessel from which it was drawn, but provides no information regarding regional hematocrit values which may differ from large vein values. When measurement of local hematocrit levels within an organ is required, direct methods are not appropriate and *in vivo* methods must be used. Using a tracer for erythrocytes and a tracer for plasma, SPECT provides the ability to noninvasively assess the relative proportion of blood components and then derive hematocrit.

3.4.1 Initial experiments utilizing the preload method

Measurement of hematocrit using SPECT requires two tracers, one for each blood component. The tracers chosen for this experiment were ^{99m}Tc-Human Serum Albumin (^{99m}Tc-HSA) for plasma, and ^{99m}Tc-Red blood cells (^{99m}Tc-RBC). The image of each tracer should be proportional to the volume of the labeled component. By inducing ischemia within the rat, any change in volume of the individual components can be assessed through the images. Ischemia was induced via an occlusion at the origin of the middle cerebral artery which reduces blood perfusion to the affected hemisphere.

In order to accurately measure changes in tracer concentration within the ischemic region, the tracer must first have access to the region or signal will not be available to measure. The ability of collateral vessels to compensate for MCA occlusion was uncertain, so to ensure tracer distribution to the ischemic region, the preload technique

was developed. Injecting tracer prior to vessel occlusion allows the probe to circulate throughout the body and reach equilibrium in the tissue, this technique was defined as preloading. After the preload phase, the occlusion operation was performed and ischemia induced.

Only a single probe can be preloaded within an animal because both tracers utilize the same radioisotope. Thus populations of rats must be imaged for each component probe. By pooling the data obtained from each population the average blood component volume can be measured and from those measurements, hematocrit values can be inferred. This method prevents the hematocrit level within a rat to be calculated since each rat only receives a single tracer. However, since the ischemic lesion only occupies one hemisphere, the other hemisphere is left normal and acts as a control measurement. By comparing the lesion hemisphere to the control hemisphere, changes in blood component volumes are attributable to the ischemic conditions.

Ischemic durations of 30min MCAO, 90min MCAO and 120min MCAO were evaluated. All rats were anesthetized using 133µg/kg chloral hydrate injected intraperitoneally every 45 minutes. Anesthesia was maintained throughout the experiment from injection of tracer until the completion of imaging when the animal was sacrificed.

A third tracer, ^{99m}Tc-hexamethylpropylene-amineoxime, ^{99m}Tc-HMPAO, was used to obtain perfusion images of the brain to establish the regions affected by the occlusion. HMPAO passes through the blood brain barrier in a lipophillic state and can pass readily through the cellular membranes into the endothelial tissue and parenchyma. Once the tracer interacts with the intracellular environment, it becomes hydrophilic and

no longer can pass through the cellular membrane. This causes the tracer to become fixed to the tissue so areas with higher perfusion rates become brighter and areas of reduced perfusion are darker when imaged with SPECT. The HMPAO image was always performed after the blood component image because the radiotracers were the same. The HMPAO images then show clearly where the extent of the perfusion defect is so that appropriate regions of interest for quantitative analysis could be defined. The entire experimental sequence is shown in Table 3.2.

Table 3.2: Preload experiment imaging protocol

Preloading Procedure	Time after occlusion
Tracer Prep: Withdrawal and label of RBC/ Label and chromatography of HSA	- 2hr (before occlusion)
Injection of Tracer	-30min
MCAO operation	0min
SPECT imaging I	30min
SPECT imaging II	90min
SPECT HMPAO imaging	120min

Using the HMPAO perfusion images as a guide, the anatomical regions were applied to the blood component images to calculate the average image intensity and pixel variance within the region of interest. Comparison of the lesion ROI to the control ROI using t-tests allowed for significant differences between the two regions to be identified. The comparison was repeated for both probe images and for each of the ischemic groups.

During each acquisition, blood samples were drawn using a catheter inserted into the femoral vein. The blood was then measured using a well counter to determine the

amount of activity per unit volume. This value was used to help calibrate the image intensity to a volumetric measure. The calibration between the well count result and the image result was performed using a simple point phantom of known activity. The phantom was imaged with the SPECT using the same imaging parameters as the experiment and then placed in the well counter for activity measurement.

Because the method did not allow for determination of Hematocrit levels within a single rat, a second study was devised to allow direct calculation of hematocrit. The second study will detail a method for administering both component probes into a single rat and calculating the Hematocrit levels.

3.4.2 Noninvasive Hematocrit calculation using SPECT

Noninvasive measurement of hematocrit within the rat cortex required a complex methodology for accurate quantification. Because hematocrit is a ratio of two values, normal image correction methods such as attenuation correction or detector response correction are not necessary. All of those factors are normalized since they remain constant for both images. Because most of the physical variables are normalized by using two scans, the image intensity depends only upon the injected tracer activity, the scan duration, and the biodistribution of the tracer. Blood samples allow for accurate measurement of the injected tracer activity, the scan duration is easily controlled so the only dependent variable left is the biodistribution of the tracer.

Loutfi, et al. described a method for Hematocrit calculation using SPECT and the ^{99m}Tc-RBC and ^{99m}Tc-HSA tracers. We remember from Section 2.4.4, that the process requires multiple sequential scans with blood samples taken during each acquisition. For the first scan, the image intensity is proportional to the blood volume, the specific activity

of the blood, and the detector efficiency. During the second scan, the image intensity is now proportional to the blood volume and the specific activity of the second tracer, the decayed remnants from the first tracer and the detector response. Ultimately, the hematocrit calculation is represented as

$$h = \frac{1}{1+x} \qquad x = \frac{PcRw}{(Pcl + Rc)Pw - PcPwl} \qquad (1)$$

Three groups were tested during this experiment: control group with no MCAO operation, 90min MCAO duration, and 90min MCAO duration with 120min reperfusion period. Five rats per group were scanned using both tracers along with an HMPAO perfusion scan performed last. Tracer activities were approximately 10mCi for each tracer with the HSA tracer administered first. Injection of the HSA tracer first allows for more convenient blood sample measurement. After centrifugation, the plasma rests above the packed cell mass and is easier to draw off using a micropipette tube. During the second acquisition for each rat, when both tracers are present, sampling of the decayed plasma sample is trivial as it rests on top of the column. When RBC is injected first, it is difficult to sample the decayed RBC cells without some mixing of the plasma. Centrifugation usually results in incomplete separation with 4-5% of the plasma activity remaining suspended within the packed cell mass.

The samples contained too much activity to be counted immediately after drawing the blood, so they were stored for ~48 hours to allow for decay. When the samples reached a suitable activity, they were counted in a well-counter using a 20% ^{99m}Tc energy window. Each sample was counted for 1 minute with during which 75K – 150K photons were counted.

The three images acquired for each animal were reconstructed using OSEM with 5 iterations. Post-reconstruction filtering was applied using a 5^{th} order Butterworth filter with 0.21 cycles/pixel cutoff. The HMPAO perfusion image showed the volume of reduced blood flow signifying the ischemic lesion. Three consecutive coronal slices within the ischemic region were chosen for volumetric ROI analysis, with equally sized regions drawn manually in both lesion and normal areas. Because the rat did not shift between scans, the regions of interest drawn using the HMPAO image could be applied directly to the RBC and HSA images.

3.4.3 Statistical Analysis

The experiments were designed to answer two main questions: Does hematocrit change within a rat during ischemic conditions? And does the duration of ischemia play a role in any hematocrit changes? The answer to the first question requires a comparison between measurements taken within the ischemic lesion and measurements taken in the contralateral control hemisphere. The answer to the second question involves analyzing the group properties for differences in the lesion/control hematocrit ratio.

Drawing volumetric regions of interest allowed for comparison both within an animal and between animals or groups. By treating each voxel within the ROI as an independent sample, t-tests were be used to determine significant differences in means between the lesion ROI and the control ROI within a rat. Because the number of voxels within an animal was quite high, this method provides high power for detecting significant differences in means. Also, by treating each ROI pair as independent samples, each rat will provide a single pair and the lesion-control difference for the group can be analyzed using rank-sum tests.

For comparison of hematocrit changes between groups, the lesion/control ratio of the volumetric ROI means provides a more convenient metric. ANOVA analysis using the lesion/control ratios were used to determine any statistically significant differences between any of the three groups. Tuchy's test was then used to determine which groups were significantly different from the others. ANOVA analysis also allows for comparison of variance between inter-group measurements and between group measurements, which helps add perspective to the clinical significance of the results. Spearman rank tests were used to evaluate the correlation between ischemic duration and hematocrit value. The Spearman correlation coefficient is a nonparametric analog to the Pearson correlation coefficient. Because it does not assume a Gaussian distribution of the underlying data, it is more appropriate for small sample sizes as used in this study.

The objective of this study was to develop a method for noninvasive hematocrit measurement for use in rat ischemia experiments. Basing the experimental procedures upon work performed in humans, small animal imaging techniques were applied to obtain similar information. Radiochemistry, imaging physics, image analysis and statistical analysis were brought together to evaluate the hypothesis and complete the study. This project provided an excellent example of the sophistication of modern small animal imaging studies.

Chapter 4

Results

A successful imaging experiment requires the integration of physics, chemistry, biology and programming. Advances in each field allow for continuous improvement and more advanced studies. Each study described will emphasize different components. Sections 4.1 and 4.2 focus upon improving the imaging physics for a single pinhole collimator. Section 4.3 tests a new tracer, which is an exercise in chemistry and biology. The results shown in Section 4.4 require the fusion of all the disciplines to answer a physiological question.

4.1 Dual Circular Orbit

To correct for the incomplete axial sampling of the pinhole collimator, the effect of two circular orbits placed at different axial distances was tested. Both simulations and experiments were performed to validate and characterize the dual orbit approach. Simulation data was used to demonstrate the theoretical potential of the method and prove that the projections could be reconstructed using ideal data.

4.1.1 Dual Circular Orbit Simulations

Simulations were performed using geometrical ray software to reproduce the geometrical components of the projections. Scatter and attenuation were ignored for this study. The first simulation provided a baseline image using a standard circular orbit

centered on the object. Sample projections and reconstruction slices are shown in Figure 4.1.

The images in Figure 4.1 clearly illustrate the problem with axial blurring inherent with pinhole imaging. When the magnification is low, the object fits easily within the center of the FOV and as such does not rely on wide-angle rays to view and sample the object. Because of the relatively short axial component, the object is reconstructed fairly well. When the object is moved closer to the pinhole and magnification is increased to M=2, the projections show a far more severe pattern of axial distortion. The angles of the rays sampling the upper and lower extremes of the phantom are far larger with this geometry resulting in increased distortion. This distortion in the projections results in large artifacts in the reconstruction that can be seen in the upper and lowermost bands of the phantom.

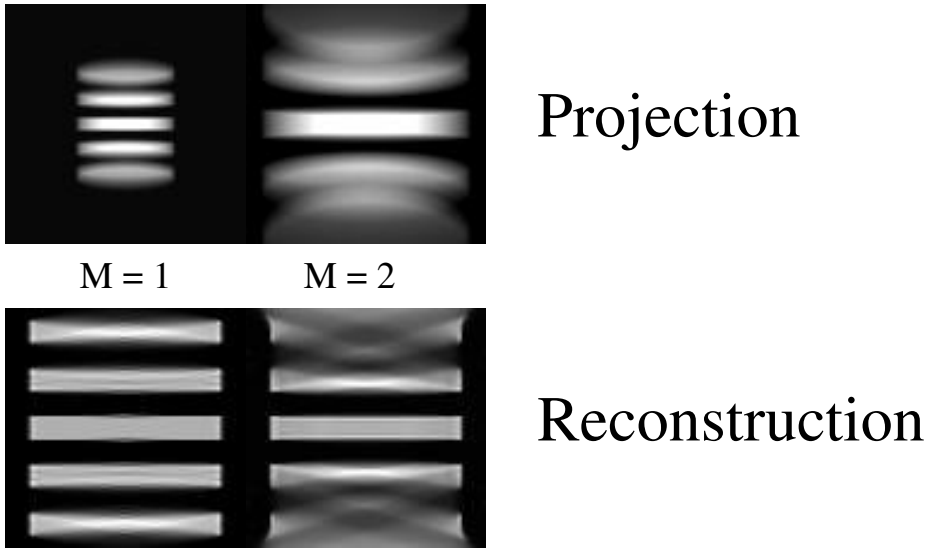

Figure 4.1: Illustration of pinhole artifacts due to poor axial sampling. As the object is moved closer to the pinhole, magnification (M) is increased and the incident angles of the rays sampling the upper and lower most hot bands of the object are larger. The larger incident angles result in inadequate sampling and distortion in the projections. The poor projections cause artifacts in the reconstructed image.

The first simulations using the dual-plane orbit were performed with the orbits placed so the object was divided evenly between the two fields of view. This was accomplished by dividing the object into fourths, and one orbit plane was moved up ¼ of the object length, or 1.25cm, and the other orbit plane was moved down 1.25cm of the object length. Dividing the object in this manner should take advantage of minimizing the most extreme distortions as the FOV used in each projection set has been reduced by a factor of 2.

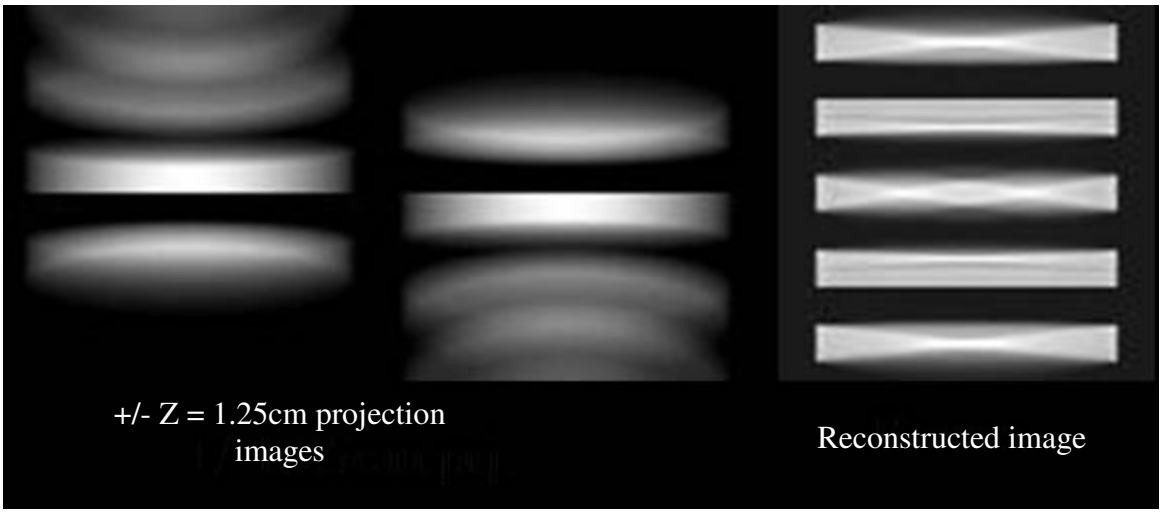

Figure 4.2: Sample projections and resultant reconstruction using the dual-circular plane pinhole orbit. Each orbit was shifted +/- 1.25 cm from the centerline of the FOV. Geometrically, this pitch divides the object evenly between the two orbits, as the FOV was 5cm.

Comparing the images shown below in Figure 4.2 with the images from Figure 4.1 suggest that even a simple dual-plane arrangement where the image space is divided evenly drastically improves reconstructed image quality. From the reconstruction, all 5 bands are clearly defined and undistorted. Even though each projection set only samples a portion of the object, by using OSEM we can incorporate both projection sets into the image estimate and obtain an improved reconstruction.

In order to more quantitatively examine the effect of the two projection sets on reconstruction, profiles along the axial direction in the center of the object were taken and compared to profiles of the original phantom and the reconstructed image using only a single projection set. The difference between the original phantom and the reconstructed images could be expressed in terms of standard error using the respective profiles. Figure 4.3 shows the profiles of the original phantom along with the dual and single plane reconstruction profiles. The positions of the orbit planes are depicted as vertical lines at the appropriate pixel number. Clearly, the dual-orbit reconstruction more accurately depicts the bands at the edges of the object. However, the dual-plane reconstruction does not show the correct uniformity within the hot bands, although this is also a problem with

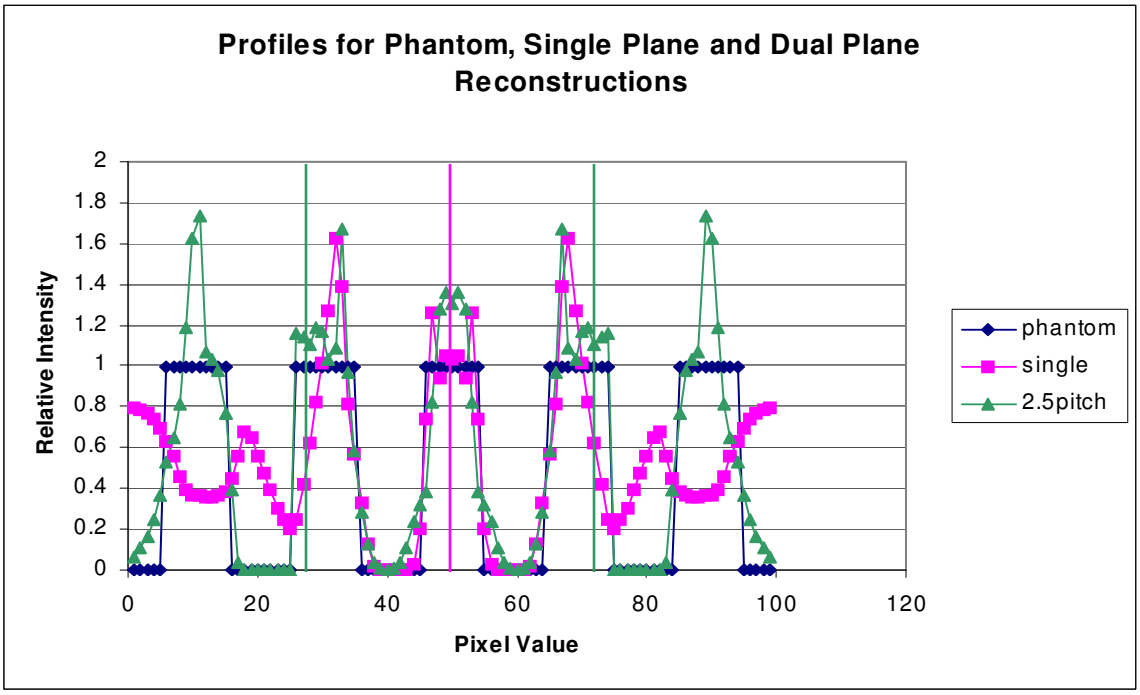

Figure 4.3: Vertical profiles through the phantom, single-plane and dual-plane images show clear differences in reconstruction accuracy. Vertical lines denote orbit plane location. The single-plane orbit most accurately reproduces the central slice, while the dual-plane orbit is superior for the outer bands. All orbits suffer from cone-beam artifact seen as sharp peaks within the hot regions of the object. Comparing the profiles at the troughs provides a more useful measure for how accurately the phantom is reconstructed, as these artifacts do not influence the images as strongly in

the single-plane reconstruction. Another shared problem with both the dual-plane and single-plane reconstructions is the presence of a hot band in the 2nd and 4th hot planes which is representative of the cone beam artifact inherent to pinhole imaging.

The dual-plane approach does tend to reproduce the outer bands in a more accurate manner than the single-plane approach. The single-plane reconstruction results in some axial blurring reducing resolution and causing very poor image quality at the edges of the field-of-view. When examining the profiles in the cold regions of the image we see that for the empty space near the central band, the single-plane profile reproduces the sharp edges and faithfully represents the blank space as zero intensity. Looking at the same cold regions with the dual-plane profile, we notice that the edges are not as sharp or defined, and the trough is a bit more rounded. Conversely at the cold regions near the edge of the FOV the dual-plane profile performs far better than the single-plane profile.

In order to both qualitatively and quantitatively examine the effect of orbit translation distance on reconstruction, several acquisition geometries were simulated using the same Defrise phantom as before. A range of vertical translation distances, or pitches, were chosen to simulate a broad variety of geometries and induce a wide range of artifacts. The simulated pitches range from 6.25mm to 5.0cm. Smaller pitches such as 6.25mm are expected to result in insufficient sampling at the outer extremes of the object and not completely overcome the axial blurring. Larger pitches are expected to show the opposite problem and not properly sample the center of the object resulting in blurring, distortion and loss of resolution. Figure 4.4 shows the central coronal slices of the reconstructed images for each of the acquisition geometries.

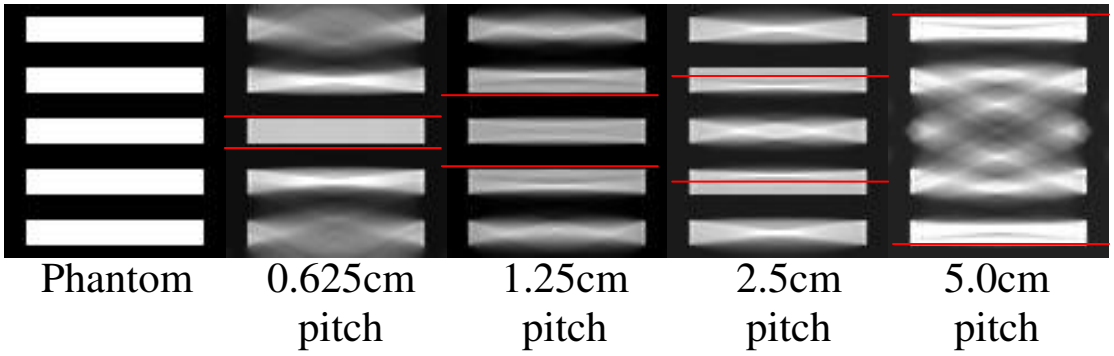

Figure 4.4: Sample reconstruction slices from the varying pinhole geometries allow for comparison of the effect of orbit spacing, or pitch, on reconstruction quality. The geometry such that the orbit planes divide the object evenly provides the greatest reconstruction quality, but it seems that an acceptable range of pitches exists.

Upon visual inspection, the best reconstruction seems to be the 2.5cm pitch image. The image using a pitch of 1.25cm also produces a fair reconstruction and accurately defines the hot planes of the phantom, although slight blurring at the extreme planes is apparent. As expected, when the pitch between the two orbit-planes increases, the accuracy of the central slice becomes worse. Profiles of the images clearly show these artifacts and are found in Figure 4.5. The images show that poor acquisition geometry and orbit positioning can result in image quality as low as or even lower than a standard single orbit scan so care must be taken to properly place the orbit planes. The data supports the hypothesis that dual circular orbit scans can improve pinhole image quality, but consideration of the appropriate imaging geometry and tradeoffs between image quality and scanning time is required.

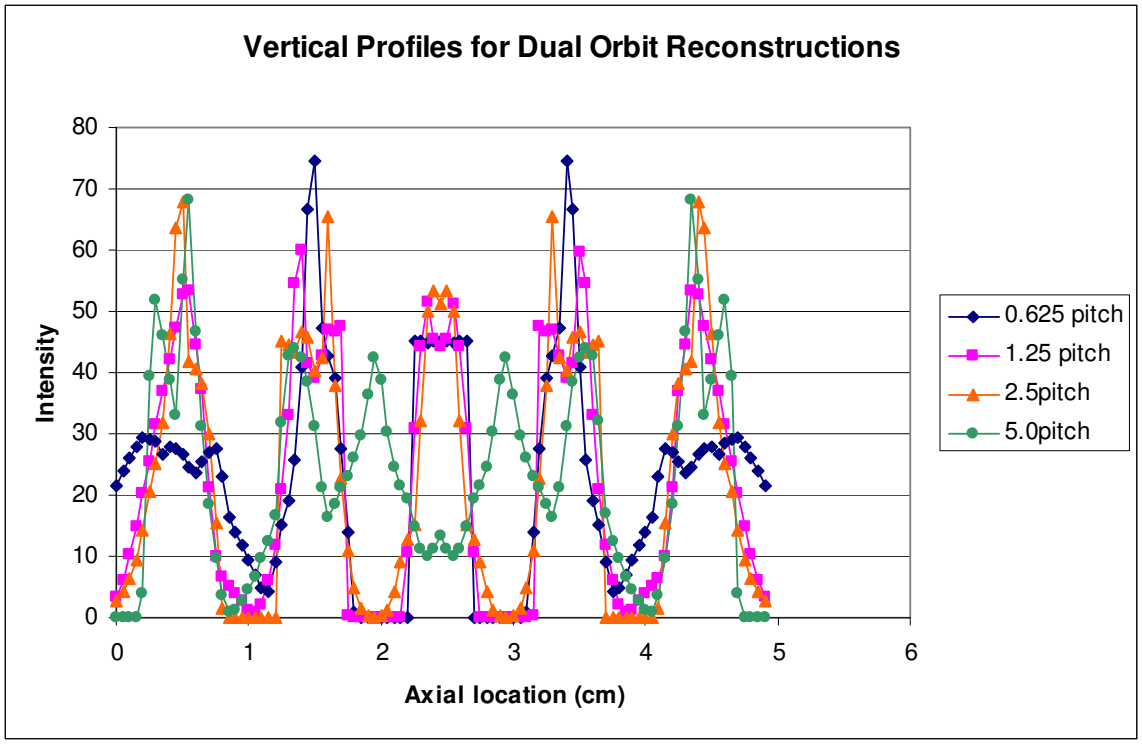

Figure 4.5: Profiles for the Figure 4.4 images show the effect of pitch on image artifact. The 5.0cm pitch profile clearly shows aliasing artifact in the 40 and 60 pixel range. The 0.625cm pitch performs poorly at the outer range of the FOV, and the 1.25cm and 2.5cm pitch profiles perform similarly. Optimization of orbit location depends upon the object distribution as well as camera FOV.

Looking at the standard error of the individual reconstructions within ROIs defined for the center, intermediate and outer cold bands allows us to better quantify the accuracy of the reconstruction and the effect of geometry on that accuracy. Examining the images in the cold regions avoids problems arising from the cone-beam artifacts, which appear as bright streaks within the hot bands. Figure 4.6 shows a plot of the mean error within 6 ROIs for each of the reconstruction geometries. Each ROI corresponds to a different cold region of the phantom. Measuring differences between reconstructed images and phantom images at the cold regions allows for the sharpness, or contrast gradient between the hot and cold bands to be examined more closely without adverse effects from the cone-beam artifacts. As the aliasing artifacts tend to manifest as blurry

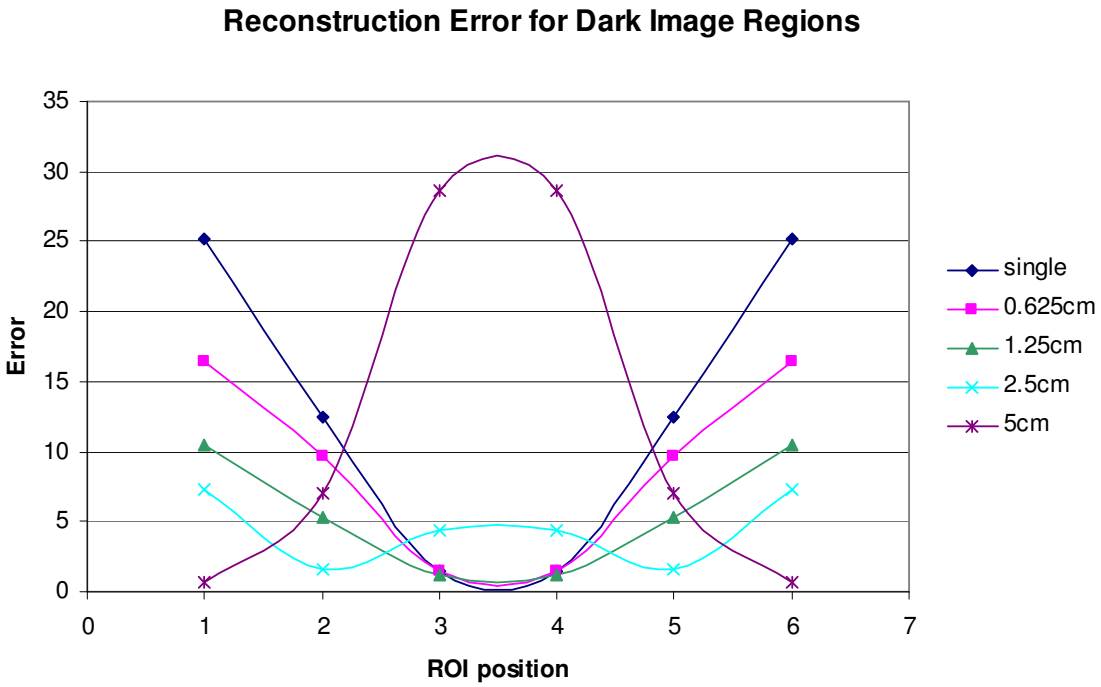

Figure 4.6: Reconstruction errors within each cold ROI differ based on the pitch of the two orbits used during acquisition. We can see that the most uniform error distribution occurs with the 2.5cm pitch.

edges, looking at the cold regions also allows a sense of the spread into neighboring pixels to be obtained by how sharply the edges are defined.

From this examination of the error it is difficult to choose a geometry that is 'optimal' as no single geometry performs best for all regions. It would appear that the 2.5cm pitch performs on average better than the other pitches, and that the 0.625cm pitch performs the worst, but the optimal arrangement will likely depend somewhat upon the object distribution and where the key features lie in the FOV. From the images seen in Figure 4.4, and the error plots shown in Figure 4.6, we can conclude that the most useful geometry would divide the FOV equally such as the 2.5cm pitch in the simulations, but the data suggests a range of potentially acceptable configurations

depending on where the activity is distributed in the object. It is also clear that increasing the pitch too much results in extreme image artifact and corresponding loss of resolution and clarity. The Defrise phantom used in these simulations is designed to be the most difficult phantom to image with a pinhole due to the sharply defined planes. Any offset of the pinhole orbit plane from a hot plane introduces error that is more clearly witnessed with this phantom than with a more realistic phantom. Moving the location of the orbit planes introduces a tradeoff between accurately reconstructing the outer bands, the intermediate bands, or the central band, but not all three. Proper reconstruction of all bands requires an orbit that offers complete sampling of all data such as a helix or spiral. As the intent of this work is not to compete with a helical orbit in terms of overall image accuracy, but to offer a simpler solution that maintains some practical utility, the question should be: does this method improve image quality with respect to a single orbit? The simulations suggest that it does. We will now look at some experimental images using the dual-orbit approach to see if they support the simulations.

4.1.2 Dual-circular Orbit Experimental Results

A microDefrise phantom purchased from Data Spectrum was used for the dual-plane orbit experiments. This phantom's height is 5cm and consists of a set of 5mm thick acrylic discs separated by 5mm spacers. When the phantom is filled with ^{99m}Tc solution, the effect is cold regions where the disks are alternating with hot disks where the spacers are. The phantom was placed at a distance from the pinhole that would not allow truncation in the transaxial direction and at a height that centered the phantom within the pinhole FOV. The phantom was placed on a computer-controlled XYZ table with the ability to place the phantom in 3-D space at 100μm accuracy. Because proper

reconstruction requires precise knowledge of the linear translation of the orbit planes as well as the typical pinhole geometrical parameters, the computer-controlled stage is critical.

With the phantom centered within the pinhole FOV, the first scan used a typical single circular orbit, which was achieved by simply rotating the phantom about the axis of rotation on a motorized stage. Sample projections and the resultant reconstruction are shown in Figure 4.7.

The images in Figure 4.7 confirm the issues seen in the simulated images. When the magnification is increased to use more of the detector FOV, we see increased sampling problems in the projections. At 5.5cm, only the central band is clearly defined in the projection images, while the other bands are blurred together. The reconstruction

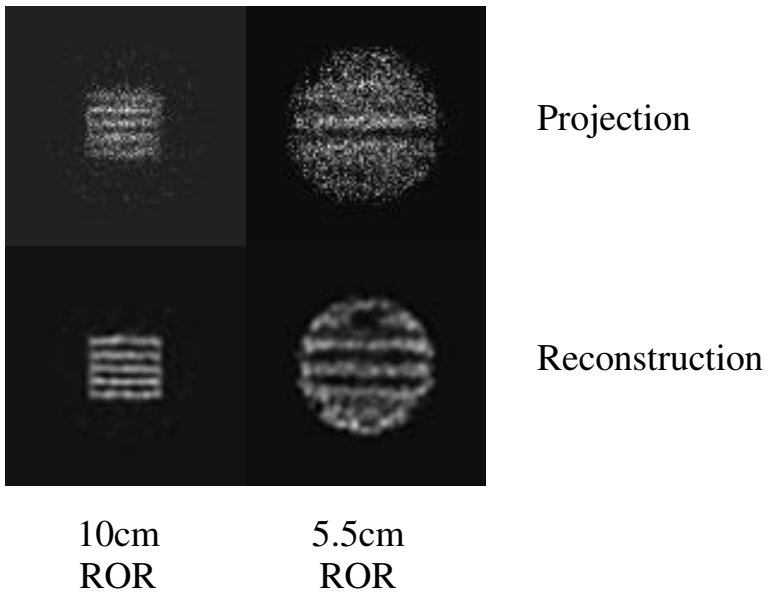

Figure 4.7: Images acquired with the MicroSPECT system at UNC. The Defrise phantom used is approximately 5cm tall and 5cm in diameter with 5 hot bands separated by plastic septa. When the object is scanned at 10cm (M=1), the reconstruction does not show any artifact, however when imaged at 5.5cm (M = 1.8), we can see that the uppermost and lowermost hot bands are not clear. Also because the detector is circular instead of square, we see some truncation of the object in both the projection and reconstruction.

can sort out the two intermediate planes, but the outermost planes are poorly defined. Another issue with the experimental data is the truncation induced by the circular FOV of the detector.

When the detector is square, the sampled volume maintains a cylindrical shape, but when the detector is circular, pixels further away from the axis of rotation and the central transaxial plane of the pinhole are not sampled at the same rate as those near the center. This results in an oblong shape for the completely sampled volume with partially sampled pixels making up the remainder of the cylinder. When performing dual-plane studies with a circular detector, this problem must be taken into consideration because of artifacts that can arise. The interaction between the two oblong sampled volumes can result in artifacts in the reconstructed image. Figure 4.8 shows reconstructions for the 2.5cm pitch and 1.25cm pitch geometries acquired using the MicroSPECT system.

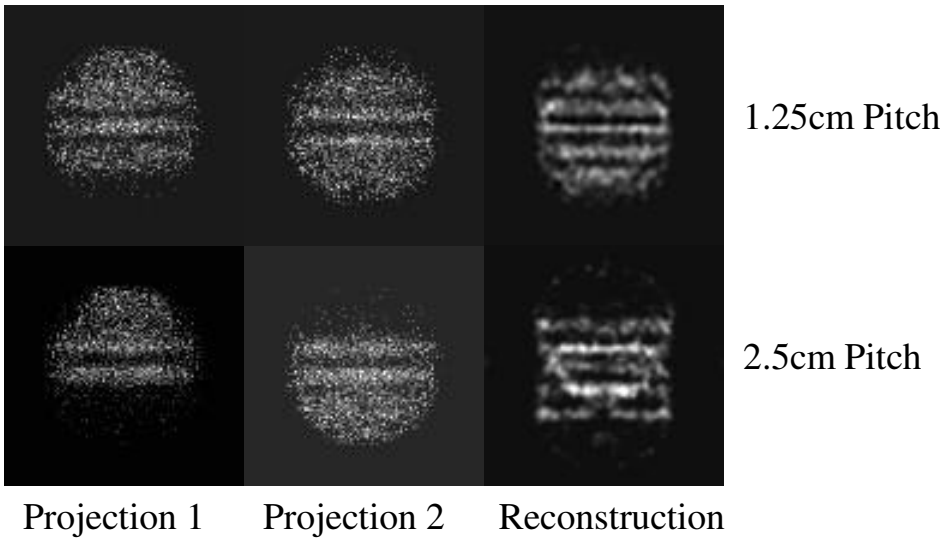

Figure 4.8: Sample images from both projection sets along with reconstructed images are shown for experimental data from the MicroSPECT system. The images from the 2.5cm pitch show a severe artifact in the center of the image due to differences in sampling caused from the circular FOV. The artifact is present in the 1.25cm pitch image, but not as severe. This would indicate that for circular cameras, the optimal pitch is less than the pitch that can be used for square cameras.

Artifacts from the circular FOV are apparent in both reconstructions shown in Figure 4.8, but they appear much worse in the image acquired with the 2.5cm pitch. The artifact seen in Figure 4.8 is due to changes in the sampling rate between pixels within the overlapping volume and pixels outside of it. Minimizing the artifact due to the circular FOV requires maximizing the overlap between the two sampled volumes and shortening the pitch. We have seen from the simulations in Figures 4.4-4.6 that an optimal pitch exists to minimize the axial sampling effects. These two counteracting problems force a tradeoff between improving the axial effects and reducing the artifact due to circular FOV.

Because of the circular FOV artifact, the optimal geometry determined from the earlier simulations is no longer accurate. We must also include the FOV affects in our simulations if we are to determine a realistic solution to the question of acquisition geometry. With these new questions, we require additional simulations and experiments to properly find the answers. The next section will show the results from dual-plane simulations using a circular detector.

4.1.3 Dual-Plane orbit with circular detector simulations

Because the experimental results showed unexpected artifacts due to changing noise levels within the reconstructed image, simulations were performed using circular FOV detectors to attempt to validate the method. The circular FOV was created by multiplying the square projections with a circular mask. Poisson noise was added to the circular projections to simulate experimental noise levels. The noise was scaled for 25K counts/projection. Sample projection images are shown in Figure 4.9.

By varying the pitch between the two circular orbits, the effect of the circular FOV upon the reconstructed image, and the relationship between pitch size and data completeness was analyzed. The pitch length was simulated for lengths varying from 6.25mm to 50mm, The circular FOV results in differing sampling completeness at different axial positions as the width of the FOV decreases toward the edges. For voxels that lie off center axially and transaxially, they will be included within some projection views, but will fall outside of the FOV in others. The result is an incomplete set of views for voxels that lie toward the 'corners' of the image. Increasing the overlap between the two circular fields of view helps to alleviate this effect, but that reduces the pitch length and worsens coverage toward the axial extremes. The circular FOV introduces a more

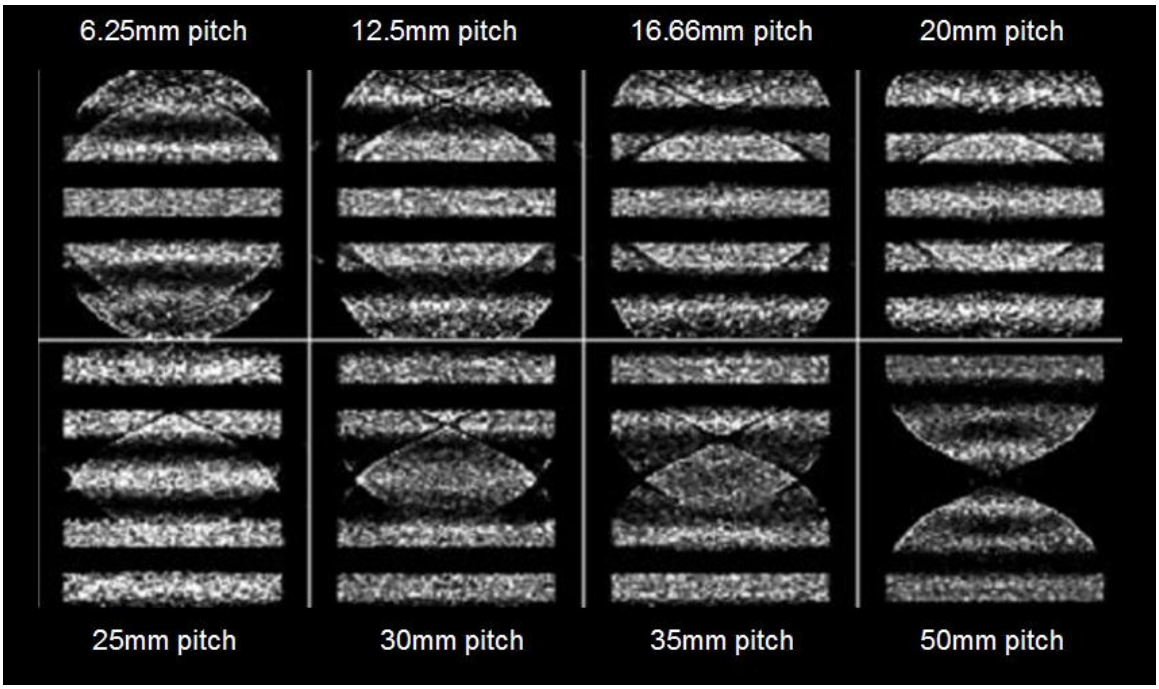

Figure 4.9: Comparison of coronal reconstructed slices using dual-plane tomography for simulated circular FOV detector and noise simulated for 70K cts/prj. Object height is 5cm, detector FOV is 10cm and M = 2. The optimum pitch appears to be 25mm based on overall image quality.

severe tradeoff between axial sampling, and transaxial sampling than the square FOV case. Figure 4.9 shows sample coronal slices from reconstructions using the various pitch lengths.

The noisy, circular projections simulate the artifact seen in the experimental images quite well. Based on overall image quality, the optimum pitch is 25mm. That image suffers the least noise artifact and has the best overall accuracy in the disc shape. Shorter pitches tend to compromise accuracy at the edge of the object, and longer pitch compromise in the center. Also, the noise artifact for the shorter pitches tends to be more pronounced, although this could be a function of the distribution of the object and the alternating hot bands tend to exaggerate the effect. Unfortunately, even the optimum geometry suffers from some artifact, so it would be helpful to develop a correction to reduce this effect.

A solid phantom of identical shape and size to the disc phantom was simulated without noise using the same dual-plane parameters as the 20mm pitch case. The reconstruction of this solid phantom should display the entire noise pattern resulting from the dual-plane acquisition. By defining the noise pattern for a specific geometry it may be possible to develop a normalization image that can be applied to other acquisitions using that same geometry. The projections and reconstruction of the solid phantom are

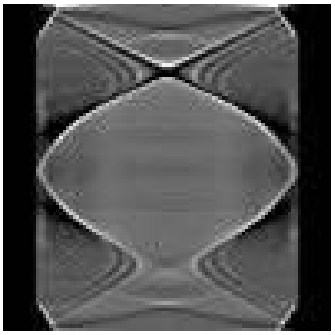

Figure 4.10: Reconstructed coronal slice of solid cylinder phantom acquired with 20mm pitch dual-plane orbit using circular FOV detectors. Variations in sampling rate result in intricate image artifacts where the fields of view overlap. Additionally, dark fields surrounding the large overlap artifact signify low sensitivity, likely due to pixels outside of either FOV.

shown in Figure 4.10. The variability in sampling completeness throughout the two fields of view result in very obvious image artifacts, especially where the two fields of view overlap. The most dominant feature in the image is the oval artifact near the center of the image that appears to correlate well with the artifacts seen in Figure 4.9. It should be noted that the image in Figure 4.10 was taken from noise free projections, so it is unlikely that the intricate pattern of artifacts would ever be realized from experimental data. Nevertheless, computation of a normalization image from the image in Figure 4.10 with pixel values that vary from 0 to 1 could be applied to the 20mm pitch image in Figure 4.9 to reduce the effect of the overlap artifact. Figure 4.11 shows the original image from Figure 4.9 using the 20mm pitch between axes of rotation, along with the normalization image and the final corrected image.

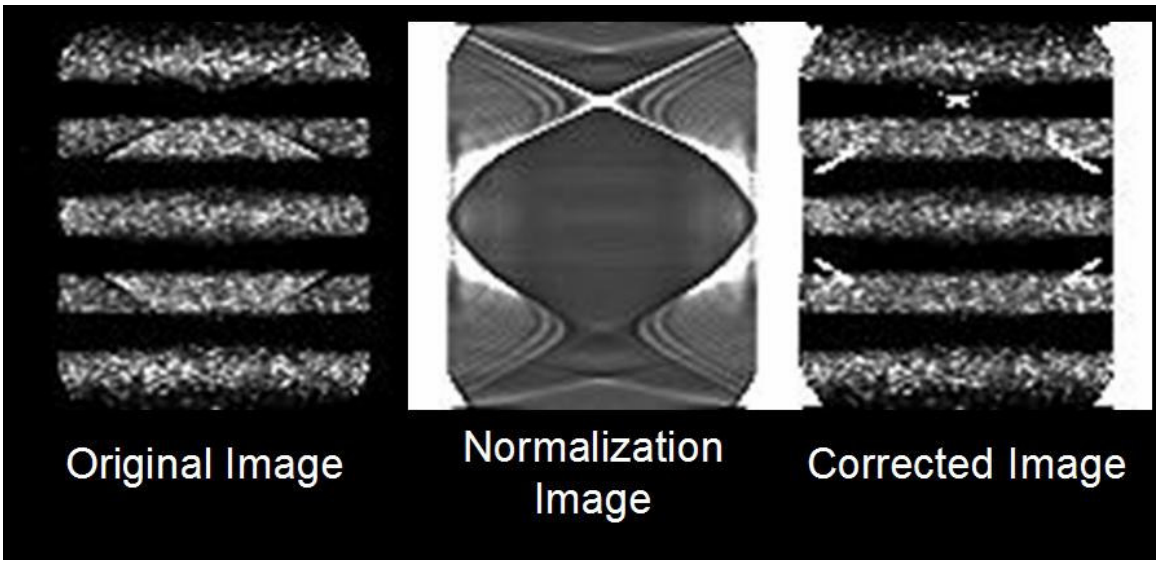

Figure 4.11: Multiplying the original image by the normalization image computed from the cylinder image reduces the extent of the artifact and enhances contrast in the center of the corrected image. The sharp lines have been reduced, but some lingering effects remain. The center appears colder than the rest of the image, which may suggest that a simple correction is not sufficient, and some tuning of the normalization image is required.

The normalization image was created by inverting the original cylinder image and normalizing the inverse image by the maximum pixel value to create an image that varies from 0 to 1. The bright nonuniformity seen in the original image has been corrected, but four sharp line artifacts remain near the transition region between overlapping and non-overlapping coverage. These artifacts were created by the normalization image which has sharp transitions and large intensity gradients between the overlap regions. Applying a median filter to blur the transition regions within the normalization image helps to reduce the severity of the artifact. The corrected image along with the blurred normalization image is shown in Figure 4.12.

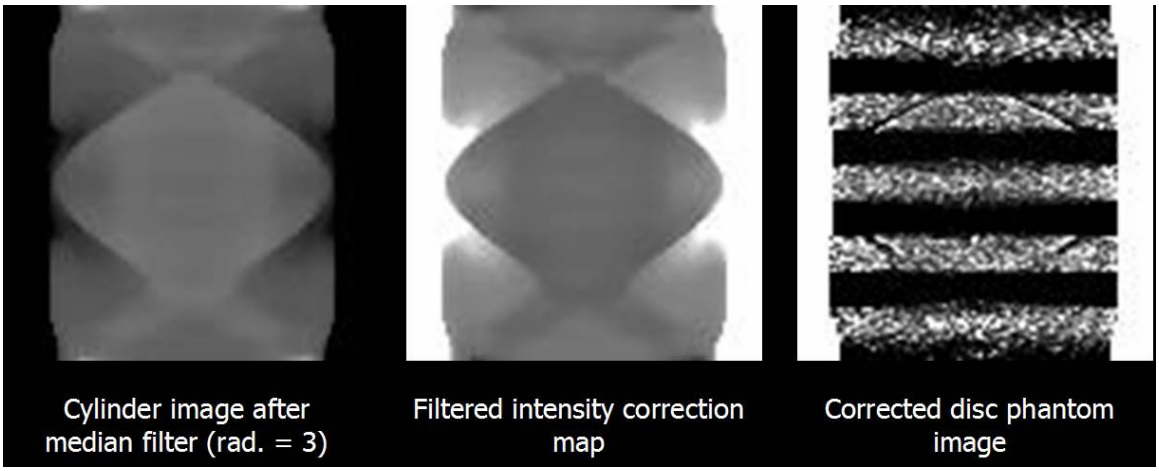

Figure 4.12: Filtering the original cylinder image with a median filter reduces the sharp gradients and allows the normalization image to correct for differences in regional intensity without amplifying the transition regions. A slight artifact persists, but could easily be removed with use of a butterworth filter.

4.2 Dual Axis of Rotation Orbit for Truncation Correction

The purpose of this project was to establish a method that could maximize the magnification used with a pinhole while maintaining a useful FOV. Generally, when using a pinhole collimator, the object is placed as close as possible to the aperture without introducing transaxial truncation in the projections. This requires the object to be placed

at least 3-4cm from the aperture, with objects of larger diameter requiring larger radii of rotation. By using multiple orbits centered about multiple axes of rotation, the truncation introduced from short ROR lengths can be compensated for allowing the entire object to be reconstructed accurately. Our method follows a similar logic to that used by Kadrmas (Kadrmas, Jaszczak et al. 1995), but we intend to use the OSEM algorithm instead of performing various interpolations and using FBP.

4.2.1 Dual AOR Simulation Experiments

Micro SPECT phantoms were simulated for both single-orbit and dual-orbit scans. The phantom was simulated to be 10cm in diameter on a 128x128x128 matrix. The detector was modeled to have a 10cm FOV over a 128x128 array. The focal length for the pinhole was 10cm. For the single-orbit scan, the phantom was placed at a distance of 10cm from the pinhole aperture to ensure no truncation in any projections, and the AOR was placed orthogonal to the central ray of the pinhole collimator. For the dual-orbit scans, the phantom was placed a distance of 5cm from the collimator, but the two axes of rotation were shifted symmetrically about the central ray parallel to the projection plane.

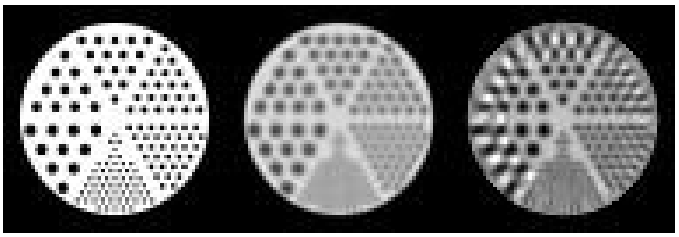

Phantom Standard Reconstruction Truncated Reconstruction

Figure 4.13: Image of original phantom along with reconstruction image using a single set of untruncated projections, and a reconstruction using truncated projections. Truncated projections were simulated from shortening the distance from the object to the pinhole.

Figure 4.13 shows the original phantom along with a standard reconstruction and a reconstruction using truncated projections. The untruncated reconstruction shows that all rods except the smallest can be clearly identified and the image is smooth and artifact-free. The truncated reconstruction shows the result when the object distance was halved leaving all other geometrical parameters constant. The truncation in the projections introduces an artifact in the reconstruction that results in distortion toward the outer regions of the image.

Figure 4.14 shows sample slices from reconstructions using the dual AOR approach with varying shifts between the axes. The most accurate images are produced when the AOR shift divides the object into two equal sections, with each projection set sampling exactly half of the object. For smaller AOR shifts, artifacts are produced at the outer edges of the phantom suggesting incomplete sampling for the outermost regions. For larger AOR shifts, artifacts are seen in the center of the phantom. The images in Figure 4.13 suggest that proper placement of the two axes of rotation is critical to reconstruction quality, and is dependent upon the FOV and magnification used.

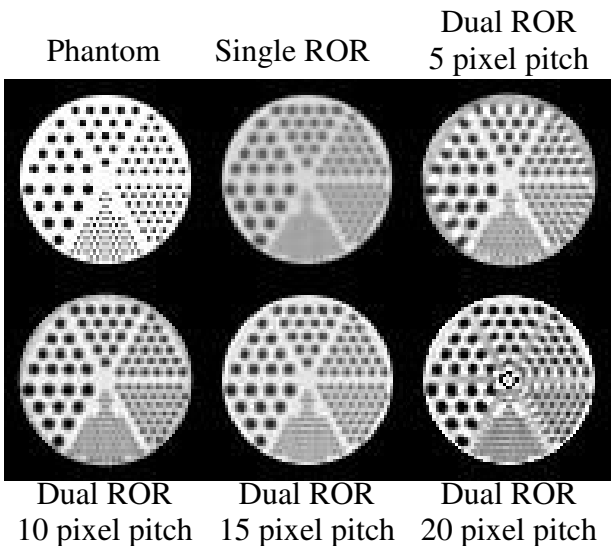

Figure 4.14 Simulated phantom image along with reconstructed slices from various two-orbit scans. The distance between the axes of rotation were varied from 5 to 20 pixels.

Using the dual-orbit approach may change the typical tradeoffs between resolution and sensitivity. Because two projection sets are used to acquire the data, the resolution of the images now depend upon the geometrical arrangement and pitch of the orbits in addition to the pinhole size and magnification.

4.2.2 Dual-AOR Experimental Results

A micro-deluxe hot-rod phantom (Data Spectrum, Hillsborough, NC) was used for the experimental validation of the dual-AOR orbit. A baseline scan was performed to establish the resolution and image quality using typical object length settings to prevent truncation. The object length for this scan was 7cm, resulting in a magnification level of 1.43 and the pinhole aperture diameter was 0.75mm. The phantom was filled with ~6mCi of ^{99m}Tc and 60 projections were acquired over 360^0. Scan time was 20 minutes and each projection acquired approximately 15K counts. The projections were

reconstructed using OSEM with 5 iterations and 6 subsets. A post-reconstruction 8th order Butterworth filter having a 0.3 cycle/pix cutoff frequency was applied to reduce the noise level in the image. The largest four rod sizes, 4.8, 4.0, 3.2, and 2.5mm are clearly distinguishable, while the 1.6mm rod size is barely distinguishable, although the rods did not fill completely. The phantom channels for the 1.2mm and 1.6mm rod sizes were partially occluded and did not fill properly so evaluations of those sectors are not possible. The insert diameter is a few mm shorter than the inner diameter of the phantom housing which results in a band of activity surrounding the insert.

For the first dual-AOR experiment, the object length was kept at 7cm to allow for evaluation of the dual-AOR procedure without any truncation defects present. It was important to establish the techniques and calibration methods to obtain good images without any truncation defect interfering. Projections were reconstructed using OSEM, again with 5 iterations and 6 subsets. Sample projection and reconstructed images are shown in Figure 4.15.

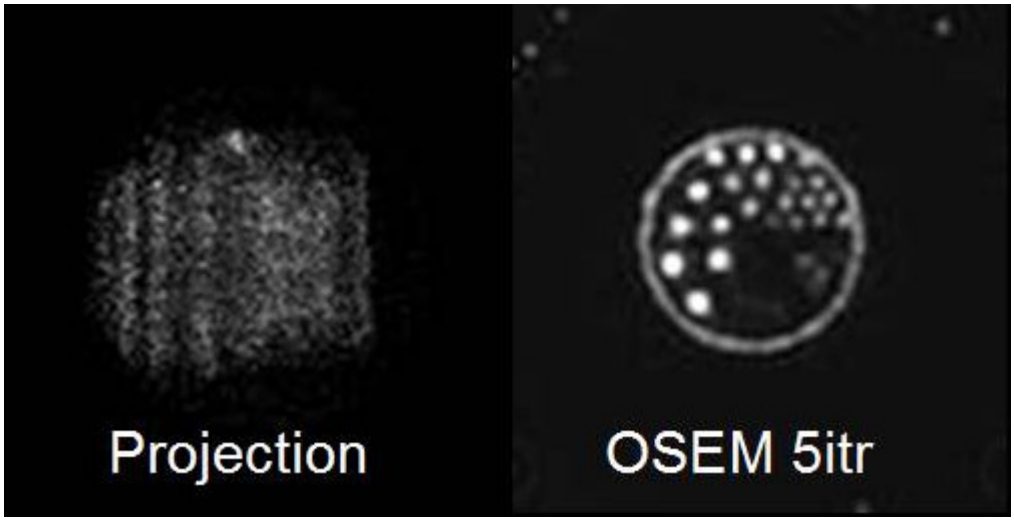

Figure 4.15: Sample Projection image and transaxial slice for microSPECT phantom filled with 5mCi ^{99m}Tc. Object length was 7cm to avoid truncation of the 5cm object.

The next experiment analyzed the effects of truncation for a dual-orbit acquisition with minimal truncation to verify the ability of the algorithm to properly reconstruct data without severe data insufficiencies. For this scan the phantom kept at 7cm from the aperture. Sample projections and the resulting reconstruction are seen in Figure 4.16.

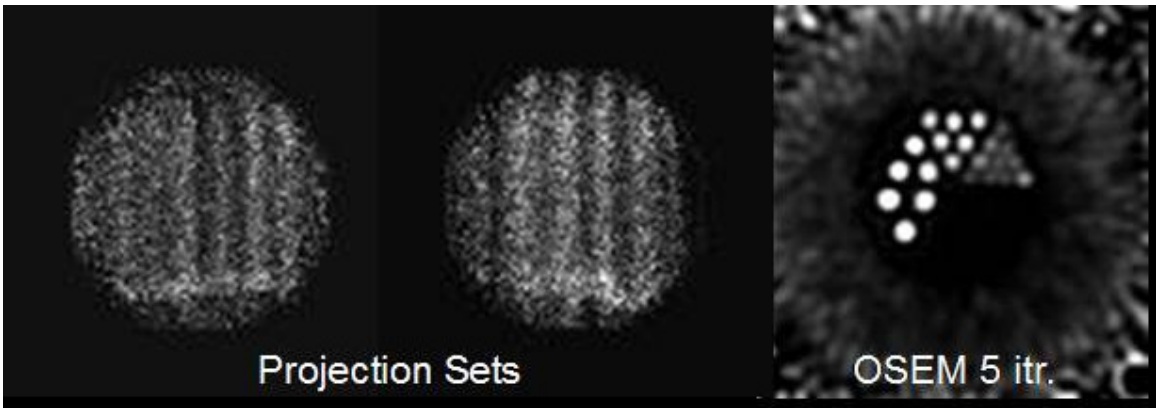

Figure 4.16: Two sets of projections were acquired with the axis of rotation shifted +/- 6mm with respect to the pinhole aperture. OSEM reconstruction was used to simultaneously reconstruct the two data sets. Obvious reconstruction artifacts are evident due to parts of the object not being included in every subset.

The reconstructed image in Figure 4.16 does not faithfully reproduce the tracer distribution within the phantom. The outermost band of activity is not reconstructed, and a wide ring artifact surrounds the hot rods of the phantom. Although both projection sets provide the complete set of views required for reconstruction, the OSEM algorithm separates the views into smaller subsets for updating the algorithm. For the algorithm to work properly, the same portion of the object should be visible from each view within the subset. By taking a closer look at the normalization images created during the reconstruction process, we can understand the field-of-view covered within each subset. The normalization images are created based on the geometrical parameters of the scan and define the fields of view for each projection. They are used to properly weight the reconstructed image based on the relative sensitivity of the pinhole trajectory to different

voxels. Under normal imaging conditions with the object and axis of rotation centered with respect to the pinhole, the natural symmetry of the circular orbit allows the projections to be broken into subsets easily. The dual-AOR orbit, however, creates conditions where portions of the object move in and out of the FOV so each view within a subset may not include the same voxels. This problem can be alleviated by using the maximum-likelihood-expectation-maximization algorithm which performs iterations upon the entire projection set at once. The normalization images for the OSEM and MLEM algorithms are seen in Figure 4.17.

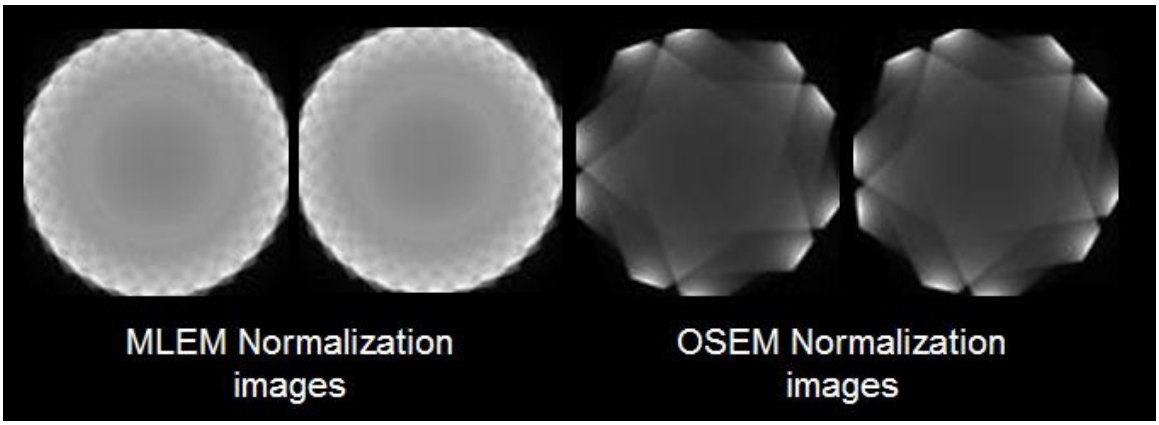

Figure 4.17: Sample normalization images for the MLEM and OSEM reconstruction algorithms. The MLEM normalization includes all 60 projections for each orbit, while the OSEM normalization only includes a single subset of 10 projections, 5 from each acquisition. Only two subsets are shown as examples. The OSEM normalization images show the overlapping cone-shaped FOVs for the two orbits.

A sample reconstructed image using the MLEM algorithm is presented in Figure 4.18 along with the sample reconstructed image using the OSEM algorithm. The MLEM algorithm outperforms the OSEM algorithm in this example due to its more inclusive manner in the handling of projection data. The tradeoff is increased computational time as the MLEM algorithm requires far more iterations than does OSEM. For the images

shown in Figure 4.18, the MLEM image required 60 iterations while the OSEM algorithm took only 5. Both images were filtered with 8th order Butterworth filters using 0.21cycle/pixel cutoff frequencies. The MLEM image closely matches the distribution seen with the single orbit scan without any serious artifacts. The 2.5mm rods are again clearly resolved indicating little resolution loss performing the dual-AOR scan. Because of the increased number of geometrical parameters when using the dual-AOR orbit, the potential exists for mismatch artifacts due to incorrect measurement of focal length, object distance, and position of the axes of rotation with respect to the detector. Careful calibration can help to alleviate these issues. For this study a line source was scanned using the same AOR positions as the phantom and reconstructed using the dual-AOR method. The geometrical parameters were adjusted to minimize the reconstructed diameter of the line indicating the correct values.

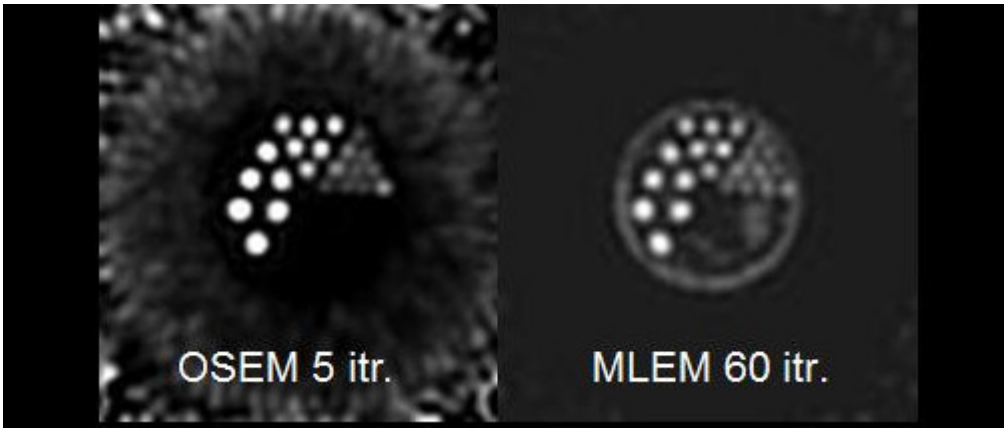

Figure 4.18: Comparison of OSEM algorithm with MLEM algorithm for 6cm object length. The OSEM image results in artifacts resulting from incomplete views within the subsets. Because the MLEM algorithm uses all projections during the update process, the holes in the data do not carry the same weight and can be compensated for. MLEM requires far more iterations and is much slower, however.

After validating the ability to perform the dual-AOR procedure without significant loss of resolution or introduction of artifact for a conservative geometry, the ability of the method to enhance the magnification levels and improve resolution was tested. Again, a baseline image was acquired using a single orbit scan, but the object was placed a distance of 5cm from the aperture instead of 7cm. This reduced the FOV and introduced truncation into the projection images. The projections were reconstructed using the same OSEM parameters as before. The projection and reconstruction images are shown in Figure 4.19.

The truncated projection set does not provide complete views for all object voxels. This results in a distortion at the edge of the field-of-view. Overall, the image appears normal, and in fact the 2.5mm rods are better resolved than when the object was imaged at 7cm, but the distribution at the edges is incorrect, most obviously due to the missing band of activity around the phantom. The rods at the extreme edge are also slightly distorted and more intense than the center of the object. Large artifacts can also

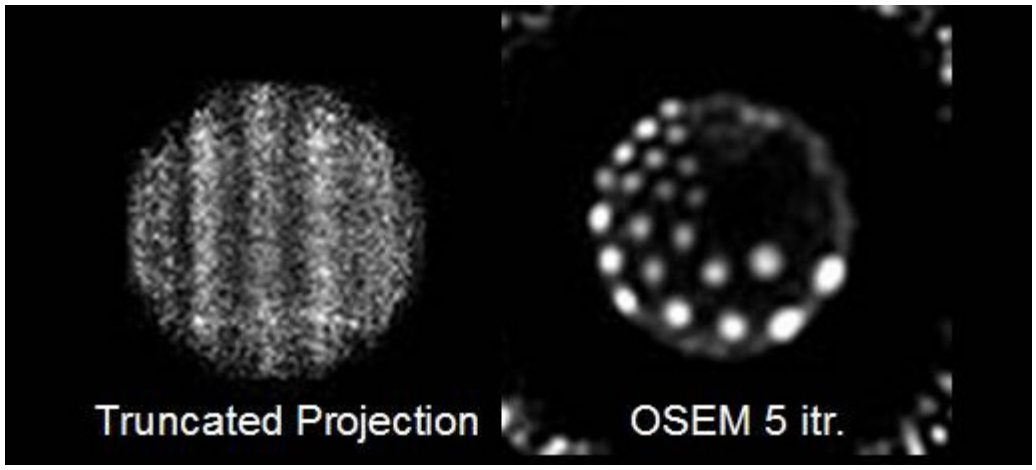

Figure 4.19: SPECT phantom imaged at 4.5cm object length. The small FOV results in truncated projections seen at left. Resulting reconstruction shows evidence of pincushion distortion and the outer edge of the object is incorrectly represented. Distortions are the result of incomplete views for pixels at the edge of the object.

be seen at the far edge of the reconstructed image.

After establishing the baseline resolution with a standard single-orbit scan and with a truncated single-orbit scan, the dual-AOR method was applied. The object length remained at 5cm, but the axis of rotation and object center were shifted by +/- 6mm. This shift was measured to be the minimum distance that allows the edge of the phantom to enter the FOV. The time spent imaging was kept at 20 min total with 10 min allowed for each orbit. The resulting reconstructions are shown in Figure 4.20.

The images seen in Figure 4.20 summarize the results of the dual-AOR experiments. At left is the image seen in Figure 4.13 using a single orbit and an object distance of 7cm to prevent truncation. The center image was shown in Figure 4.17 was generated using a single orbit, but 5cm object length to induce truncation in the projection images. At right, the result of the full dual-AOR procedure is shown. Clearly, the two images using the shorter object length exhibit more magnification resulting in

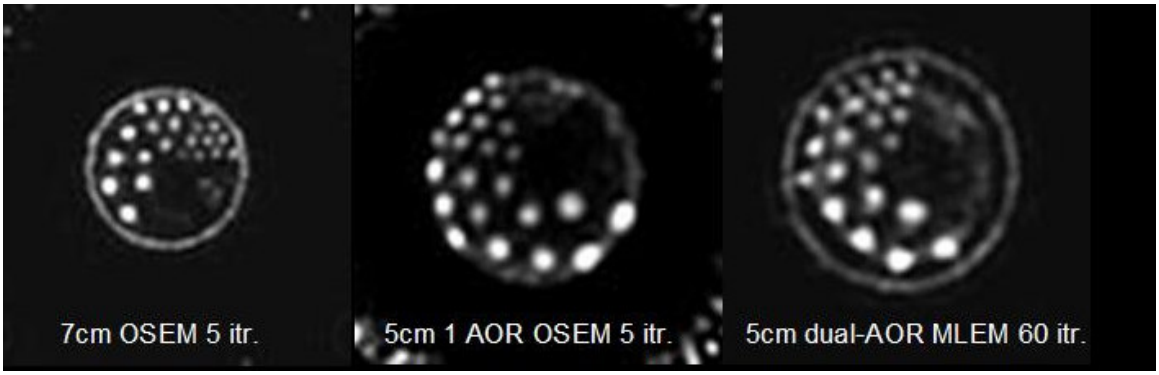

Figure 4.20: Comparison of single-AOR with untruncated projections, single-AOR with truncation and dual-AOR reconstructions. The increase in magnification due to the shorter object length is clear in the images using the shorter object length. The increased magnification allows finer resolution as the 2.5mm rods are more clearly defined in the center and right images. The dual-AOR procedure improves the distortions present in the 5cm single AOR image. A slight ring artifact is present in the dual-AOR image due to slight imperfections in the reconstruction parameters. Development of a more through calibration procedure will help this problem.

more pixels devoted to the image space. This allows greater definition of the hot rods and specifically, the 2.5mm rods are more clearly defined compared to the standard image. The dual-AOR procedure also works to reduce the truncation distortions and artifacts while maintaining the gains in resolution. A slight ring artifact is evident in the dual-AOR image due to a small in the coverage of the object. A more thorough and robust calibration procedure can help to reduce this effect. Overall, the dual-AOR orbit allows higher resolution and similar noise performance for a similar imaging time.

4.3 Validation of anti-myeloperoxidase antibody tracer for SPECT imaging

This study set to provide an initial validation of a novel tracer based upon an anti-myeloperoxidase antibody for imaging sites of neutrophil activity. A mouse infection model was utilized by injection of Staph A bacteria into the left thigh of the mouse and allowing 24 hours for incubation. Presence of infection was confirmed via visual inspection of the treated thigh for inflammation and swelling. Favoring of the leg by the mouse was also taken as an indicator of active infection.

4.3.1 Staph-A inflammation model results

Data from 8 mice are included using the Staph A inflammation model. Staph injected into the mouse thigh results in infection and subsequent inflammatory response

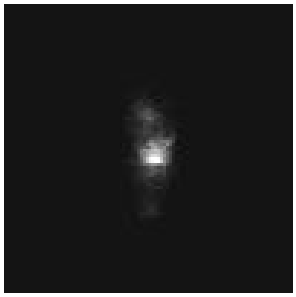

Figure 4.21: Mouse image taken using ^{99m}Tc-1H4 anti-MPO antibody and parallel-hole collimation 90 minutes after tracer injection. Uptake is visible in the bladder and liver, but not within the infected thigh region.

dominated by neutrophil activation. This response can be targeted by labeling appropriate antibodies, for the purposes of this study we used polyclonal immunoglobulin (IgG), and a monoclonal antibody against myeloperoxidase (MPO). The time course of tracer uptake was unknown so animals were imaged at 2 hours and 24 hours after injection of labeled antibody. Figure 4.21 shows a sample coronal view of a mouse after parallel-hole SPECT imaging 90 minutes after injection. The injection site behind the left eye is just visible at the top of the image, but most activity is concentrated within the liver, and bladder. No uptake is seen within the Staph-A infected thigh. The contralateral thigh injected with inert PBS also shows no uptake of tracer.

Figure 4.22 shows a similar image taken using the MPO based tracer imaged after 24 hours. Again the distribution is similar with most activity concentrating in the liver, bladder, but this image also shows increased uptake in the infected thigh. Again no activity was seen in the sham operated contralateral thigh. Imaging confirms increased uptake of the anti-MPO antibody after 24 hours. Similar scans with the IgG based tracer were performed as well to determine any difference in response between the two tracers. Figure 4.23 shows a coronal view of a mouse injected with 99mTc-IgG after 24 hours.

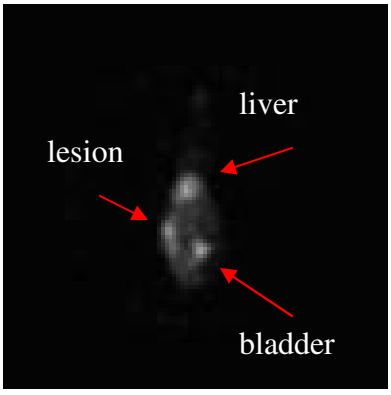

Figure 4.22: Mouse image taken using ^{99m}Tc-1H4 anti-MPO antibody and parallel-hole collimation 24 hours after tracer injection. Uptake is visible in the bladder and liver, but also along the left thigh where the Staph infection was

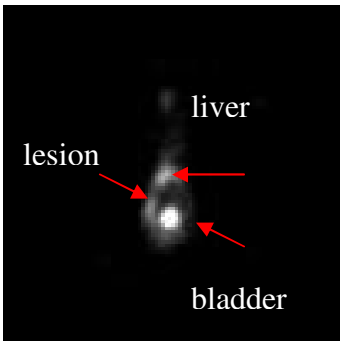

Figure 4.23: Mouse image taken using ^{99m}Tc-IgG and parallel-hole collimation. Uptake is again visible along the left thigh where the Staph infection was located.

Initial experiments using our Staph inflammation model, have shown increased uptake of both anti-MPO and IgG antibodies, but have not proven the specificity of the anti-MPO antibody for sites of neutrophil activation. The dose effect of the injected tracer was examined by using varying titers of antibody mass for injection. For this experiment, 50ug, 10ug, and 5ug doses were prepared and labeled with ^{99m}Tc. Mice were prepared using the same Staph model as before and the tracer was injected 24hr prior to imaging. The uptake in the infection region was characterized as a percentage of liver uptake. Liver function was assumed to be normal in all mice and thus hepatic uptake was deemed to be a suitable control for injected dose, animal body weight, and isotope decay.

Drawing regions-of-interest over both the liver and the infected area showed no significant differences in the liver/infection ratio between the anti-MPO and the IgG treated mice. The results are seen in Figure 4.24. Further refinements to the model and additional experiments are required to validate the anti-MPO tracer for use with neutrophil activation and not more generalized immune response.

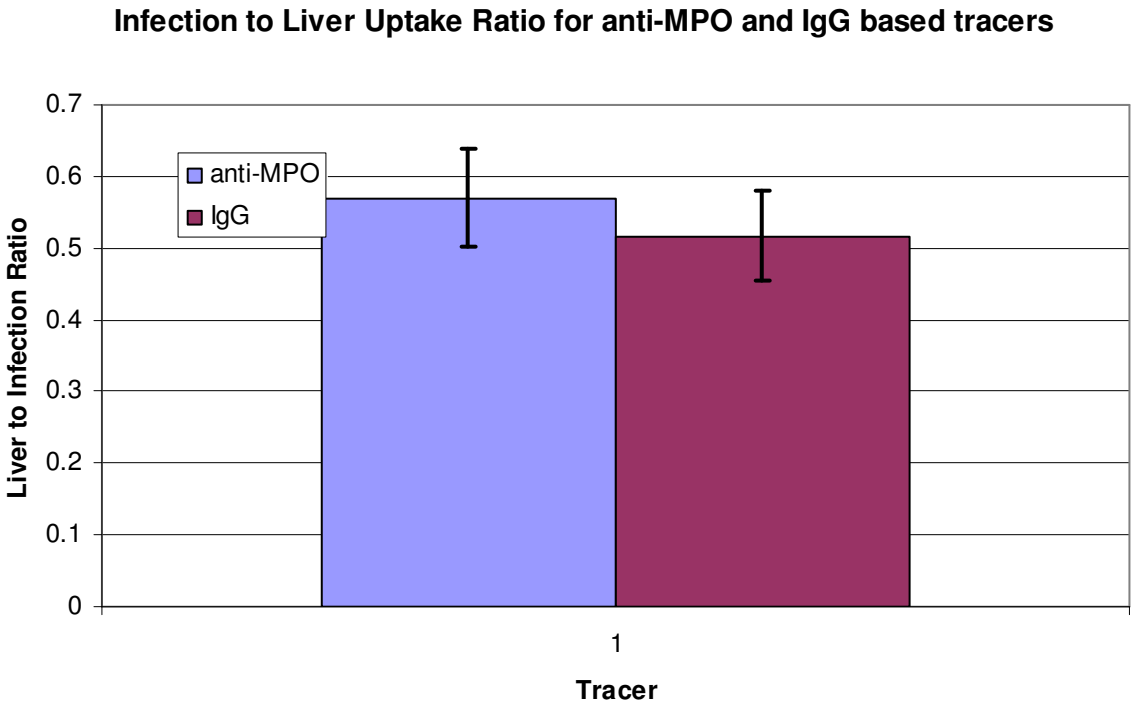

Figure 4.24: Ratio of image intensity in the infection site to image intensity within the liver. The anti-MPO tracer was not significantly better at localizing to the infection site than the polyclonal IgG. While it is possible that the anti-MPO is localizing to areas of neutrophil activation it is difficult to separate this response from the more generalized immune response.

4.3.2 Specificity of anti-MPO tracer within MPO Knockout Mice

The results from section 4.3.1 were not encouraging based on the lack of difference in uptake ratio of the two tracers. To test that the similar performance was not a function of the animal infection model, three mice were bred without the ability to produce the myeloperoxidase protein. Presumably, because the mouse would have no expression of MPO, there would not be any antigen for the anti-MPO antibody to bind to and we would not see any uptake within the infected region. Three mice were scanned, one with the IgG based tracer and two with the anti-MPO based tracer. Figure 4.24 shows the result of imaging performed on the $MPO^{-/-}$ mouse.

The images presented in Figure 4.25 confirm that the anti-MPO antibody 1H4 localized within the infected area even though no myeloperoxidase was present. This would strongly suggest that the 1H4 antibody is not specific to regions of MPO concentration, but will also accumulate in regions of general immune response. It is possible that some 'piggyback' effect exists where the antiMPO antibodies travel along

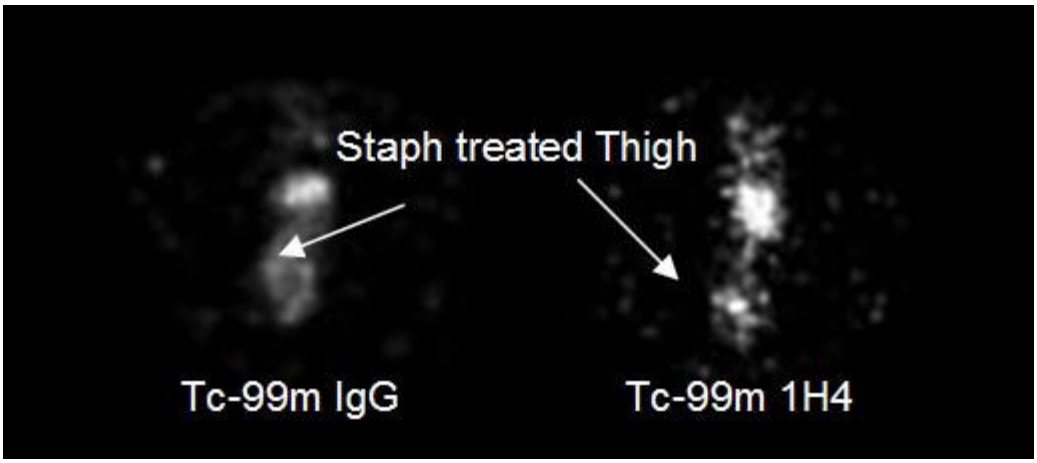

Figure 4.25: MPO knockout mouse injected with IgG (left) and antiMPO antibody (right). Both images show uptake within the infected thigh confirming that the anti-MPO tracer binds to secondary antigens other than myeloperoxidase.

with other immune cells to the site of infection. Nevertheless, because the ANCA model results in nephritis and vasculitis, even though myeloperoxidase is present in the ANCA lesions, the inflammation of the endothelial wall may also induce expression of other factors that may preferentially bind to the 1H4 tracer. As such it would be impossible to tell if uptake was related to myeloperoxidase concentration or a more general inflammation response. This uncertainty in binding characteristics would make interpretation of the images difficult and reduce the scientific usefulness of the tracer.

4.4 Noninvasive Hematocrit Measurement during Ischemic Stroke

The noninvasive measurement procedure as proposed by Loutfi used multiple scans within a single subject to obtain the required RCV and PCV volume information. Because those methods were derived for human studies where stroke onset cannot be controlled, they may not be optimal for an animal study with more precise control over the ischemic conditions. This study was broken into two sections: the first section used a preloading method to take advantage of the controlled onset of ischemia, and the second used the methods of Loutfi modified for small-animal imaging.

4.4.1 Preloading Method for Noninvasive Hematocrit Evaluation

The MCAO filament model for occlusion places a plug at the entrance to the middle cerebral artery thereby completely halting flow past the MCA. A concern was that collateral vessels would be unable to compensate for the MCA block and tracer would not be allowed to enter the ischemic space when injected. The preloading concept calls for injection of tracer prior to MCA occlusion to allow the tracer to equilibrate within the tissue. For each rat, HMPAO images were processed to establish presence of a lesion and matched to the corresponding perfusion-weighted MR images.

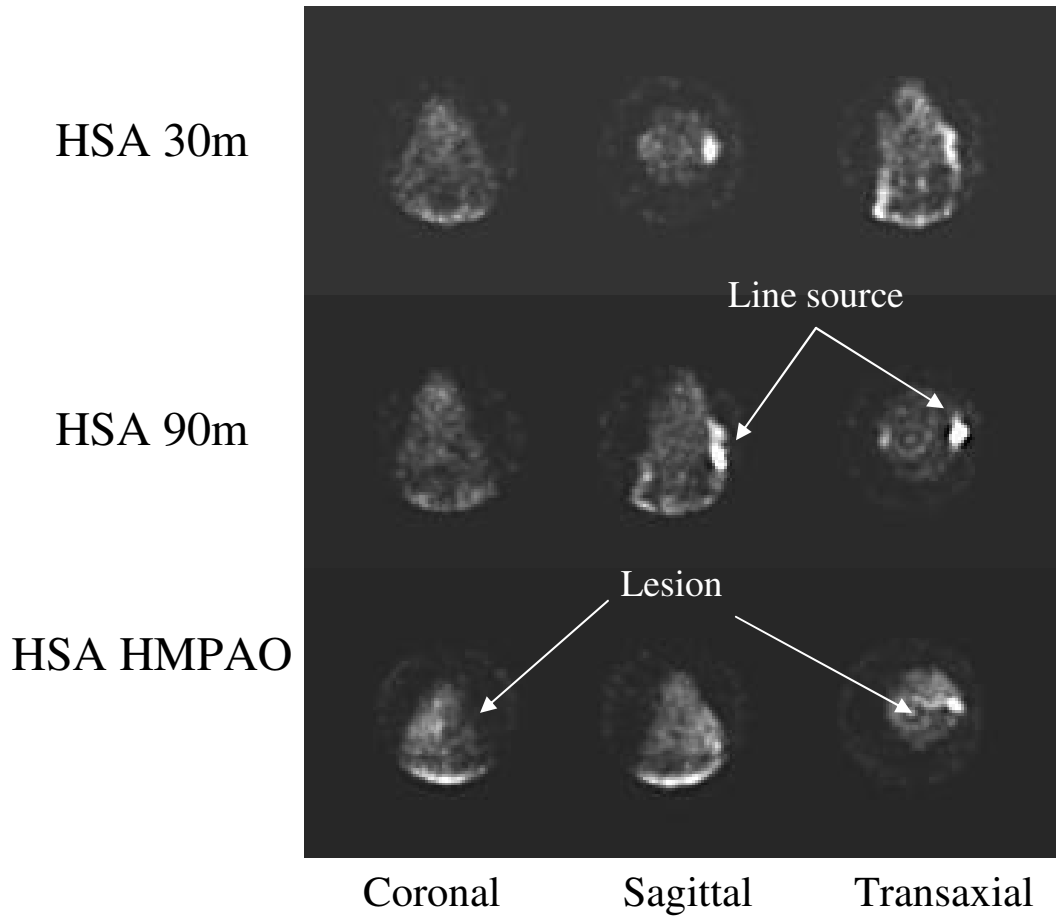

Figure 4.26: Sample Tc-99m HSA images shown after 30 minutes and 90minutes of ischemic conditions. HMPAO images are shown to define regions of reduced perfusion and highlight the ischemic lesion.

Figure 4.26 shows sample reconstruction slices of SPECT acquisitions at 30m and 90m post-MCAO for a rat injected with ^{99m}HSA along with the perfusion image. The HMPAO perfusion image clearly shows reduced uptake in the hemisphere containing the ischemic lesion allowing for identification of appropriate ROIs. Upon visual inspection, little difference between the ischemic and control hemispheres is evident in the plasma image, but ROI analysis will quantify the image intensities in the ischemic and control regions.

Figure 4.27 shows the MR images acquired for the same HSA rat as displayed in Figure 4.25. The MR images (A) and (B) are perfusion-weighted images taken 60min

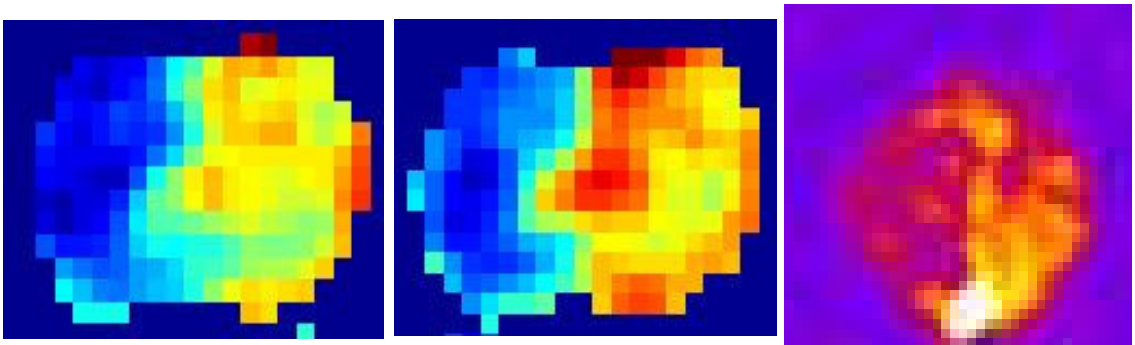

MR CBF 60m MR CBF 120m SPECT HMPAO

Figure 4.27: Axial slices of MR perfusion images along with SPECT HMPAO image. All images show reduced perfusion in the left hemisphere with gradual worsening from 60m to 120m. The SPECT image supports the MR findings and confirms that lesions seen in SPECT images roughly correspond to MR lesions. This provides a basis for comparison of images between the two modalities.

and 120min after MCAO. The HMPAO (C) is shown to provide perspective between the MR data and SPECT data. The perfusion-weighted images show strong similarities with the HMPAO SPECT perfusion image which confirms the ability of HMPAO SPECT to identify the ischemic lesion. In both images approximately one hemisphere of the brain shows significant decrease in signal intensity, corresponding to reduced blood flow. The similarities between the two images allow comparisons between the two modalities and allow SPECT ROIs to be roughly translated back to MR images. It should be noted that the physical differences in orientation, as well as image properties do not allow direct registration of the SPECT and MR images, only that the two datasets can be compared on a broad basis. The MR PWI calculation was only performed on the region identified as brain, while the SPECT HMPAO image includes the entire head within the ROI. The SPECT image also includes a fiducial marker located at the base of the skull, seen as a bright spot at the bottom of the image.

A population of six rats was injected with ^{99m}Tc-HSA using the preload procedure. Comparison of control and lesion ROIs show a reduction in plasma volume within the ischemic lesion. The comparison is seen in Figure 4.28.

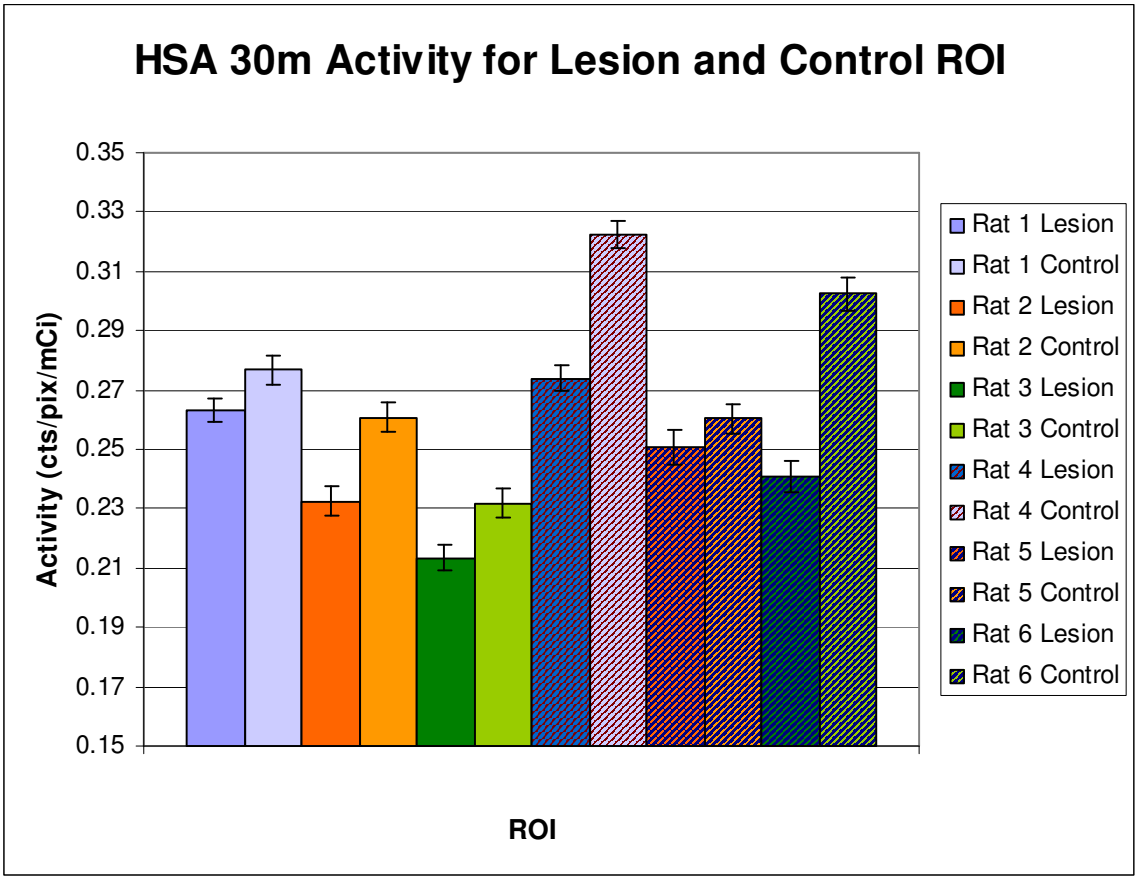

Figure 4.28: The HSA image intensity was shown to be significantly lower in the lesion ROI when compared to the control ROI. This indicates a loss of plasma concentration in the ischemic region further supporting the hypothesis that hematocrit increases under ischemic conditions. When this data is compared with the data from Figure 3, a clear picture arises with RBC concentration increasing and plasma concentration decreasing, resulting in an overall hematocrit increase.

For completed experiments, the hematocrit examination has been performed as a comparison between normal and ischemic brain tissue for each blood component independently. Using the current methods it is impossible to calculate the actual hematocrit value for a single rat, as each rat only receives a single tracer. Even with these limitations, the experiments allow useful information to be inferred from the images. Relative changes in either RBC distribution or plasma distribution as visualized

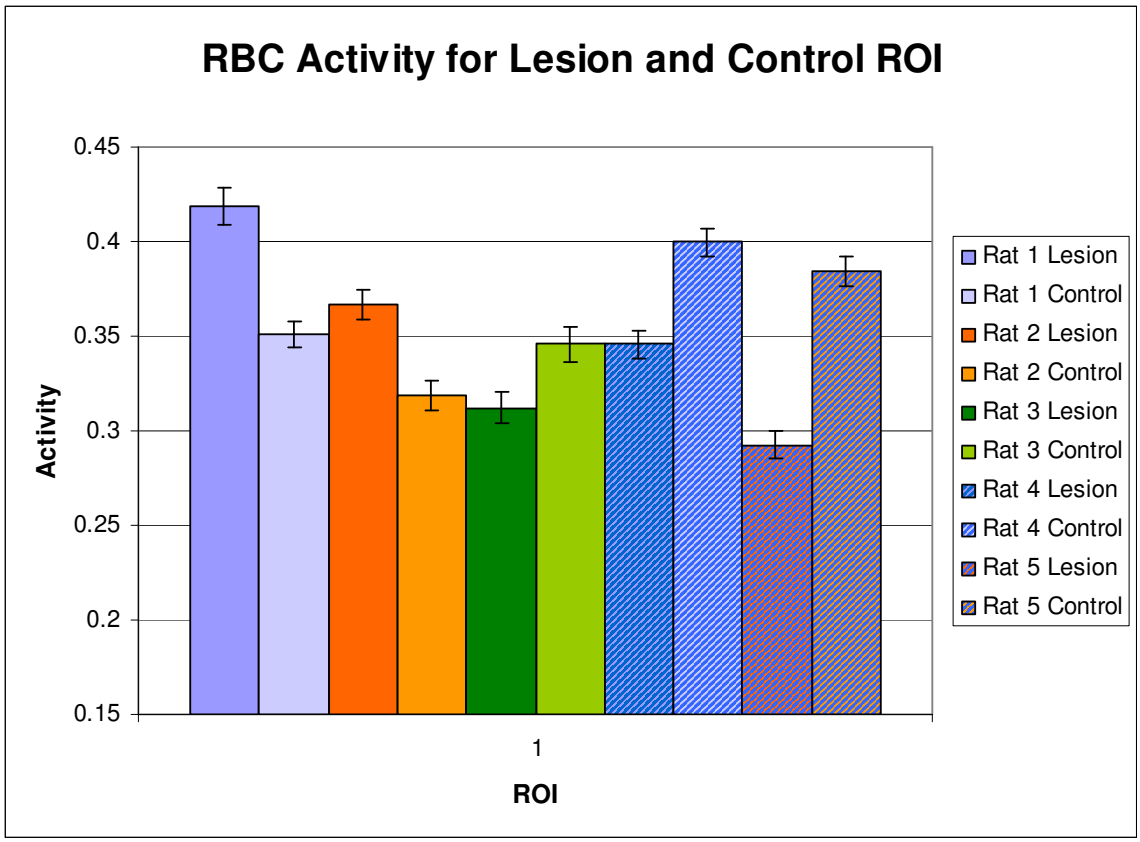

Figure 4.29: ROI analysis on images taken with the Tc-labeled RBCs show no pattern of intensity changes within the lesion ROI with respect to the control ROI. For some rats the lesion intensity is higher than control intensity, which would indicate an increase of RBC to the lesion, while in others the intensity is lower indicating an exodus of RBC from the lesion.

by HSA and RBC imaging can be measured with ROI analysis. Figure 4.29 shows the relative changes in RBC distribution within the five rats scanned. It is not clear from Figure 4.29 if the RBC intensity within the lesion is higher or lower than the control. The data shows inconsistent results. All differences are statistically significant with p-values under 0.05.

With the HSA images we saw clear and consistent differences between the lesion and control ROIs. For all rats the data showed a consistent decrease in the HSA intensity within the lesion, which would indicate a loss of plasma in that area. Unfortunately, from the data seen in Figures 4.28 and 4.29, we cannot make a determination about the

hematocrit changes within the ischemic lesion. Clearly plasma concentration decreases, but RBC concentration shows no consistent response.

The results from Figures 4.26-4.29 allow examination of blood changes during ischemic conditions, but measurements during reperfusion phase would also be valuable. Complicating the imaging protocol during reperfusion is the lack of a suitable landmark for defining the lesion and control tissue. The RBC and HSA images shown for the ischemic conditions do not provide a suitable landmark indicating the location of the lesion, so HMPAO images were used. When imaging during reperfusion, however, HMPAO images cannot be used because the occlusion will be removed prior to injection of the HMPAO and recanalization should eliminate any difference in perfusion between the two hemispheres. Perfusion imaging required different methods.

4.4.2 In Vivo hematocrit measurement within ischemic rat brain

The work performed by Loutfi (Loutfi, Frackowiak et al. 1987) and Sakai (Sakai, Igarashi et al. 1989) provided the base for similar experiments within the MCAO rat stroke model. The ability of the HSA and RBC tracers to penetrate the ischemic lesion caused some concern, but the images shown in Figure 4.30 show sufficient signal from the affected hemisphere when tracer was injected 90min after MCAO. Either collateral flow or incomplete occlusion allows for tracer to enter the ischemic area and be detected at acceptable noise levels. Positive confirmation of sufficient signal for measurement encouraged the progression of the study to more quantitative measures.

4.4.2.1 Validation of quantitative measurement

Because the method required the use of two different tracers both using the same radioisotope, a short experiment was performed to confirm the quantitative accuracy of

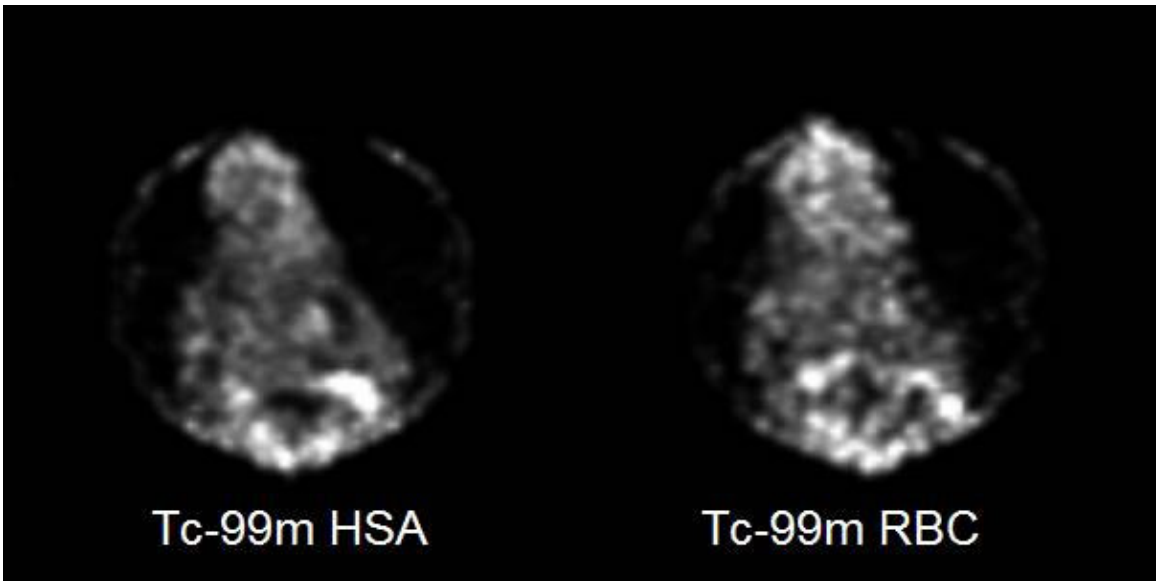

Figure 4.30: ^{99m}Tc-HSA and ^{99m}Tc-RBC images show uptake within the tissue affected from MCA occlusion. Collateral flow is sufficient to allow for tracer to enter the lesion and provide an acceptable signal to noise ratio. Images were taken with 1mm pinhole. M = 1.6, 60 projections, 20sec/projection, OSEM 5itr 6 subsets.

the hematocrit calculation. The sources were created from blood samples taken after injection of the radiotracers. The first sample only included the ^{99m}Tc-HSA tracer, and the second sample included both the ^{99m}Tc-HSA and the ^{99m}Tc-RBC tracer. The sources were imaged using SPECT under the exact same conditions as the proposed animal experiments, 60 projections, 20 seconds per projection, OSEM reconstruction. The reconstructed images were processed using ROI analysis with each ROI encompassing the entire source. The source size allowed both sources to be imaged simultaneously and a sample projection and reconstruction image is seen in Figure 4.31.

The image clearly shows the difference in signal intensity between the two samples because of the difference in tracer activity, and the average hematocrit calculation for five samples results in measurements 0.39. Comparison of this method to the centrifuge method yields good results with the average centrifuge hematocrit measurement for 5 samples being 0.40. These values are within the range for large vessel

hematocrit values witnessed from experience measuring the hematocrit via centrifuge, and from the literature. Confirmation of the quantitative nature of the imaging methods allowed progression of the study to the animal stroke model.

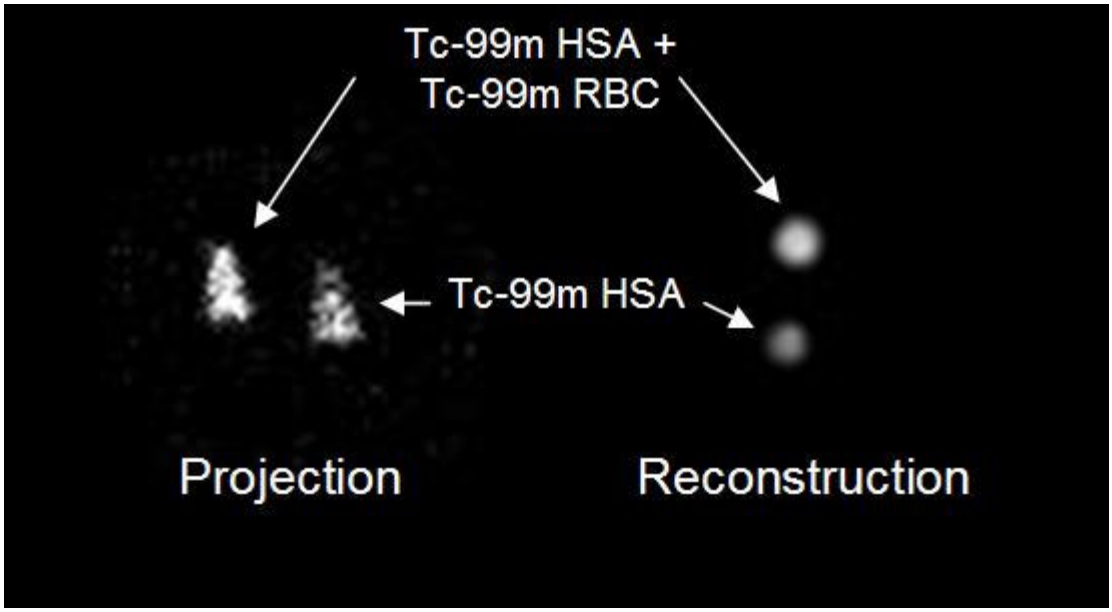

Figure 4.31: Blood samples taken from a rat after injection of ^{99m}Tc-HSA, and both ^{99m}Tc-HSA and ^{99m}Tc-RBC. ROI analysis was performed upon the sources and hematocrit was calculated to be 0.39

4.4.2.2 Hematocrit Calculation using MCAO stroke model

The study included two groups: one group of 5 rats undergoing 90 minutes of MCAO before injection of tracer, and one group of 5 rats undergoing 90 minutes of MCAO along with 120 minutes of reperfusion before injection of tracer. For all rats the HSA tracer was injected first because the blood samples are easier to measure, than when RBC is injected first. Because the hematocrit calculation requires multiple scans taking about 30min each, the hematocrit value represents an average over the duration of imaging. For this experiment, that duration was ~1 hr, so the calculation represents the

average value between 90 min and 150min post MCAO. The hematocrit rate of change was expected to be slow enough to not differ between scans, so the time resolution of SPECT was sufficient for this study.

After the completion of the HSA and RBC scans, 5-7mCi of buffered HMPAO was injected to acquire a perfusion image and identify the location of hypoperfusion, which appears as a cold lesion. The HMPAO image was used to draw regions of interest within the cold lesion and the contralateral control region. Because the rat was fixed for all three scans, the ROIs drawn in the HMPAO image were directly applied to the HSA and RBC images. Figure 4.32 shows the HMPAO, RBC, and HSA images along with the ROIs used for analysis for all five rats within the group. Lesion ROIs are denoted with green, while control ROIs are shown as blue. The ROIs were applied to three consecutive sagittal slices that showed clear perfusion defects.

Image intensities from the ROI measurements were used along with blood samples taken during the scans to calculate the hematocrit values. Table 4.1 shows the ROI values along with hematocrit values for each ROI within the 5 rats. Hematocrit values varied between 0.21 and 0.55, which roughly agree with values published in human and rat studies (Lammertsma, Brooks et al. 1984; Kuke, Donghua et al. 2001). Comparison of the control ROI to the lesion ROI shows that in 5 of 5 rats, the lesion hematocrit level was higher than that control hematocrit, with 4 of 5 differences statistically significant. The paper from Loutfi examined hematocrit changes during the acute phase of ischemia and also noted an increase in hematocrit levels in the ischemic lesion for patients with stroke.

Table 4.1: Results of hematocrit calculation for rats treated with 90min MCAO

Rat	*A*	*B*	*C*	*D*	*E*	*Mean*	*Stdev*
Lesion Hct	0.38	0.46	0.55	0.33	0.39	0.42	0.09
Control Hct	0.37	0.22	0.43	0.38	0.28	0.34	0.09
Difference	0.01	0.24	0.12	-0.05	0.11	0.08	

A second group of rats was treated with 90 minutes of MCAO occlusion followed by a 120 minute reperfusion period. SPECT imaging was performed immediately after the reperfusion phase, with the HSA image acquired before the RBC image. As with the earlier group, an HMPAO scan was performed to identify perfusion levels and determine if recanalization was complete, or if some perfusion defect persisted. Images shown of the five rats are presented in Figure 4.33. The HMPAO images for rats 1 and 3 show reperfusion levels within the lesion that are slightly higher than normal, a hyperperfusion effect that has been noticed in other reperfusion studies. For rat 2, however, the HMPAO intensity within the lesion ROI was only 86% of the control ROI, suggesting an incomplete recanalization and persistent perfusion defect.

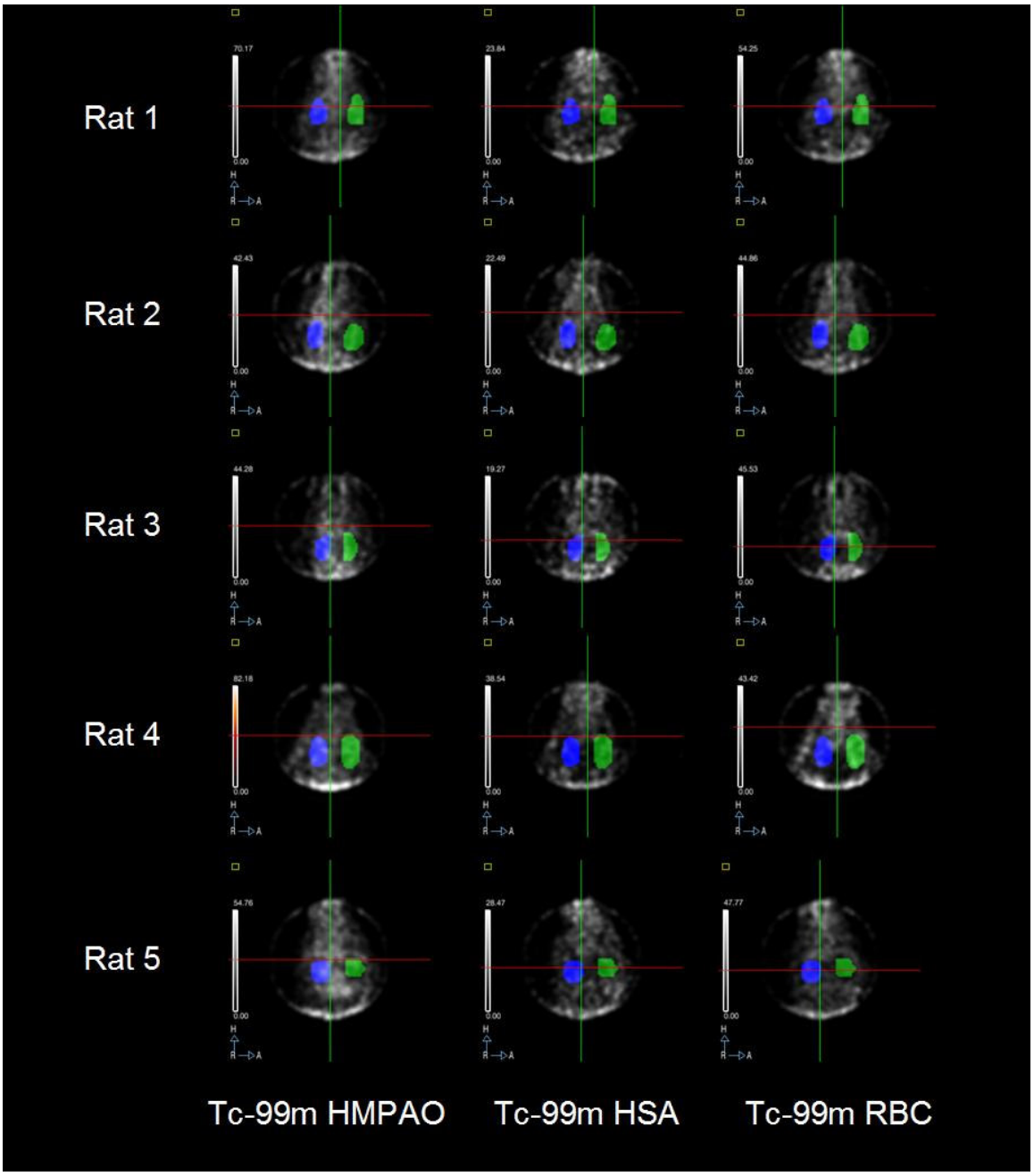

Figure 4.32: The HMPAO image was used to identify the regions of interest for the RBC and HSA images for rats treated with 90min MCAO. Lesion ROIs are shown in green, and control regions in blue. The rat skull was fixed using a bite-bar so the images are well registered.

The hematocrit values for the reperfusion rats were not as consistent as for the ischemic rats. Table 4.2 shows the hematocrit values for the 5 reperfusion rats. Reperfusion rat 1 lesion hematocrit was 0.21 while control hematocrit was 0.35, a significant decrease in hematocrit value and blood viscosity within the reperfused tissue,

but rats two and three showed slightly higher hematocrit levels within the lesion ROI. Overall, hematocrit values within the reperfused tissue were lower than hematocrit values within ischemic tissue. This may indicate that blood rheology returns to a normal state and may not 'overshoot' to lower hematocrit values as compensation. The hematocrit values may depend upon cerebral blood flow and perfusion values. The hematocrit values within the lesion ROIs for the ischemic and reperfusion rats were plotted with the HMPAO defect to look for correlation. Figure 4.33 shows that as the perfusion value increases, hematocrit tends to decrease. This pattern was somewhat expected from the literature as a compensatory effect for ischemia. In fact, one paper

Table 4.2 Results for hematocrit calculation for rats treated with 90min MCAO and 120min reperfusion

Rat	*A*	*B*	*C*	*D*	*E*	*Mean*	*Stdev*
Lesion Hct	0.21	0.37	0.34	0.27	0.35	0.31	0.07
Control Hct	0.35	0.36	0.30	0.31	0.20	0.30	0.07
Difference	-0.14	0.01	0.04	-0.04	0.16	0.01	

found that in patients with elevated hematocrit reperfusion was diminished and the prognosis for recovery was worse (Allport, Parsons et al. 2005).

Because of the small number of samples, assumption of a Gaussian population distribution may be invalid so nonparametric statistical tests are required. The nonparametric correlation coefficient is the Spearman coefficient and is analogous to the Pearson coefficient for normally distributed data. For the data in this study, comparison of HMPAO perfusion data with hematocrit values resulted in a Spearman correlation coefficient for HMPAO and hematocrit was -0.88 with a p value of 0.03 suggesting a very strong negative correlation.

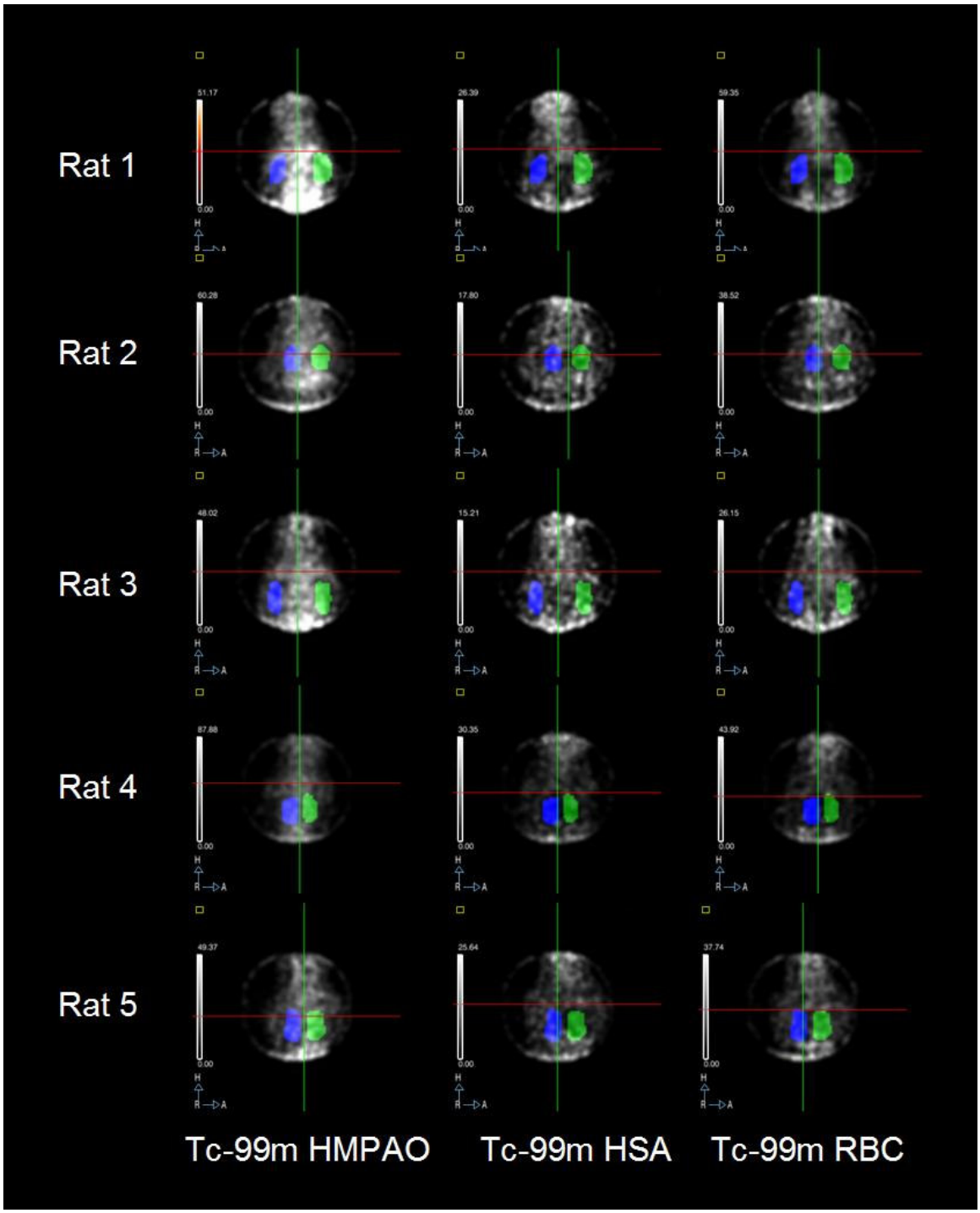

Figure 4.33: Perfusion images along with HSA and RBC images are shown for 5 rats treated with 90 min. MCAO followed by 120 min reperfusion. All rats showed better perfusion within the lesion ROI compared to the ischemic rats, with one rat slightly hypoperfused (86% normal), and two rats slightly hyperperfused (116% normal, and 126% normal). Hematocrit values within in the lesion ROIs varied from 0.21 to 0.37, while control hematocrit varied between 0.29 to 0.35.

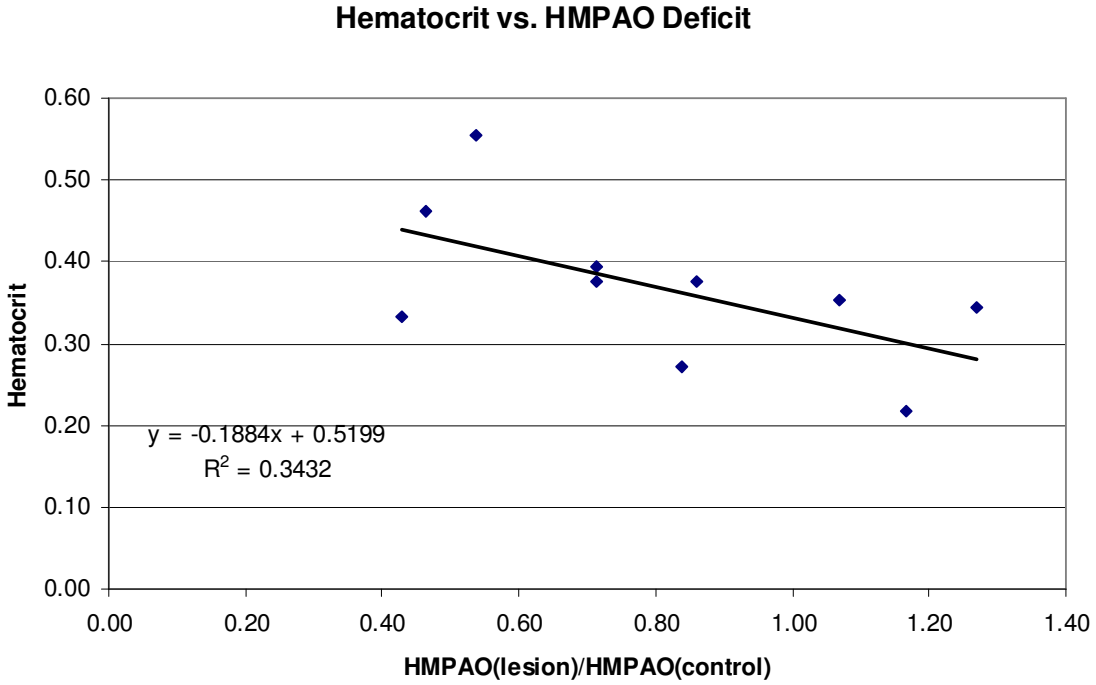

Figure 4.34: Perfusion image intensity correlated negatively with hematocrit values. The ratio of HMPAO lesion intensity to HMPAO control intensity is plotted against hematocrit. Decreases in perfusion tended to show an increase in hematocrit levels.

The plot shown in Figure 4.34 presents the hematocrit as a function of the HMPAO ratio between the lesion and control ROIs. A linear fit is provided as a first approximation for the relationship between hct and perfusion, and the R^2 value of 0.66 also suggests strong covariance between the two variables. This finding may support previous research that the hematocrit value is dependent upon blood flow and not necessarily oxygen deficiency. Future work varying the length of the MCA occlusion and time of reperfusion may help to clarify how changes in hematocrit vary and if longer occlusion results in lower perfusion results.

Figure 4.34 includes data points from the 90min MCAO rats as well as the 90min MCAO plus 120 min reperfusion rats. Because the HMPAO behavior should be

consistent between the two groups and only depend upon perfusion, comparisons of perfusion between the two groups are valid. We see that for a few rats, the ratio between HMPAO within the lesion and HMPAO within the control ROIs is larger than one. This would suggest a hyperperfusion within the reperfused tissue and is consistent with hyperemia following ischemic events. Likewise the ischemic rats all show lesion/control HMPAO ratios of less than one, indicating a reduction in flow.

Chapter 5

Conclusions

The evolution of preclinical research has placed greater emphasis upon nondestructive methods which can provide *in vivo* data without requiring animal sacrifice. Modern technology has provided several imaging modalities such as PET, SPECT, MR, CT and ultrasound to allow researchers the ability to answer ever more advanced hypotheses. The choice of modality depends upon the specific requirements of the study such as spatial and temporal resolution, sensitivity, and analytical analysis. The work in this thesis focuses exclusively upon SPECT and the preceding chapters have discussed methods to improve SPECT and increase the utility of the method for a broader set of studies as well as show work from appropriate animal applications. This chapter will attempt to provide some perspective on the results and a sense of how they fit with the current literature.

5.1 Dual Circular Plane Orbit for Pinhole Tomography

The results seen in Section 4.1 provided both simulation and experimental confirmation of the utility of the dual-circular orbit for pinhole tomography. The nature of the pinhole geometry dictates that pixels that lie above or below the orbit plane are not viewed from opposing angles and therefore do not meet the criteria set by Orlov or Tuy for completeness. To compensate for this deficiency, a pinhole trajectory must include an axial component. Several pinhole trajectories have been proposed to enhance data

completeness. Some of these orbit trajectories seem odd, such as the circle plus line orbit proposed by (Zeng and Gullberg 1992) A successful and useful orbit trajectory will provide for complete data and be easy to implement mechanically. One particular trajectory that fits both criteria nicely is the helical orbit. Originally developed for cone-beam CT imaging, it is equally suitable for pinhole SPECT.

The dual-plane orbit was not developed to compete directly with the helical-orbit since the trajectory cannot provide complete data for the entire object. What the dual-plane orbit lacks in theoretical robustness, it makes up with simple implementation. Using the OSEM algorithm for reconstruction of the dual-plane projections, small deficiencies in data completeness can be tolerated. The simulations in section 3.1.1 confirm that the dual-plane orbit can improve image quality and extend the axial FOV relative to a single-orbit scan. This improvement allows a single-pinhole scanner to image long objects accurately even with a small-FOV. From an applications point of view, the dual-orbit scan could be extended for multiple orbits indefinitely which would allow full-body imaging of mice and rats at pinhole resolutions. The cost comes with longer imaging times and lower temporal resolution.

An unexpected result from the experiments performed in Section 4.1.2 was the effect of the shape of the FOV upon the quality of the reconstruction. The circular FOV of the microSPECT detector results in varying degrees of data completeness depending upon the length of the chord across the FOV at a given axial location. For a single orbit scan, the effect is negligible because other factors such as detector intrinsic resolution or the noise level dominate the image quality, but for a dual-plane acquisition, the relationship between the two fields-of-view can result in varying noise levels and data

completeness within the overall field of view. The image space is no longer shift invariant and the signal acquired from the object will differ according to the object's location within the combined FOV. Because this effect depends upon the volume of overlap between the two FOVs, using the proper pitch can help to minimize these effects and the simulation data in Section 4.1.4 showed that the optimum pitch is such that the object is divided into halves, with the center half covered by both orbits, and the outer quarters covered by only one.

The results from Section 4.1.5 show that although careful setup and pitch choice can minimize the artifact, it is also relatively simple to correct for the local variance in signal intensity with a normalization image tuned for the specific geometry. While the acquisition of a normalization image adds to the complexity and length of an imaging, some demanding applications may justify the increased effort in order to more faithfully reconstruct a longer field-of-view. As a simple cylinder phantom of approximate size to the desired object is all that is required, the acquisition of a normalization image should not pose a major obstacle for implementing the dual-plane method.

While the dual-plane acquisition method does not offer a perfect solution to the long-object problem, it does provide an alternative to single-orbit scanning which is easy to implement. No change to either the reconstruction algorithm, or system hardware was required, making the method efficient for simple SPECT systems and facilities without the resources required for software development or purchase of more advanced systems.

5.2 Dual-AOR orbit for truncation correction

The basic theory and physics behind both the dual-plane and dual-AOR acquisition orbits is quite similar. The two approaches both attempt to increase the

limited FOV of a pinhole camera by performing multiple acquisitions from different perspectives. While the approach to both projects seems similar, the two methods were designed to improve different deficiencies. The dual-plane acquisition was designed to improve axial sampling and FOV, while the dual-AOR orbit was designed to improve transaxial resolution by allowing more favorable geometry for the pinhole collimator.

The basic concept of using multiple scans for situations of truncated data has been applied previously, described in a paper from Kadrmas (Kadrmas, Jaszczak et al. 1995). In that paper, the methods focused upon development of a dual-scan method for truncation correction for transmission CT. The concepts described in that paper differ slightly than those described within in this dissertation, but the intent was similar. Kadrmas's methods required development of a unified projection set using the views from one set to explicitly fill in the missing views from the other and then use FBP for reconstruction. Our methods do not explicitly combine projection sets into one complete set, but instead use an iterative algorithm and perform the backprojection/projection estimates for two truncated datasets. Our methods work well for pinhole SPECT where matrix sizes are manageable, but may not be applicable for CT images due to the increased computational demand.

The results presented in Section 5.2 confirm, both with simulation and experimental data, the ability of the dual-AOR orbit to compensate for truncation thereby increasing the transaxial field-of-view and allowing greater magnification levels. The method provides a straightforward solution to increase the resolution of a pinhole collimator. Although conceptually simple, application of the method to studies requires some preparation and careful planning. When the geometry is setup properly, all parts of

the object are included in either of the two fields of view, with the two FOVs meeting before the proximal edge of the object. It is deceptively easy to overestimate the cone angle and move the object too close to the aperture, as illustrated in Figure 3.3. The pitch required to cover the edge truncation then introduces a blind spot between the two FOVs at the region of the animal proximal to the pinhole. The method only works if each voxel in the image space is viewed by at least one of the two scans, but the blind spot creates a small area where the voxels disappear. The missing data results in inconsistencies in the projection data and ultimately causes severe reconstruction artifacts.

Another potential problem for the dual-AOR approach is the increased number of geometrical parameters that must be accounted for so backprojection and projection steps can be applied during the reconstruction. Several papers have described methods for pinhole calibration (Beque, Nuyts et al. 2005) and generally a single pinhole orbit requires seven separate independent geometrical variables to be either measured or assumed (Beque, Nuyts et al. 2003) . Mismatches between the true values and measured values can result in severe artifacts. The increased number of geometrical parameters with the dual-AOR orbit increases the number of possible mismatches and the severity of potential artifacts. For this reason a robust and accurate calibration method is critical for maximum resolution in the reconstructed image. The increased FOV and magnification gained from the orbit are too easily lost from sloppy calibration. The calibration method for the experiments in this study required reconstruction of a 1mm line source at each AOR location and adjusting the reconstruction parameters to minimize the width of the reconstructed line. Admittedly, this method does not provide the precision of a more

rigorous calibration program and the maximum resolution attained with the method could likely be improved. Also, manually adjusting the parameters is a tedious and time-consuming process and inefficient for high-volume applications where the AOR locations are changing frequently.

An unexpected result of this study was the image quality using the truncated projections. Overall, the image was quite good except for some minor distortion at the edge of the FOV. This has implications for studies where the region of interest does not include the entire animal, such as a cardiac study. The heart could be placed as close as possible to the axis of rotation and even if the body of the mouse falls out of the FOV, the heart will be reconstructed at good quality. This development somewhat negates the need for the dual-AOR scan for very small regions of interest.

The results presented within this dissertation validate the utility and effectiveness of the method for improving the performance of a small-FOV pinhole camera. Combined with a rigorous calibration procedure, the dual-AOR approach offers the potential for submillimeter resolution without significant increase in imaging time. The development of this method has increased the potential of the microSPECT system, which was ultimately the desired conclusion.

5.3 Validation of anti-myeloperoxidase antibody based tracer

The role of myeloperoxidase for small-vessel ANCA-related vasculitis has been well documented (Kallenberg 1998; Souid, Terki et al. 2001; Suzuki 2001; Xiao, Heeringa et al. 2002). Because of the importance of MPO in the disease manifestation, an antibody against it was considered to be a suitable imaging marker for the progression of ANCA-induced vasculitis. Regions of increased MPO concentration correlate to

regions of increased neutrophil activity, which makes anti-MPO antibody encouraging potential markers for regions of ANCA activity. Although mouse models for ANCA-induced vasculitis exist, they were deemed too expensive for initial tracer validation. Instead, the Staph-A infection model was used to determine the affinity of the tracer for regions of inflammation and general immune response. Both the anti-MPO antibody and a control tracer based on polyclonal immunoglobulin (IgG) showed high affinity for the Staph infected region. The IgG based tracer was not expected to exhibit the same affinity for the infected site as the anti-MPO antibody based tracer. This is because the immune response to a bacterial infection was expected to be dominated primarily by neutrophil activity. Because MPO is one of the more common enzymes expressed by neutrophils, the anti-MPO tracer was expected to show higher affinity for the inflammation than the IgG-based tracer.

Unfortunately, the data in Section 4.3.1 show both tracers to exhibit similar affinity for the thigh infection. Because this was a pilot experiment, a quantitative analysis was not attempted for most mice and qualitative judgments were used to evaluate the relative affinity of each tracer for the inflamed region. An attempt to assess the specificity of the anti-MPO based tracer was made using an $MPO^{-/-}$ mouse which does not express MPO. Images showing the anti-MPO tracer localizing to an infection within an $MPO^{-/-}$ mouse would provide strong evidence that the tracer is not specific to MPO and shows affinity for secondary targets. Because the ultimate goal is to use the tracer within ANCA mouse models to examine kidney vasculitis, the affinity for the tracer to regions of ANCA activity is critical. The affected area within the mouse kidney

is expected to be quite small so it is imperative that any signal detected comes from the ANCA and not from a secondary target.

One possible explanation for the negative result could be alteration of the functional long-chain of the antibody during the chelation and ^{99m}Tc labeling processes. Care must be taken to develop the chemistry so as to not affect the active regions. Other tracers such as Gallium (Querol Sans, Chen et al. 2005), or nanocrystals (Hoshino, Nagao et al. 2007) have been successfully bound to anti-MPO antibodies without adversely affecting the long chain, but a literature search has not shown successful labeling with ^{99m}Tc.

Also, the use of the Staph-A infection model may not be appropriate for the validation of the tracer as proposed. The IgG family of antibodies has been shown to express affinity for Staph-A proteins (Mackenzie, Warner et al. 1978) so our hypothesis that anti-MPO antibody would show greater affinity for the infection than IgG may have been faulty. The ideal validation experiment requires using the full ANCA mouse model for imaging. If the images allow visualization of uptake within the kidney, histology and autoradiography can confirm localization of the tracer within the endothelial cells lining the vessel. Autoradiographs are specialized equipment and somewhat uncommon to find in imaging labs, but they are critical for validation of tracer specificity.

To conclude, the experiments presented within in this dissertation did not confirm the specificity of an anti-MPO antibody based tracer. Because the model used for tracer validation was not the same model we would ultimately like to use, it is difficult to determine if the negative result is the fault of the tracer, or the experimental model.

Future work may help to provide confirmation, either positive or negative, for the utility of the tracer for imaging ANCA-induced vasculitis.

5.4 In-vivo measurement of hematocrit using SPECT

5.4.1 Experimental Conclusions

Experiments using the preload method suggested that hematocrit levels during ischemic conditions may increase, but since each rat only received a single tracer, actual calculations of hematocrit were not possible. Analysis of the changes between lesion and control ROIs for both the RBC and HSA tracers showed that plasma levels decreased, but RBC levels stayed somewhat level, indicating a hematocrit rise due to loss of plasma volume. The preload experiments provided a tantalizing glimpse of the rheological changes during ischemia, but ultimately were not suited for true quantitative analysis due to the multiple groups for each tracer.

Development of methods where both tracer distributions can be examined within a single animal study allowed for decreased interanimal variability. With each animal receiving cellular and plasma tracers, an explicit calculation of hematocrit was also possible using SPECT. Initially, the large number of potential errors led to concerns over the accuracy of the calculation. Potential sources or error included parameter estimation for pinhole reconstruction, error with handling the blood samples, and error determining the location of the regions of interest in addition to statistical variation. The position of the ROIs was of critical importance for an accurate hematocrit calculation. From inspecting the HSA or RBC images, it was extremely difficult to identify an ischemic lesion as the tracer distribution in both images tended to be nonuniform and somewhat

irregular. Loutfi chose to deal with this issue by drawing large hemispherical regions of interest, but the lesion size and location vary so a very large ROI that includes healthy as well as hypoperfused tissue may miss significant differences between control and ischemic regions. Anatomical variation between animals also hindered the ability to infer a 'normal' image from which to base comparisons. Therefore, acquisition of the HMPAO perfusion images was imperative for quantitative accuracy.

The hematocrit values calculated from SPECT imaging showed that average healthy cerebral hematocrit levels were 0.34 and varied from 0.22 to 0.42, with cerebral hematocrit to large vessel hematocrit ratios of approximately 0.6 to 0.9. These values are within the boundaries established in the literature. Lammertsma found that cerebral hct/large vessel hct ratios varied from 0.62 to 0.94 for several studies examining rat cortex hematocrit values (Lammertsma, Brooks et al. 1984).

5.4.2 Discussion of Error Sources in Hematocrit Calculation

We should include in our discussion a brief analysis of the propagation of error throughout the measurement. The precision and accuracy of the hematocrit calculation depends upon the precision of the images used in the calculation. We can approximate the error within the image by calculating the standard error within the ROI. This value will depend upon the number of counts acquired during the scan, and the size of the ROI in voxels. As an approximation of the underlying pixel distribution, we will assume a Gaussian distribution of the pixel values. After the reconstruction process the underlying distribution of the pixel value is no longer Poisson in nature so a Gaussian assumption is reasonable. The error from the blood sample measurement can be calculated with $\sqrt{n}/n$ where n is the number of measured counts. Because the measurements contained several

hundred thousand counts, the error term is less than 0.5% and can safely be ignored. If we refer to our original equation for hematocrit:

$$h = \frac{1}{1+x} \qquad x = \frac{PcRw}{(Pcl+Rc)Pw - PcPwl} \qquad (1)$$

Our error thus depends only upon the image errors for the plasma and RBC images so the equation simplifies to:

$$\mathrm{X} = \frac{Pc}{Rc + Pcl - Pc} \quad \text{and the error terms expressed by} \quad \mathrm{E} = \frac{Ep}{Erp - Ep}$$

Where Pc is the mean ROI value from the plasma image and Rc is the mean ROI value from the combined plasma/red cell image. Ep is the standard error term from the plasma image, and Erp is the standard error from the combined RBC/plasma image. We intend to determine the worst case error for the final hematocrit calculation so we simply add our error terms in the denominator to find total denominator error:

$$\mathrm{E_{den}} = \mathrm{Ep} + \mathrm{Erp}$$

We then can add the error from the numerator and denominator using the fractional error:

$$\mathrm{Etot} = \frac{Ep}{Pc} + \frac{Eden}{\mathrm{Pr} - Pc}$$

Where Rc and Pc are the red cell image counts and plasma image counts, respectively. This calculation provides us with the maximum deviation in hematocrit value given our statistical variation in the images. We can examine the error for both the lesion and control ROI in the two rat treatment models. Tables 5.1 and 5.2 show the raw data for the 90min MCAO treatment rats and 90min MCAO plus 120min reperfusion treatment rats, respectively. Within in the 90min MCAO group, the mean lesion error was 8% and

the mean control error was 9%, which corresponds to a hematocrit difference of ±3 points in both cases. For the 90m MCAO treatment, 3 of 5 rats showed hematocrit differences larger than the expected error. The measured difference may be due to interanimal variability, statistical noise or a true hematocrit change. The significance using a paired t-test was 0.08, which suggests a significant difference between lesion and control ROIs, but more rats are needed to confirm.

Table 5.1: Raw Data Summary for 90min MCAO treatment

Propagation of Error 90m MCAO Treatment							
		sigmaHSA	sigmaRBC	voxels	St. Err.HSA	St.Err RBC	Total Error %
RAT A	lesion	1.37	2.89	306	0.079	0.165	0.05
	control	1.27	3.64	276	0.077	0.219	0.06
RAT B	lesion	1.15	2.27	327	0.064	0.126	0.07
	control	1.44	4.14	288	0.085	0.244	0.09
RAT C	lesion	1.72	3.07	402	0.086	0.153	0.05
	control	1.27	3.05	333	0.116	0.167	0.09
RAT D	lesion	2.11	1.29	228	0.084	0.086	0.10
	control	1.41	1.78	291	0.082	0.104	0.07
RAT E	lesion	2.95	5.41	234	0.193	0.354	0.13
	control	2.20	2.93	213	0.151	0.201	0.16
						Mean Lesion Error	**0.08**
						Mean Control Error	**0.09**

Table 5.2: Raw Data Summary for 90min MCAO and 120min reperfusion treatment

Propagation of Error 90m MCAO 120min reperfusion Treatment							
		sigmaHSA	sigmaRBC	voxels	St. Err.HSA	St.Err RBC	Total Error %
RAT A	lesion	2.663	5.391	348	0.143	0.289	0.09
	control	1.455	3.360	285	0.086	0.199	0.05
RAT B	lesion	1.284	2.242	267	0.079	0.137	0.07
	control	1.534	3.030	273	0.093	0.183	0.08
RAT C	lesion	2.073	2.645	315	0.117	0.149	0.11
	control	1.200	1.653	285	0.071	0.098	0.10
RAT D	lesion	1.413	1.945	249	0.090	0.123	0.18
	control	1.242	1.961	288	0.073	0.116	0.15
RAT E	lesion	2.646	2.510	327	0.146	0.139	0.12
	control	2.217	2.704	327	0.123	0.150	0.21
						Mean Lesion Error	**0.11**
						Mean Control Error	**0.12**

For the reperfusion treated rats, the % error within the lesion and control ROI's is 11% and 12%, respectively, which corresponds to a hematocrit error of ± 0.034, and ± 0.036. We can express our hematocrit measurements along with the error tolerances stemming from uncertainty in the measurement procedure. For the 90min MCAO treatment, the average lesion hematocrit was 0.42±0.04 and the control hematocrit was 0.34±0.03. For the rats treated with 90min MCAO and 120min reperfusion, the lesion hematocrit was 0.31±0.03, and the control hematocrit was 0.30±0.03. The error supports our prior conclusion that hematocrit during the vessel occlusion is significantly higher than control, and after reperfusion both hemispheres normalize.

5.4.3 Clinical Relevance of Hematocrit Measurement

The experiments performed in this work were designed to explore the acute phase of stroke where data tends to be more difficult clinically to obtain. Often stroke patients do not recognize the symptoms quickly and fail to receive prompt treatment. Most clinical evaluations take place several hours after the event and it is rare to diagnose a patient within an hour of the event. Those factors make the acute phase of stroke an excellent realm of study for small animal imaging. Because of the lack of data available during the acute phase, the published literature provides an inconsistent view of the changes in hematocrit during acute stroke. A study performed by Kuke (Kuke, Donghua et al. 2001) examined the hemorheologic properties within rats for 1 hour of ischemia followed by either 1, 6, or 12 hours of reperfusion. They found that hematocrit values initially decreased during ischemia, and then increased during the reperfusion phase. However, they were measuring hematocrit using the centrifugation technique from samples obtained from the femoral artery, not locally within the cortex. Data presented

from Sakai (Sakai, Igarashi et al. 1989) showed using SPECT that local regions of increased hematocrit showed the poorest prognosis, supporting the hypothesis that acute phase hematocrit levels rise and then return to normal as the tissue recovers. Our own data support the same conclusion with hematocrit levels measured in rats after 90 minutes of MCA occlusion higher within the ischemic lesion than control. The data also showed a correlation between the magnitude of the perfusion deficit and the rise of hematocrit, with larger deficits correlating to higher hematocrit. This would suggest that cerebral blood flow plays a major role in hematocrit regulation.

We must be careful when using the HMPAO image as a surrogate for a true CBF measurement. The HMPAO tracer is injected as a lipophilic tracer capable of passing the blood brain barrier (BBB), and then extracted quickly within the brain as the brain uptake reaches a maximum about 5 minutes after injection in humans (Leonard, Nowotnik et al. 1986; Neirinckx, Canning et al. 1987). However, the relationship between HMPAO image intensity and CBF is nonlinear (Lassen, Andersen et al. 1988), therefore we must qualify our conclusions a bit and state that differences in relative perfusion between ischemic and control regions correlate with differences in relative hematocrit levels. To establish true correlation between Hct and CBF, a more quantitative approach is needed such as ^{133}Xe-SPECT, a very difficult tracer to deal with, or PWI-MR imaging.

A cursory analysis of the reperfusion results shows large variability in both perfusion defects as measured by HMPAO, and hematocrit as measured by RBC and HSA imaging. Some rats showed hyperperfusion along with a decrease in hematocrit, while others returned to normal for both hematocrit and perfusion. Still others showed hyperperfusion with increased hematocrit, so the data does not lead to a firm conclusion.

The period during reperfusion is marked with inconsistency and instability as both the tissue and blood properties adjust to compensate for the damage caused by ischemia with hyperemia effects potentially confounding the measurements. For this reason, many studies examining the effects of reperfusion, either natural or induced, perform SPECT, or PET perfusion imaging 24hr after the induction of reperfusion (Grotta and Alexandrov 1998). After that time period, the physiological states have begun to reach new equilibrium and the effect of the reperfusion can be assessed. Future work for this project should include longer time points to examine the hematocrit and perfusion after 24 hours, instead of just two.

The hematocrit study has shown that small-animal SPECT provides a feasible and accurate method to assess hematocrit levels locally in-vivo. Applying those methods to the task of hematocrit measurement during ischemia allowed confirmation of hematocrit elevation during ischemic and low CBF conditions. Removal of the occlusion allowed for recanalization and reperfusion, but hematocrit effects were inconsistent. Future work should examine the effect of longer periods of reperfusion on hematocrit and blood viscosity values.

5.5 Concluding Remarks

The work presented in this dissertation provided advances both for imaging physics and SPECT acquisition methods, as well as small animal applications. The two segments of this work exist as a synergy between the driving force of more demanding animal applications forcing the advancement of the instrumentation of the imaging systems, which in turn allow even more advanced applications and studies.

The studies selected for this dissertation were well suited to the capabilities of the preclinical SPECT system. The simplicity and flexibility of the design allowed for the development of unconventional orbit acquisitions that may not be possible on a more rigid system. Neither animal study required involved quantitative methods such as attenuation correction, scatter correction or detector response correction that are typically applied for nuclear medicine applications, yet by selecting an appropriate measure, an accurate quantitative measurements were acquired.

Future work will further develop the dual-plane and dual-AOR orbits to better characterize the noise response and geometric response functions for more effective artifact correction, as well as examine the potential of the methods for quantitative studies. Unfortunately, the anti-MPO antibody tracer did not show sufficient specificity, but future efforts may offer refinement to the chemistry and the experimental model to better explore the potential of the tracer. The hematocrit study should continue to explore the relationships between ischemic duration, cerebral blood flow, and hematocrit. As a functional imaging modality, SPECT is uniquely appropriate for exploring the rheological effects of acute ischemic stroke.

References

Allport, L. E., M. W. Parsons, et al. (2005). "Elevated hematocrit is associated with reduced reperfusion and tissue survival in acute stroke." Neurology **65**(9): 1382-7.

Baron, J. C., R. S. Frackowiak, et al. (1989). "Use of PET methods for measurement of cerebral energy metabolism and hemodynamics in cerebrovascular disease." J Cereb Blood Flow Metab **9**(6): 723-42.

Beque, D., J. Nuyts, et al. (2003). "Characterization of pinhole SPECT acquisition geometry." IEEE Trans Med Imaging **22**(5): 599-612.

Beque, D., J. Nuyts, et al. (2005). "Optimization of geometrical calibration in pinhole SPECT." IEEE Trans Med Imaging **24**(2): 180-90.

Bryan, R. N., L. M. Levy, et al. (1991). "Diagnosis of acute cerebral infarction: comparison of CT and MR imaging." AJNR Am J Neuroradiol **12**(4): 611-20.

Coles, J. P., T. D. Fryer, et al. (2006). "Intersubject variability and reproducibility of 15O PET studies." J Cereb Blood Flow Metab **26**(1): 48-57.

Davis, D. P., T. Robertson, et al. (2006). "Diffusion-weighted magnetic resonance imaging versus computed tomography in the diagnosis of acute ischemic stroke." J Emerg Med **31**(3): 269-77.

Falk, R. J. and J. C. Jennette (1997). "ANCA small-vessel vasculitis." J Am Soc Nephrol **8**(2): 314-22.

Forrer, F., R. Valkema, et al. (2006). "In vivo radionuclide uptake quantification using a multi-pinhole SPECT system to predict renal function in small animals." Eur J Nucl Med Mol Imaging **33**(10): 1214-7.

Frackowiak, R. S., G. L. Lenzi, et al. (1980). "Quantitative measurement of regional cerebral blood flow and oxygen metabolism in man using 15O and positron emission tomography: theory, procedure, and normal values." J Comput Assist Tomogr **4**(6): 727-36.

Funk, T., P. Despres, et al. (2006). "A multipinhole small animal SPECT system with submillimeter spatial resolution." Med Phys **33**(5): 1259-68.

Funk, T., D. L. Kirch, et al. (2006). "A novel approach to multipinhole SPECT for myocardial perfusion imaging." J Nucl Med **47**(4): 595-602.

Gibbs, J. M., K. L. Leenders, et al. (1984). "Evaluation of cerebral perfusion reserve in patients with carotid-artery occlusion." Lancet **1**(8370): 182-6.

Grotta, J. C. and A. V. Alexandrov (1998). "tPA-associated reperfusion after acute stroke demonstrated by SPECT." Stroke **29**(2): 429-32.

Guadagno, J. V., E. A. Warburton, et al. (2004). "Does the acute diffusion-weighted imaging lesion represent penumbra as well as core? A combined quantitative PET/MRI voxel-based study." J Cereb Blood Flow Metab **24**(11): 1249-54.

Hashimoto, Y., T. Hirano, et al. (2005). "Therapeutic strategy for acute stroke--prologue for an epoch of brain attack--. Progress of diagnosis of acute stroke." Intern Med **44**(4): 360-2.

Heeringa, P., D. Huugen, et al. (2005). "Anti-neutrophil cytoplasmic autoantibodies and leukocyte-endothelial interactions: a sticky connection?" Trends Immunol **26**(11): 561-4.

Hoshino, A., T. Nagao, et al. (2007). "Nanocrystal quantum dot-conjugated anti-myeloperoxidase antibody as the detector of activated neutrophils." IEEE Trans Nanobioscience **6**(4): 341-5.

Hudson, H., Larkin, RS (1994). "Accelerated image reconstruction using ordered subsets of projection data." IEEE Trans Med Imaging **13**: 601-609.

Huugen, D., J. W. Tervaert, et al. (2004). "Antineutrophil cytoplasmic autoantibodies and pathophysiology: new insights from animal models." Curr Opin Rheumatol **16**(1): 4-8.

Ishizu, K., T. Mukai, et al. (1995). "Ultra-high resolution SPECT system using four pinhole collimators for small animal studies." J Nucl Med **36**(12): 2282-7.

Jaszczak, R. J., J. Li, et al. (1994). "Pinhole collimation for ultra-high-resolution, small-field-of-view SPECT." Phys Med Biol **39**(3): 425-37.

Jennette, J. C. and R. J. Falk (1997). "Small-vessel vasculitis." N Engl J Med **337**(21): 1512-23.

Jennette, J. C. and R. J. Falk (1998). "Pathogenesis of the vascular and glomerular damage in ANCA-positive vasculitis." Nephrol Dial Transplant **13 Suppl 1**: 16-20.

Jennette, J. C., H. Xiao, et al. (2006). "Pathogenesis of vascular inflammation by anti-neutrophil cytoplasmic antibodies." J Am Soc Nephrol **17**(5): 1235-42.

Kadrmas, D. J., R. J. Jaszczak, et al. (1995). "Truncation artifact reduction in transmission CT for improved SPECT attenuation compensation." Phys Med Biol **40**(6): 1085-104.

Kallenberg, C. G. (1998). "Autoantibodies to myeloperoxidase: clinical and pathophysiological significance." J Mol Med **76**(10): 682-7.

Karonen, J. O., L. Ostergaard, et al. (2001). "Diffusion and perfusion MR imaging in acute ischemic stroke: a comparison to SPECT." Comput Methods Programs Biomed **66**(1): 125-8.

Klaunberg, B. A. and M. J. Lizak (2004). "Considerations for setting up a small-animal imaging facility." Lab Anim (NY) **33**(3): 28-34.

Kuke, D., L. Donghua, et al. (2001). "Alteration of blood hemorheologic properties during cerebral ischemia and reperfusion in rats." J Biomech **34**(2): 171-5.

Lammertsma, A. A., D. J. Brooks, et al. (1984). "In vivo measurement of regional cerebral haematocrit using positron emission tomography." J Cereb Blood Flow Metab **4**(3): 317-22.

Lammertsma, A. A., T. Jones, et al. (1981). "A theoretical study of the steady-state model for measuring regional cerebral blood flow and oxygen utilisation using oxygen-15." J Comput Assist Tomogr **5**(4): 544-50.

Lassen, N. A., A. R. Andersen, et al. (1988). "The retention of [99mTc]-d,l-HM-PAO in the human brain after intracarotid bolus injection: a kinetic analysis." J Cereb Blood Flow Metab **8**(6): S13-22.

Leonard, J. P., D. P. Nowotnik, et al. (1986). "Technetium-99m-d, 1-HM-PAO: a new radiopharmaceutical for imaging regional brain perfusion using SPECT--a comparison with iodine-123 HIPDM." J Nucl Med **27**(12): 1819-23.

Li, T. Q., Z. G. Chen, et al. (1998). "Diffusion-weighted MR imaging of acute cerebral ischemia." Acta Radiol **39**(5): 460-73.

Loutfi, I., R. S. Frackowiak, et al. (1987). "Regional brain hematocrit in stroke by single photon emission computed tomography imaging." Am J Physiol Imaging **2**(1): 10-6.

Love, C. and C. J. Palestro (2004). "Radionuclide imaging of infection." J Nucl Med Technol **32**(2): 47-57; quiz 58-9.

Lyons, S. K. (2005). "Advances in imaging mouse tumour models in vivo." J Pathol **205**(2): 194-205.

MacDonald, L. R., B. E. Patt, et al. (2001). "Pinhole SPECT of Mice Using the LumaGEM Gamma Camera." IEEE Trans. Nucl. Sci. **48**(3): 830-836.

Mackenzie, M. R., N. L. Warner, et al. (1978). "The binding of murine immunoglobulins to staphylococcal protein A." J Immunol **120**(5): 1493-6.

Mansi, I. A., A. Opran, et al. (2002). "ANCA-associated small-vessel vasculitis." Am Fam Physician **65**(8): 1615-20.

Metzler, S. D., R. J. Jaszczak, et al. (2005). "Molecular imaging of small animals with a triple-head SPECT system using pinhole collimation." IEEE Trans Med Imaging **24**(7): 853-62.

Neirinckx, R. D., L. R. Canning, et al. (1987). "Technetium-99m d,l-HM-PAO: a new radiopharmaceutical for SPECT imaging of regional cerebral blood perfusion." J Nucl Med **28**(2): 191-202.

Orlov, S. S. (1975). "Theory of three dimensional reconstruction. I. Conditions for a complete set of projections." Sov. Phys. Crystallogr. **20**(3): 312-314.

Parsons, M. W., E. M. Pepper, et al. (2007). "Identification of the penumbra and infarct core on hyperacute noncontrast and perfusion CT." Neurology **68**(10): 730-6.

Popov, V., S. Majewski, et al. (2001). "Analog Readout System with Charge Division Type Output." Proc. IEEE Nuclear Science Symp. and Medical Imaging Conf. Rec. San Deigo, CA, Nov. 2001: 1937.

Powers, W. J., R. L. Grubb, Jr., et al. (1984). "Physiological responses to focal cerebral ischemia in humans." Ann Neurol **16**(5): 546-52.

Querol Sans, M., J. W. Chen, et al. (2005). "Myeloperoxidase activity imaging using (67)Ga labeled substrate." Mol Imaging Biol **7**(6): 403-10.

Rentmeester, M. C., F. van der Have, et al. (2007). "Optimizing multi-pinhole SPECT geometries using an analytical model." Phys Med Biol **52**(9): 2567-81.

Rivers, C. S., J. M. Wardlaw, et al. (2006). "Do acute diffusion- and perfusion-weighted MRI lesions identify final infarct volume in ischemic stroke?" Stroke **37**(1): 98-104.

Ryu, C. W., D. H. Lee, et al. (2006). "Acquisition of MR perfusion images and contrast-enhanced MR angiography in acute ischaemic stroke patients: which procedure should be done first?" Br J Radiol **79**(948): 962-7.

S. Cherry, J. S., M. Phelps (2003). "Physics in Nuclear Medicine 3rd edition." Saunders: 280-283.

Sakai, F., H. Igarashi, et al. (1989). "Cerebral blood flow and cerebral hematocrit in patients with cerebral ischemia measured by single-photon emission computed tomography." Acta Neurol Scand Suppl **127**: 9-13.

Savage, C. O., L. Harper, et al. (2002). "New findings in pathogenesis of antineutrophil cytoplasm antibody-associated vasculitis." Curr Opin Rheumatol **14**(1): 15-22.

Schaefer, P. W., W. A. Copen, et al. (2006). "Diffusion-weighted imaging in acute stroke." Magn Reson Imaging Clin N Am **14**(2): 141-68.

Schramm, N., A. Wirrwar, et al. (2000). "Compact High Resolution Detector for Small Animal SPECT." IEEE Trans. Nucl. Sci. **47**(3): 1163-1167.

Shepp, L., Vardi, Y (1982). "Maximum Likelihood Reconstruction for Emission Tomography." IEEE Trans Med Imaging **1**: 113-122.

Souid, M., N. H. Terki, et al. (2001). "Myeloperoxidase anti-neutrophil cytoplasmic autoantibodies (MPO-ANCA)-related rapidly progressive glomerulonephritis (RPGN) and pulmonary fibrosis (PF) with dissociated evolution." Clin Nephrol **55**(4): 337-8.

Srinivasan, A., M. Goyal, et al. (2006). "State-of-the-art imaging of acute stroke." Radiographics **26 Suppl 1**: S75-95.

Strand, S. E., M. Ivanovic, et al. (1994). "Small animal imaging with pinhole single-photon emission computed tomography." Cancer **73**(3 Suppl): 981-4.

Suzuki, K. (2001). "Neutrophil functions of patients with vasculitis related to myeloperoxidase-specific anti-neutrophil antibody." Int J Hematol **74**(2): 134-43.

Tan, J. C., W. P. Dillon, et al. (2007). "Systematic comparison of perfusion-CT and CT-angiography in acute stroke patients." Ann Neurol.

Tan, J. D., W. Liu, S (2007). "Systematic comparison of perfusion-CT and CT-angiography in acute stroke patients." Annals of Neurology.

Tsui, B. M., E. C. Frey, et al. (1994). "The importance and implementation of accurate 3D compensation methods for quantitative SPECT." Phys Med Biol **39**(3): 509-30.

Tuy, H. (1983). "An Inversion Formula for Cone-beam Reconstruction." SIAM J Appl Math **43**: 546-552.

Vastenhouw, B. and F. Beekman (2007). "Submillimeter Total-Body Murine Imaging with U-SPECT-I." J Nucl Med **48**(3): 487-493.

von Kummer, R., K. L. Allen, et al. (1997). "Acute stroke: usefulness of early CT findings before thrombolytic therapy." Radiology **205**(2): 327-33.

Weber, D. A. and M. Ivanovic (1995). "Pinhole SPECT: ultra-high resolution imaging for small animal studies." J Nucl Med **36**(12): 2287-9.

Weber, D. A., M. Ivanovic, et al. (1994). "Pinhole SPECT: an approach to in vivo high resolution SPECT imaging in small laboratory animals." J Nucl Med **35**(2): 342-8.

Weisenberger, A., E. Bradley, et al. (1997). "Development of a Novel Radiation Imaging Detector System for In Vivo gene Imaging in Small Animals." Conf. Rec. 1996 IEEE NSS/MIC, Anaheim, CA, Nov. 2-9 **2**: 1201-1205.

Weisenberger, A., R. Wojcik, et al. (2003). "SPECT-CT System for Small Animal Imaging." IEEE Trans. Nucl. Sci. **50**(1): 74-79.

Xiao, H., P. Heeringa, et al. (2002). "Antineutrophil cytoplasmic autoantibodies specific for myeloperoxidase cause glomerulonephritis and vasculitis in mice." J Clin Invest **110**(7): 955-63.

Xiao, H., P. Heeringa, et al. (2005). "The role of neutrophils in the induction of glomerulonephritis by anti-myeloperoxidase antibodies." Am J Pathol **167**(1): 39-45.

Yamauchi, H., H. Fukuyama, et al. (1998). "Cerebral hematocrit decreases with hemodynamic compromise in carotid artery occlusion: a PET study." Stroke **29**(1): 98-103.

Yumura, W., M. Itabashi, et al. (2006). "A novel mouse model for MPO-ANCA-associated glomerulonephritis." Microbiol Immunol **50**(2): 149-57.

Zeng, G. L. and G. T. Gullberg (1992). "A cone-beam tomography algorithm for orthogonal circle-and-line orbit." Phys Med Biol **37**(3): 563-77.